AWARD NUMBER: W81XWH-17-0206

TITLE: Novel therapy strategies for mesenchymal non-small cell lung cancer

PRINCIPAL INVESTIGATOR: Faye Johnson, MD, PhD

CONTRACTING ORGANIZATION: MD Anderson Cancer Center
Houston, TX 77030

REPORT DATE: September 2019

TYPE OF REPORT: Final

PREPARED FOR: U.S. Army Medical Research and Materiel Command
Fort Detrick, Maryland 21702-5012

REPORT DOCUMENTATION PAGE

Form Approved
OMB No. 0704-0188

1. REPORT DATE	2. REPORT TYPE	3. DATES COVERED
September 2019	Final	1 Jul 2017 - 30 Jun 2019

4. TITLE AND SUBTITLE
Novel therapy strategies for mesenchymal non-small cell lung cancer

5a. CONTRACT NUMBER

5b. GRANT NUMBER
W81XWH-17-0206

5c. PROGRAM ELEMENT NUMBER

6. AUTHOR(S)
Faye Johnson, MD, PhD

E-Mail: fmjohns@mdanderson.org

5d. PROJECT NUMBER

5e. TASK NUMBER

5f. WORK UNIT NUMBER

7. PERFORMING ORGANIZATION NAME(S) AND ADDRESS(ES)

University of Texas MD Anderson Cancer Center
1515 Holcombe Blvd Unit 207
Houston, TX 77030-4017

8. PERFORMING ORGANIZATION REPORT NUMBER

9. SPONSORING / MONITORING AGENCY NAME(S) AND ADDRESS(ES)

U.S. Army Medical Research and Materiel Command
Fort Detrick, Maryland 21702-5012

10. SPONSOR/MONITOR'S ACRONYM(S)

11. SPONSOR/MONITOR'S REPORT NUMBER(S)

12. DISTRIBUTION / AVAILABILITY STATEMENT

Approved for Public Release; Distribution Unlimited

13. SUPPLEMENTARY NOTES

Despite therapeutic improvements for non-small cell lung cancer (NSCLC), there is still an unmet need for effective systemic therapy. To address this need, we previously demonstrated that mesenchymal NSCLC was sensitive to polo-like kinase 1 (PLK1) inhibitors, but the mechanisms of resistance to PLK1 inhibitors in epithelial NSCLC remain unknown. We observed differential regulation of the cMet/FAK/Src axis, which is intact in both mesenchymal and epithelial cells. However, PLK1 inhibition inhibits cMet phosphorylation only in mesenchymal NSCLC cells, leading to subsequent inhibition of FAK and Src. Constitutively active cMet abrogates PLK1 inhibitor–induced apoptosis. Likewise, cMet silencing or inhibition enhances PLK1 inhibitor–induced apoptosis. Additionally, cells with acquired resistance to PLK1 inhibitors are more epithelial than their parental cells and maintain cMet activation after PLK1 inhibition. In both patient-derived and cell line xenografts, mesenchymal NSCLC was more sensitive to PLK1 inhibition alone than was epithelial NSCLC. The combination of cMet and PLK1 inhibition led to regression of tumors in three models and marked tumor size reduction in the fourth model. When drug treatment was stopped, tumors treated with the combination did not regrow. PLK1 inhibition did not affect levels of HGF but did decrease vimentin phosphorylation, which regulates cMet phosphorylation via β1 integrin. This research defines a heretofore unknown mechanism of ligand-independent activation of cMet downstream of PLK1, as well as an effective combination therapy.

15. SUBJECT TERMS
Polo-like kinase 1 (PLK1)
Non-small cell lung cancer (NSCLC)

16. SECURITY CLASSIFICATION OF:			17. LIMITATION OF ABSTRACT	18. NUMBER OF PAGES	19a. NAME OF RESPONSIBLE PERSON
a. REPORT	b. ABSTRACT	c. THIS PAGE			USAMRMC
Unclassified	Unclassified	Unclassified	Unclassified	49	19b. TELEPHONE NUMBER *(include area code)*

TABLE OF CONTENTS

1. **INTRODUCTION:** *Narrative that briefly (one paragraph) describes the subject, purpose and scope of the research.*

The successful completion of this project will validate polo-like kinase 1 (PLK1) as a potential therapeutic target for mesenchymal non-small cell lung cancer (NSCLC) and provide prospective biomarkers of response to PLK1 inhibitors that could be used to select patients for a future clinical trial (Aim 1). We may also identify rational drug combinations for clinical trial by testing anti-PD1 antibodies (Aim 2) and cMet inhibitors (Aim 3) with PLK1 inhibition.

2. **KEYWORDS:** *Provide a brief list of keywords (limit to 20 words).*

polo-like kinase 1 (PLK1)
non-small cell lung cancer (NSCLC)

3. **ACCOMPLISHMENTS:**

What were the major goals of the project?

Specific Aim 1: To validate mesenchymal biomarkers as predictors of PLK1 inhibition–induced apoptosis in NSCLC *in vivo* using patient derived xenografts (PDXs) and an immunocompetent, orthotopic model of NSCLC.	**Timeline**	**Site 1**
Major Task 1: Determination of biomarker expression and efficacy of volasertib in PDX models	Months	
Milestone: Obtain HRPO approval	3	Dr. Johnson
Milestone: Obtain ACURO approval	3	Dr. Johnson
Implant 20 independent PDX models into 10 mice per group with one, independent biological replicate group. The number of mice needed for this experiment is: 5 mice per treatment group x 2 treatment groups x 2 biological replicates x 20 PDX models = 400 mice.	4-17	Dr. Johnson, 400 mice
Treat mice with volasertib or DMSO (n=5 mice per treatment group)	7-18	Dr. Johnson
Collect tissue for biomarkers	7-19	Dr. Johnson
Biomarker measurement and quantification via IHC staining.	19-21	Dr. Wistuba
Data analysis	21-24	Dr. Johnson
Major Task 2: Efficacy of volasertib in NSCLC with epithelial and mesenchymal phenotypes (GEMM tumors)		
Transfection of murine cells from $Kras^{LA1/+}p53^{R172H\Delta G/+}$ (KP) mice.	6-9	Dr. Johnson and Gibbons
Orthotopic implantation, treat with volasertib or DMSO. For each cell line, the tumor cells are implanted in the lungs of 20 mice. Five mice that express miR200a/b will be used for treatment, five mice that express ZEB1 will be used for	9-16	Dr. Johnson and Gibbons, 120 mice

treatment and ten for control. Thus, each independent model requires 20 mice. With 6 cell lines, the total number of mice required for this aim will be: 20 mice per cell line x 6 cell lines = 120		
Biomarker measurement and quantification via IHC staining.	10-17	Dr. Wistuba
Data analysis	18-24	Dr. Johnson
Specific Aim 2: To test the hypothesis that the combination of anti-PD1 immunotherapy and PLK1 inhibition will lead to tumor regression in mesenchymal NSCLC in vivo.	**Timeline**	**Site 1**
Major Task 3: Establish the degree of heterogeneity of EMT in NSCLC patient tumors		
Measure the EMT score in 3 regions of 100 NSCLC tumors to estimate the intra-tumor heterogeneity of the EMT score.	1-12	Dr. Johnson, funded other sources (donors)
Major Task 4: Test the combination of PLK1 inhibitors with PD1 inhibitors in syngeneic models of mesenchymal NSCLC		
Three, independent isogenic mesenchymal cell lines from KP mice will be injected into 129Sv mice	9-12	Dr. Gibbons
Treat with murine anti-PD1 or control. Three mesenchymal models x 10 mice per treatment arm x 4 treatment groups = 120 mice.	12-18	Dr. Johnson, 120 mice
Biomarker measurement with TILs measured by flow cytometry.	17-19	Dr. Johnson and Dr. Wistuba
Data analysis	19-24	Dr. Johnson
Specific Aim 3: To determine if FAK mediates PLK1-inhibitor induced apoptosis in NSCLC in vitro and in vivo.	**Timeline**	**Site 1**
Major Task 5: Test the combination of PLK1 inhibitors with FAK inhibitors		
Test PLK1 and FAK (defactinib) inhibitors in vitro. Effects of the single agents and combinations on senescence, apoptosis, and cell cycle will be measured	1-9	Dr. Johnson
Determine if FAK overexpression leads to PLK1 inhibitor resistance via use of an inducible vector to conditionally express FAK in 3 mesenchymal (commercially, available) NSCLC cell lines.	10-17	Dr. Johnson
Data analysis	18-24	Dr. Johnson

What was accomplished under these goals?

Under Major Task 1, we demonstrated that the PLK1 inhibitor volasertib was more effective in mesenchymal than in epithelial NSCLC patient derived xenograft (PDX) models (Figure 1).

Major Tasks 2 and 3 were completed as described in our two publications (manuscripts in the appendix of this report). Year two of the award included manuscript writing, revisions, and responses to reviewers for publication of the *Neoplasia* manuscript.

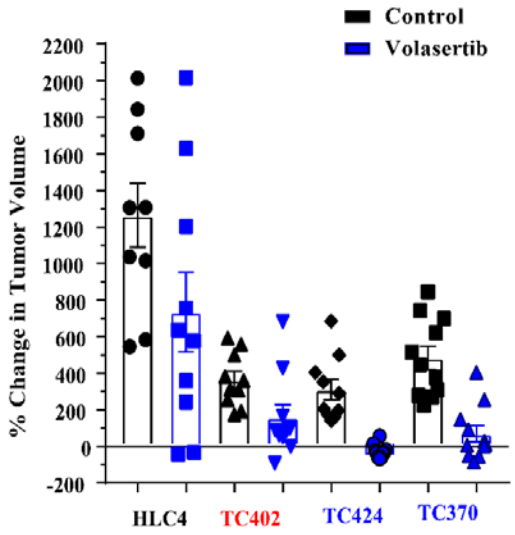

Figure 1: Mesenchymal NSCLC PDX tumors are more sensitive to PLK1 inhibition induced apoptosis in comparison to epithelial NSCLC PDX tumors. The overall percent change in tumor volume between the vehicle and Volasertib treated mice at the end of the experiment for all the PDX models is depicted. Each data point represents one mouse in the respective group. HLC4 has intermediate morphology. TC402 is epithelial. TC424 and TC370 are mesenchymal.

Viswanath P, Peng S, Singh R, Kingsley C, Balter PA, **Johnson FM**. *A Novel Method for Quantifying Total Thoracic Tumor Burden in Mice*. Neoplasia. 2018;20(10):975-84. PMID: 30157470

Lee WC, Diao L, Wang J, Zhang J, Roarty EB, Varghese S, Chow CW, Fujimoto J, Behrens C, Cascone T, Peng W, Kalhor N, Moran CA, Weissferdt A, **Johnson FM**, William WN, Jr., Swisher SG, Lee JJ, Hong WK, Heymach JV, Wistuba, II, Futreal PA, Zhang J. *Multiregion gene expression profiling reveals heterogeneity in molecular subtypes and immunotherapy response signatures in lung cancer*. Mod Pathol. 2018;31(6):947-55. PMID: 29410488.

Major Task 4 involved the combination of PLK1 and anti-PD1 inhibition in murine models. However, PLK1 inhibition with volasertib alone was very effective in the planned models of KP cell lines that were injected into syngeneic 129Sv mice. Volasertib led to marked tumor regression despite the use of several different dosing regimens and the modification of the timing and number of cells injected (representative data, Figure 2). As such, this was not an appropriate model to test for synergy with the addition of anti-PD1 therapy. We hypothesized that a more specific PLK1 inhibitor would lead to less apoptosis in KP cells. Additionally, a more specific PLK1 inhibitor would likely be less toxic in humans in future clinical trials. We chose to use NMS-937 (PCM075) due to its specificity toward PLK1 as well as its current clinical development. However, NMS937 was not effective when tested in 44 NSCLC

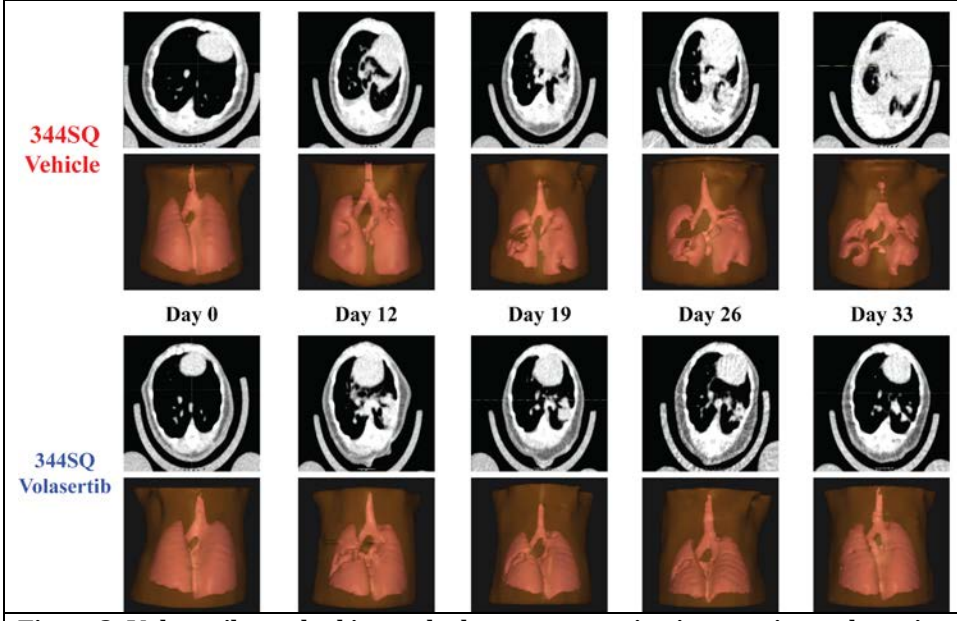

Figure 2. Volasertib resulted in marked tumor regression in a murine orthotopic model of mesenchymal metastatic NSCLC. Representative images of micro-CT and 3 dimensional mass of the thoracic cavity images in mice treated with vehicle control or volasertib.

cell lines *in vitro* (Figure 3). In a separate project, we also determined that NMS937 was wholly ineffective and poorly tolerated in NSCLC xenografts models. Our resources for this task were exhausted in these attempts to overcome the technical hurdles.

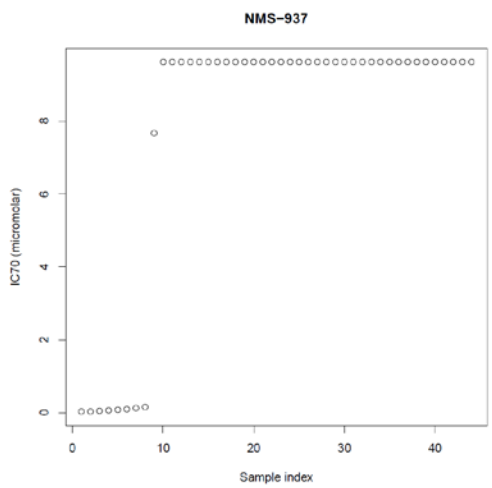

Figure 3. The PLK1 inhibitor NMS-937 was not effective in most NSCLC cell lines. Forty four NSLCC cell lines were incubated with 0-10 µM NMS-937 for 72 hours and cell viability was measure using cell titer glo. The inhibitory concentration (IC) was calculated using CalcuSyn Software.

Major Tasks 5 was completed as described in our publication (manuscript attached to this report). Year two of the award included manuscript writing, revisions, and responses to reviewers for publication of the *EMBO Mol Med* manuscript.

Singh R, Peng S, Viswanath P, Sambandam V, Shen L, Rao X, Fang B, Wang J, **Johnson FM**. *Non-canonical cMet regulation by vimentin mediates Plk1 inhibitor-induced apoptosis.* EMBO Mol Med. 2019;11(5). Epub 2019/05/02. doi: 10.15252/emmm.201809960. PubMed PMID: 31040125; PubMed Central PMCID: PMCPMC6505578.

What opportunities for training and professional development has the project provided?

Graduate student Pavitra Viswanath was funded by this grant in Year 1. She completed her master's degree and has one first author publication from this work. Based on her successful research, she was able to secure a position at the University of Utah graduate school where she is pursuing a PhD in cancer research.

Post-doctoral fellow Ratnakar Singh was funded by this grant in Year 1. He has one first author publication from this work. He presented his research at the annual American Association for Cancer Research (AACR) meetings in 2017 and 2018. Based on his successful research, he was able to secure a fellowship at the University of Illinois.

How were the results disseminated to communities of interest?

The results were published in three peer-reviewed journals (as listed above) and presented at the American Association for Cancer Research (AACR) Meetings in 2017 and 2018.

What do you plan to do during the next reporting period to accomplish the goals?

Nothing to Report

4. **IMPACT:** D*escribe distinctive contributions, major accomplishments, innovations, successes, or any change in practice or behavior that has come about as a result of the project relative to:*

What was the impact on the development of the principal discipline(s) of the project?

Non-small cell lung cancer (NSCLC) cell lines have diverse sensitivities to inhibition of a protein that helps cancer cells to divide – PLK1. These lab findings are consistent with the results of clinical trials of PLK1 inhibitors in NSCLC. Our research revealed a novel mechanism of resistance to PLK1 inhibitors through the non-canonical activation of a cell surface protein, cMet. The addition of cMet inhibitors is a promising therapeutic strategy to overcome *de novo* and acquired resistance to PLK1 inhibitors in patients with NSCLC.

What was the impact on other disciplines?
Nothing to report

What was the impact on technology transfer?
Nothing to report

What was the impact on society beyond science and technology?
Nothing to report

5. CHANGES/PROBLEMS:
Nothing to report

Changes in approach and reasons for change
Nothing to report

Actual or anticipated problems or delays and actions or plans to resolve them
Nothing to report

Changes that had a significant impact on expenditures
Nothing to report

Significant changes in use or care of human subjects, vertebrate animals, biohazards, and/or select agents
Nothing to report

6. PRODUCTS:
Nothing to report

- **Publications, conference papers, and presentations**

Journal publications.

Viswanath P, Peng S, Singh R, Kingsley C, Balter PA, Johnson FM. A Novel Method for Quantifying Total Thoracic Tumor Burden in Mice. Neoplasia. 2018;20(10):975-84. PMID: 30157470

Singh R, Peng S, Viswanath P, Sambandam V, Shen L, Rao X, Fang B, Wang J, Johnson FM. Non-canonical cMet regulation by vimentin mediates Plk1 inhibitor-induced apoptosis. EMBO Mol Med. 2019;11(5). Epub 2019/05/02. doi: 10.15252/emmm.201809960. PubMed PMID: 31040125; PubMed Central PMCID: PMCPMC6505578.

Books or other non-periodical, one-time publications. *None*

Other publications, conference papers and presentations.

Singh R, Shen L, Tong P, Wang J, Johnson FM. c-Met activation mediates resistance to polo-like kinase 1 inhibitor-induced apoptosis in non-small cell lung cancer. American Association for Cancer Research Annual Meeting (AACR) - Washington DC, 4/2017

Singh S, Viswanath P, Peng S, Sambandam V, Shen L, Li L, Wang J, Fang B, Johnson FM. Noncanonical c-Met activation mediates de novo and acquired resistance to polo-like kinase 1 inhibitor-induced apoptosis in non-small cell lung cancer. American Association for Cancer Research Annual Meeting (AACR) - Chicago, IL (#895), 4/2018

- **Website(s) or other Internet site(s)**

Nothing to Report

- **Technologies or techniques**

Nothing to Report

- **Inventions, patent applications, and/or licenses**

Nothing to Report

- **Other Products**

Nothing to Report

7. PARTICIPANTS & OTHER COLLABORATING ORGANIZATIONS

What individuals have worked on the project?

Name:	Faye Johnson, Project Years 1-2
Project Role:	Principal Investigator
Nearest Person Month Worked	5
Contribution to Project:	Dr. Johnson conceived and designed the proposed project and is responsible for overall scientific direction of the research, for reviewing and validating the data resulting from the research, and for supervising day-to-day experiments.
Funding support:	Dr. Johnson's salary is provided in part by UT MD Anderson Cancer Center

Name:	Tuhina Mazumdar, Project Year 2
Project Role:	Research Investigator
Nearest Person Month Worked	7
Contribution to Project:	She performed the bench experiments.
Funding support:	Additional salary support on: donor funds

Name:	Shaohua Peng, Project Year 2
Project Role:	Research Investigator
Nearest Person Month Worked	8
Contribution to Project:	He performed the bench experiments and the animal studies.
Funding support:	Additional salary support on: U01DE025181; donor funds; Trovagene

Name:	Ratnakar Singh, Project Year 1
Project Role:	Post Doc Fellow
Nearest Person Month Worked	12
Contribution to Project:	Dr. Singh performs the bench experiments and the animal studies on this project.
Funding support:	Funded 100% from this award

Name:	Pavitra Viswanath, Project Year 1
Project Role:	Graduate Student
Nearest Person Month Worked	12
Contribution to Project:	Ms. Viswanath performs the bench experiments and the animal studies on this project.
Funding support:	Funded 100% from this award

Has there been a change in the active other support of the PD/PI(s) or senior/key personnel since the last reporting period?

Changes to other support **– <u>Faye Johnson, MD, PhD – Principal Investigator</u>**

Grants Closed:

NIDCR -5 U01 DE025181 – "Translating genomic alterations into novel therapeutic targets in head and neck cancer through computational and functional approaches" - 07/01/2015-04/30/2019 – 1.5%, 0.18 calendar months

National Institutes of Health (NIH) - 5 R01DE024601 – "Predicting and overcoming chemoradioresistance in p53-mutant head and neck cancer" - 07/20/2014 – 05/31/2019 – 5%, 0.60 calendar months

National Institutes of Health (NIH)/National Institute of Dental and Craniofacial Research (NIDCR) –" HPV Moonshot Flagship" - 09/01/2014 – 12/31/2018 – 10% - 1.20 calendar months

National Institutes of Health (NIH) – R01 CA168485 –"Extension of Radiotherapy Research" – 03/01/2017-02/28/2019 – 1% - 0.12 calendar months

Trovagene – LS2018-00055359-"To determine if cMet mediates PLK-1 inhibitor induced apoptosis in non-small cell lung cancer (NSCLC) in vitro and in vivo" - 06/29/2018-06/28/2019 – 1%, 0.12 calendar months

New Active Grants:

National Institutes of Health (NIH)/National Cancer Institute (NCI) - 1R01CA235620-01A1 - **"**Targeting Alterations of the NOTCH1 Pathway in Head & Neck Squamous Cell Carcinoma (HNSCC)" - 09/08/2019/-08/31/2024 – 20% - 2.40 calendar months

PIQUR Therapeutics AG – "Open-Label, Single Arm, Two-Stage Study, Evaluating the Efficacy and Safety of Bimiralisib (PQR309) in Patients with Recurrent or Metastatic (r/m) Head and Neck Squamous Cell Carcinomas (HNSCC) Harboring NOTCH1 Loss of Function (LOF) Mutations" – 01/18/2019-01/07/2026 – 7%, 0.84 calendar months

Changes to Other Support **– <u>Don Gibbons, MD, PhD – Co-Investigator</u>**

Grants Closed

LUNGevity Foundation – "Axl as a target to reverse EMT, treatment resistance and immunosuppression" - 08/01/2015 – 07/31/2019 – 5%, 0.60 calendar months

New Active Grants:

None

What other organizations were involved as partners?

Nothing to Report

8. SPECIAL REPORTING REQUIREMENTS

COLLABORATIVE AWARDS: *NA*

QUAD CHARTS: *NA*

9. APPENDICES: *Three journal articles.*

Research Article

SOURCE DATA | TRANSPARENT PROCESS | OPEN ACCESS

EMBO Molecular Medicine

Non-canonical cMet regulation by vimentin mediates Plk1 inhibitor–induced apoptosis

Ratnakar Singh[1], Shaohua Peng[1], Pavitra Viswanath[1,2], Vaishnavi Sambandam[1], Li Shen[3], Xiayu Rao[3], Bingliang Fang[4], Jing Wang[2,3] & Faye M Johnson[1,2,*]

Abstract

To address the need for improved systemic therapy for non–small-cell lung cancer (NSCLC), we previously demonstrated that mesenchymal NSCLC was sensitive to polo-like kinase (Plk1) inhibitors, but the mechanisms of resistance in epithelial NSCLC remain unknown. Here, we show that cMet was differentially regulated in isogenic pairs of epithelial and mesenchymal cell lines. Plk1 inhibition inhibits cMet phosphorylation only in mesenchymal cells. Constitutively active cMet abrogates Plk1 inhibitor–induced apoptosis. Likewise, cMet silencing or inhibition enhances Plk1 inhibitor–induced apoptosis. Cells with acquired resistance to Plk1 inhibitors are more epithelial than their parental cells and maintain cMet activation after Plk1 inhibition. In four animal NSCLC models, mesenchymal tumors were more sensitive to Plk1 inhibition alone than were epithelial tumors. The combination of cMet and Plk1 inhibition led to regression of tumors that did not regrow when drug treatment was stopped. Plk1 inhibition did not affect HGF levels but did decrease vimentin phosphorylation, which regulates cMet phosphorylation via β1-integrin. This research defines a heretofore unknown mechanism of ligand-independent activation of cMet downstream of Plk1 and an effective combination therapy.

Keywords cMet; drug combination; NSCLC; Plk1; vimentin

Subject Categories Cancer; Pharmacology & Drug Discovery; Respiratory System

DOI 10.15252/emmm.201809960 | Received 19 October 2018 | Revised 28 February 2019 | Accepted 12 March 2019 | Published online 30 April 2019

EMBO Mol Med (2019) 11: e9960

Introduction

Lung cancer remains the most lethal cancer, contributing to 27% of cancer-related deaths in the United States (Siegel *et al*, 2018). Although personalized treatment approaches based on genetic mutations that underlie non–small-cell lung cancer (NSCLC) have been developed and immunotherapy is very effective in some patients, the 5-year overall survival rate for all stages of NSCLC is only 18% and a dismal 5% for those with metastatic disease (Siegel *et al*, 2018). Therefore, numerous new potential targets, including several cell cycle kinases, are under investigation to further improve patient survival. Polo-like kinase 1 (Plk1) is a serine–threonine protein kinase that is overexpressed in cancer cells and plays a major role in the regulation of G2–M transition and response to DNA damage. Inhibitors of Plk1 are under active clinical development in oncology (NCT03414034 and NCT03303339).

Despite Plk1's reputation as an essential protein for cell survival, Plk1 inhibitors are well tolerated by patients (Nokihara *et al*, 2016; Pujade-Lauraine *et al*, 2016; Schoffski *et al*, 2012, 2010; Sebastian *et al*, 2010; Stadler *et al*, 2014; Van den Bossche *et al*, 2016) and there are diverse biological responses to Plk1 inhibition or knockdown in cancer cells (Choi *et al*, 2015; Craig *et al*, 2014; Driscoll *et al*, 2014; Gjertsen & Schoffski, 2015; McCarroll *et al*, 2015; Medema *et al*, 2011; Rudolph *et al*, 2009; Spankuch-Schmitt *et al*, 2002). These laboratory results are consistent with the results of clinical trials of Plk1 inhibitors in solid tumors that demonstrated striking clinical responses but a low response rate (4–14%), with a stable disease rate of 26–42% in unselected patients (Nokihara *et al*, 2016; Pujade-Lauraine *et al*, 2016; Schoffski *et al*, 2012, 2010; Sebastian *et al*, 2010; Stadler *et al*, 2014; Van den Bossche *et al*, 2016). Up to 11% of patients had stable disease for more than a year (Pujade-Lauraine *et al*, 2016; Sebastian *et al*, 2010). Predictive biomarkers have not been used to select patients likely to respond to Plk1 inhibitors. Plk1 inhibitor sensitivity was found to be associated with *KRAS* and *TP53* mutations in colon, breast, and lung tumors in some studies (Degenhardt *et al*, 2010; Luo *et al*, 2009; Sanhaji *et al*, 2013) but not in others (Ferrarotto *et al*, 2016; Sanhaji *et al*, 2012). We previously compared gene mutation and basal gene and protein expression among 63 NSCLC cell lines and discovered that mesenchymal NSCLC cell lines were more sensitive to Plk1 inhibitors than were epithelial cell lines *in vitro* and *in vivo*; however, *KRAS*, *TP53*, and *MET* mutations did not consistently

1 Department of Thoracic/Head & Neck Medical Oncology, The University of Texas MD Anderson Cancer Center, Houston, TX, USA
2 The University of Texas MD Anderson Cancer Center Graduate School of Biomedical Sciences, Houston, TX, USA
3 Department of Bioinformatics and Computational Biology, The University of Texas MD Anderson Cancer Center, Houston, TX, USA
4 Department of Thoracic and Cardiovascular Surgery, The University of Texas MD Anderson Cancer Center, Houston, TX, USA
*Corresponding author. Tel: +1 713-792-6363; Fax: +1 713-792-1220; E-mail: fmjohns@mdanderson.org
Dr. Ratnakar Singh is currently a postdoctoral fellow at the University of Illinois. Ms. Pavitra Visvanath is currently a graduate student at the University of Utah. Both were employed at The University of Texas MD Anderson Cancer Center at the time this research was performed

predict sensitivity. However, only one NSCLC cell line in the analysis had an activating mutation in exon 14 of *MET* making it impossible to determine whether this molecular subgroup was resistant to Plk1 inhibition. Plk1 inhibitors were equally effective at inhibiting Plk1 in mesenchymal/sensitive and epithelial/resistant NSCLC cell lines (Ferrarotto *et al*, 2016). The mechanisms of resistance to Plk1 inhibitors in epithelial NSCLC remain unknown, and this represents a major gap in knowledge.

To address this gap, in the current study, we performed an integrated analysis of functional proteomics and drug screening in an independent online database of NSCLC cell lines. When this approach confirmed that epithelial-to-mesenchymal transition (EMT)-related proteins correlated significantly with Plk1 inhibitor sensitivity, we used isogenic pairs of epithelial NSCLC cell lines treated with TGF-β to induce a mesenchymal phenotype to measure the changes in protein expression and activation after Plk1 inhibition. We observed differential regulation of cMet phosphorylation after Plk1 inhibition in epithelial and mesenchymal NSCLC. We confirmed cMet's role in Plk1 inhibition–induced apoptosis by inhibiting, silencing, and activating cMet in NSCLC *in vivo* and *in vitro*. Further, Plk1 inhibition decreases vimentin phosphorylation that subsequently regulates cMet phosphorylation via β1-integrin only in mesenchymal NSCLC.

Results

NSCLC cell lines with high cMet and epithelial protein expression are resistant to Plk1 inhibitors *in vitro*

To find pathways that can drive Plk1 inhibitor resistance, we examined data for all NSCLC cell lines from two sources: (i) protein and phosphoprotein expression measured using reverse phase protein array (RPPA) from the MD Anderson Cell Line Project database (Li *et al*, 2017), and (ii) Plk1 inhibitor sensitivity from the Cancer Therapeutics Response Portal v2 (CTRPv2; https://portals.broadinstitute.org/ctrp/) database (Seashore-Ludlow *et al*, 2015). These data were independent of our original study (Ferrarotto *et al*, 2016), although there was some overlap in the drugs and cell lines tested (Appendix Table S1 and Fig S1). Varying numbers of proteins were associated with sensitivity to four Plk1 inhibitors (selected by Spearman's rho coefficient value > 0.3; associated *P*-values are indicated in the figures): 33 proteins were associated with sensitivity to BI2536, 36 with sensitivity to GSK461364, 37 with sensitivity to BRD-K70511574, and 26 with sensitivity to GW-843682X (Fig EV1A–D). Thirty-three proteins were associated with sensitivity to two or more Plk1 inhibitors (Fig 1A). Consistent with our previous findings, we observed that expression of the epithelial proteins E-cadherin ($P < 0.001$) and β-catenin ($P < 0.001$) was higher and expression of the mesenchymal protein Snail ($P < 0.01$), as well as ATM and thymidylate synthase, was lower in cell lines resistant to Plk1 inhibitors than in those sensitive to Plk1 inhibitors. We also found that cMet protein expression correlated with drug sensitivity for all Plk1 inhibitors ($P < 0.01$; Figs 1B and EV1E).

The correlation of drug sensitivity with cMet protein expression motivated us to compare Plk1 inhibitor sensitivity [area under the curve (AUC) and effective dose 50 (ED_{50})] to *MET* gene copy number in NSCLC cell lines. *MET* gene copy number was obtained from the MD Anderson Cell Line Project database, CTRPv2, and Kubo *et al* (2009) in 41, 185, and 29 NSCLC cell lines, respectively. *MET* gene copy number did not correlate with drug sensitivity for any of the 24 possible comparisons (i.e., two measures of drug sensitivity, four drugs, and three sources of *MET* copy number) with Spearman's rho coefficient values that ranged from −0.428 to 0.430 and associated *P*-values that ranged from 0.078 to 0.872. However, this analysis was limited by the fact that there were drug sensitivity data for only two NSCLC cell lines with *MET* copy number > 5.

Induction of a mesenchymal phenotype increases Plk1 inhibition–induced apoptosis

To create isogenic cell line pairs for mechanistic studies, we incubated epithelial/resistant NSCLC cells (H1975, HCC366, and HCC4006) with 5 ng/ml TGF-β for at least 14 days, which led to the expected changes in the expression of vimentin, Snail, Slug, ZEB1, Twist, E-cadherin, β-catenin, and claudin 7 (Fig 2A and Appendix Fig S2). Given that gene mutation did not correlate with Plk1 inhibitor sensitivity (Ferrarotto *et al*, 2016), we chose these cell lines independent of gene mutation status. The induction of a mesenchymal phenotype by TGF-β led to a significant increase in cleaved poly(ADP-ribose) polymerase (PARP) protein expression after Plk1 inhibition with volasertib in all isogenic cell lines (Fig 2B and Appendix Fig S3A). Similarly, TGF-β–treated mesenchymal cells showed increases in volasertib-induced apoptosis as measured by BrdU-positive cells (threefold in H1975, 4.1-fold in HCC4006, and 4.1-fold in HCC366) compared with their epithelial parental cells ($P < 0.05$; Fig 2C). Likewise, volasertib-induced DNA damage was increased in the mesenchymal cell lines compared with the epithelial parental cells (Fig 2B and D, and Appendix Fig S3A), and mesenchymal cell lines were more sensitive to volasertib *in vitro* (Appendix Fig S3B). The Plk1 inhibitor–induced DNA damage (Driscoll *et al*, 2014; Wang *et al*, 2018; Yim & Erikson, 2009) may explain why apoptosis measured by BrdU was more striking than that measured by PARP cleavage. Target inhibition, measured by inhibition of the Plk1 substrate p-NPM (S4), was similar in the isogenic pairs (Appendix Fig S3A).

Activation of cMet is differentially regulated in epithelial and mesenchymal NSCLC cell lines following Plk1 inhibition and knockdown

To elucidate the mechanism for EMT-induced sensitivity to Plk1 inhibition, we analyzed the expression of 301 proteins or phosphoproteins (Kalu *et al*, 2017) after Plk1 inhibition with volasertib for 24 h using RPPA in the three isogenic pairs and two additional mesenchymal/sensitive cell lines (Calu6 and H1792; Fig 3A). To discover the pathway responsible for driving the resistance to Plk1 inhibition, we looked for differentially expressed proteins between epithelial and mesenchymal cell lines after treatment with volasertib. At a cutoff of $P < 0.05$, we observed that the mean expression of 33 proteins or phosphoproteins was differentially regulated (Fig 3B). These data revealed differential effects on both the cMet/FAK/Src axis and the PI3K/Akt pathway (Figs 3B and EV2A). We did a similar analysis using only the parental cell lines to eliminate TGF-β as a confounder, and this led to similar findings (Fig EV2B and C). Western blot analysis confirmed a significant decrease in cMet (Y1234/1235) phosphorylation in sensitive/mesenchymal cells

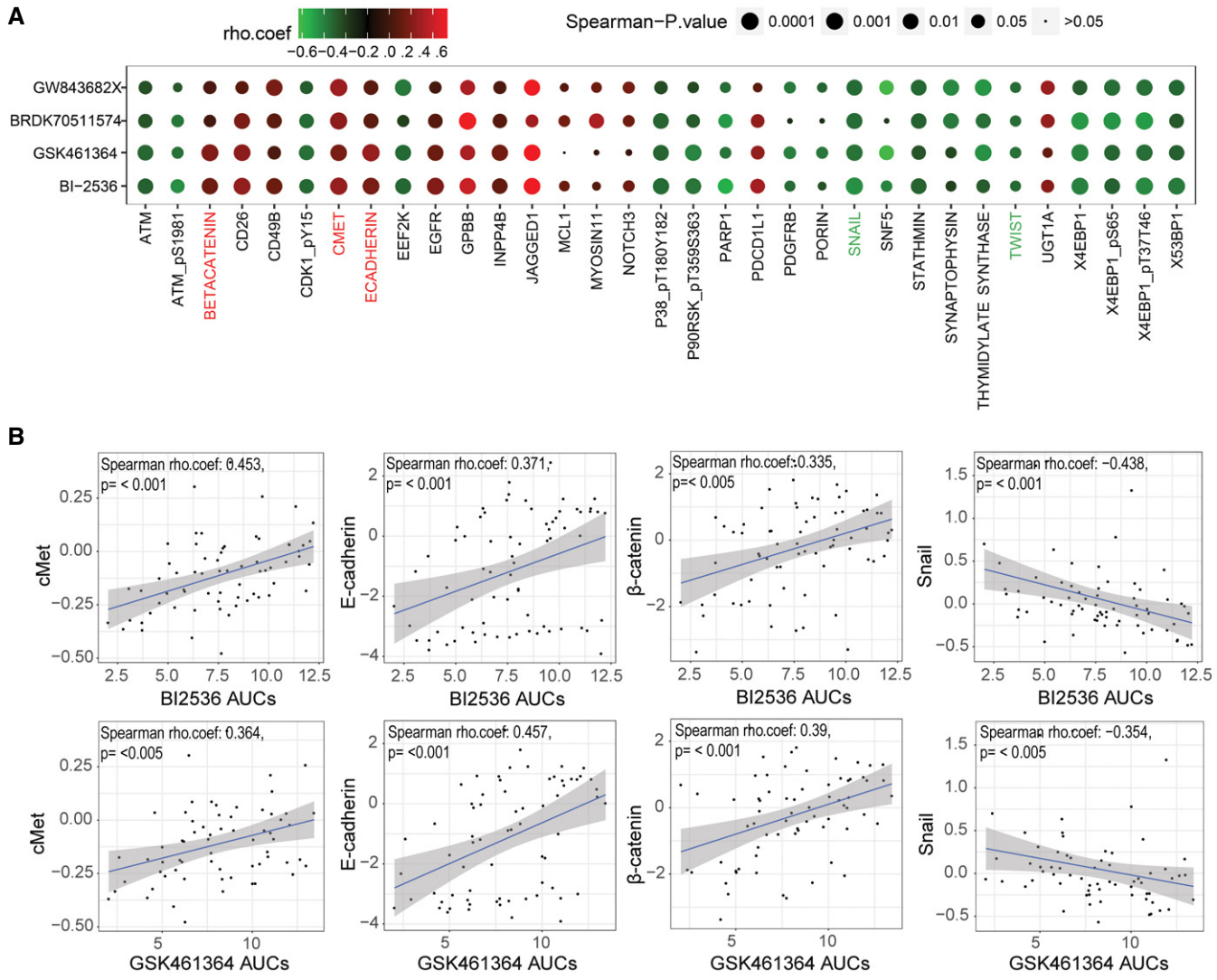

Figure 1. Epithelial-to-mesenchymal transition proteins are associated with sensitivity to Plk1 inhibitors in non–small-cell lung cancer cell lines *in vitro* in an independent dataset.

Spearman's correlations between protein expression and sensitivity to Plk1 inhibitors (BI2536, GSK461364, BRD-K70511574, and GW-843682X), based on data from the Cancer Therapeutics Response Portal v2 database and protein expression data derived from the MD Anderson Cell Line Project database (Li *et al*, 2017).

A Proteins with expression levels that correlate with area under the curve (AUC) values for at least two drugs are included in the graph. The color and size of the data point represent the direction and significance (*P*-value) of the correlation. Red indicates a positive correlation with drug resistance and green a positive correlation with drug sensitivity (i.e., proteins in red are more highly expressed in resistant cell lines).

B AUC values for two Plk1 inhibitors are compared with expression of selected proteins (cMet, E-cadherin, β-catenin, and Snail); each data point represents an individual non–small-cell lung cancer cell line. The gray shaded area represents the 95% confidence interval around the linear regression (blue line). E-cadherin, β catenin, and cMet protein expression correlated with drug resistance.

but not in resistant/epithelial cells after treatment with volasertib (Fig 3C). However, changes in Src (Y416), FAK (Y925), and Akt (S473) were not statistically significant (Fig 3C). As with the RPPA results (Fig EV2A), the average decrease in FAK (Y397) phosphorylation was greater in the mesenchymal cells, but the effects of Plk1 inhibition on the epithelial cells were diverse (Fig 3C). Total cMet, FAK, and Src protein levels were not affected, supporting posttranslational changes. Likewise, when we knocked down Plk1 using siRNA, cMet (Y1234/1235) phosphorylation decreased only in sensitive/mesenchymal cells but not in resistant/epithelial cells with variable effects on pSrc and pFAK (Fig 3D).

Because cMet, FAK, and Src signaling can be bi-directional (Sen *et al*, 2011), we used inhibitors of cMet (tepotinib), FAK (VS6063), Src (dasatinib), and Plk1 (volasertib) to distinguish the properties of this signaling axis in NSCLC cell lines (Fig 3E). Consistent with our RPPA findings, these experiments showed that inhibition of Plk1 inhibits phosphorylation of cMet in the mesenchymal cell line but not in the epithelial one. Phosphorylation of the Plk1 substrate NPM1 was inhibited in both cell lines confirming that efficient target inhibition does not underlie the differential sensitivity. cMet inhibition also inhibited the phosphorylation of FAK in both cell lines, but FAK inhibition did not affect cMet activation. Inhibition of Plk1,

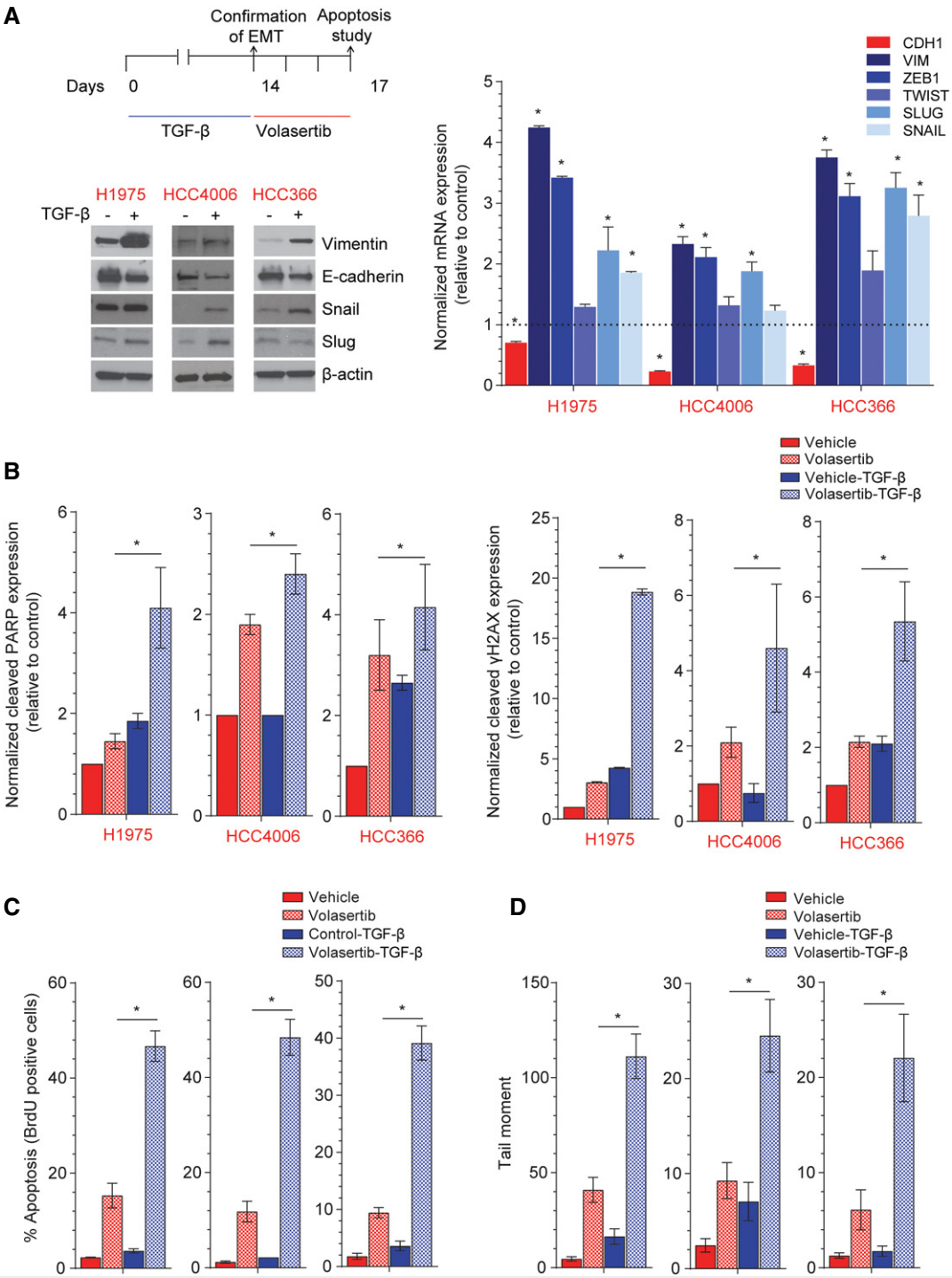

Figure 2. TGF-β–induced mesenchymal phenotype increases sensitivity to Plk1 inhibition.

A Three epithelial/resistant non–small-cell lung cancer cell lines were treated with 5 ng/ml TGF-β for 14 days to induce a mesenchymal phenotype, which was confirmed with Western blot (left) and qPCR (right) analysis of epithelial-to-mesenchymal transition (EMT) markers.

B Parental and TGF-β isogenic cell lines were treated with 50 nM volasertib for 72 h. Cells were then harvested, and lysates were immunoblotted for cleaved PARP and γH2AX proteins that were subsequently quantitated and normalized with β-actin.

C, D Apoptosis was measured by the Apo-BrdU assay (C), and DNA damage was measured by the Comet assay (D).

Data information: Data are means ± standard error of the mean from three independent experiments. Significant differences using two-way analysis of variance with Bonferroni or Benjamini–Hochberg correction for multiple comparison are indicated (*$P < 0.01$).
Source data are available online for this figure.

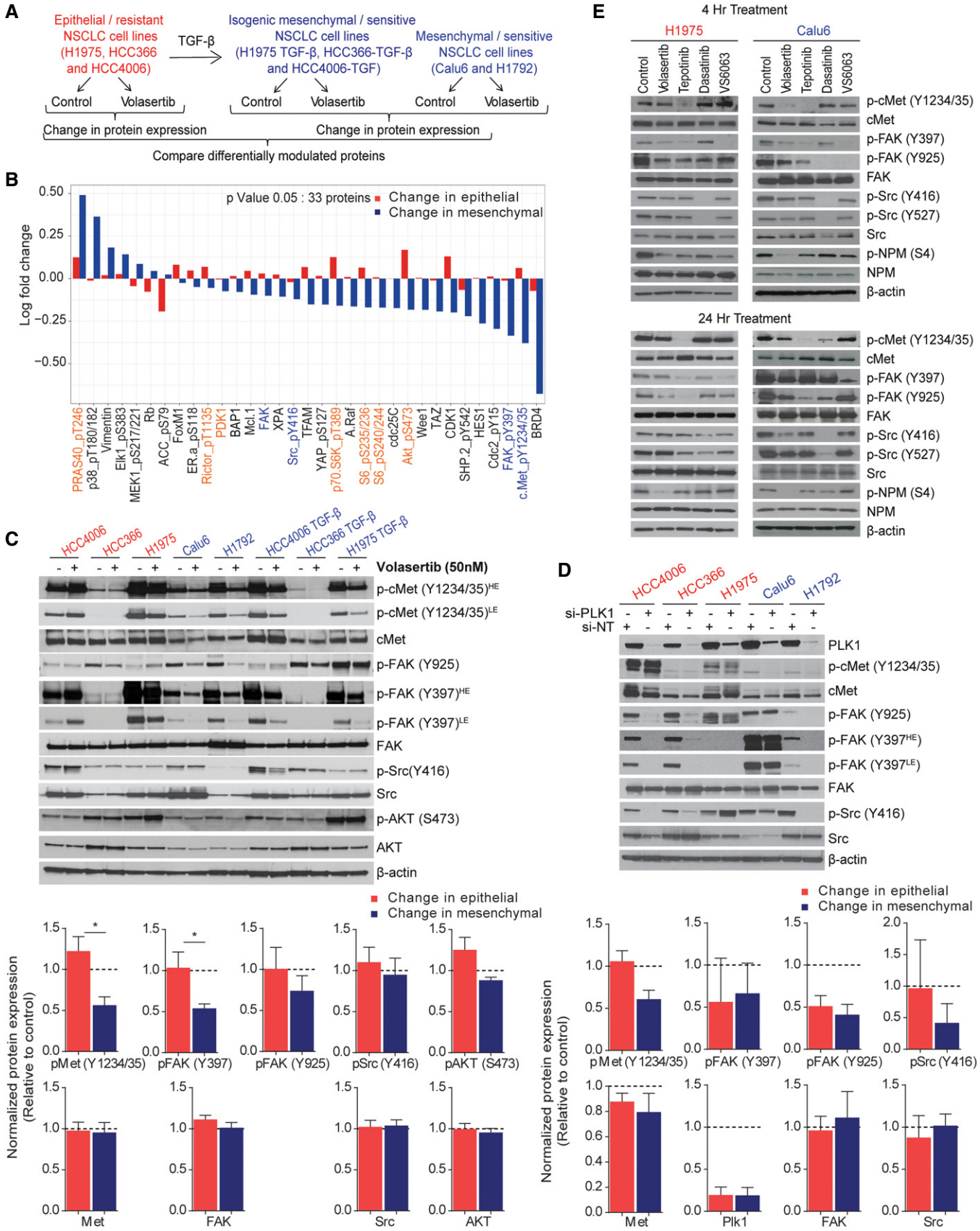
A
Epithelial / resistant NSCLC cell lines (H1975, HCC366 and HCC4006)
TGF-β
Isogenic mesenchymal / sensitive NSCLC cell lines (H1975 TGF-β, HCC366-TGF-β and HCC4006-TGF)
Mesenchymal / sensitive NSCLC cell lines (Calu6 and H1792)
Control
Volasertib
Change in protein expression
Compare differentially modulated proteins
B
p Value 0.05 : 33 proteins
Change in epithelial
Change in mesenchymal
Log fold change
PRAS40_pT246
p38_pT180/182
Vimentin
Elk1_pS383
MEK1_pS217/221
Rb
ACC_pS79
FoxM1
ER.a_pS118
Rictor_pT1135
PDK1
BAP1
Mcl.1
FAK
XPA
Src_pY416
TFAM
YAP_pS127
p70.S6K_pT389
A.Raf
S6_pS235/236
S6_pS240/244
cdc25C
Akt_pS473
Wee1
TAZ
CDK1
SHP.2_pY542
HES1
Cdc2_pY15
FAK_pY397
c.Met_pY1234/35
BRD4
C
HCC4006
HCC366
H1975
Calu6
H1792
HCC4006 TGF-β
HCC366 TGF-β
H1975 TGF-β
Volasertib (50nM)
p-cMet (Y1234/35)HE
p-cMet (Y1234/35)LE
cMet
p-FAK (Y925)
p-FAK (Y397)HE
p-FAK (Y397)LE
FAK
p-Src(Y416)
Src
p-AKT (S473)
AKT
β-actin
Change in epithelial
Change in mesenchymal
Normalized protein expression (Relative to control)
pMet (Y1234/35)
pFAK (Y397)
pFAK (Y925)
pSrc (Y416)
pAKT (S473)
Met
FAK
Src
AKT
D
si-PLK1
si-NT
PLK1
p-cMet (Y1234/35)
cMet
p-FAK (Y925)
p-FAK (Y397HE)
p-FAK (Y397LE)
FAK
p-Src (Y416)
Src
β-actin
Change in epithelial
Change in mesenchymal
Normalized protein expression (Relative to control)
pMet (Y1234/35)
pFAK (Y397)
pFAK (Y925)
pSrc (Y416)
Met
Plk1
FAK
Src
E
4 Hr Treatment
H1975
Calu6
Control
Volasertib
Tepotinib
Dasatinib
VS6063
p-cMet (Y1234/35)
cMet
p-FAK (Y397)
p-FAK (Y925)
FAK
p-Src (Y416)
p-Src (Y527)
Src
p-NPM (S4)
NPM
β-actin
24 Hr Treatment
p-cMet (Y1234/35)
cMet
p-FAK (Y397)
p-FAK (Y925)
FAK
p-Src (Y416)
p-Src (Y527)
Src
p-NPM (S4)
NPM
β-actin

Figure 3.

Figure 3. Activation of cMet is differentially regulated in epithelial and mesenchymal non–small-cell lung cancer (NSCLC) cell lines following Plk1 inhibition and knockdown.

A Three pairs of TGF-β–treated isogenic NSCLC cell lines (H1975, HCC4006, and HCC366) and two mesenchymal NSCLC cell lines (Calu6 and H1792) were incubated with 50 nM volasertib for 24 h, lysed, and subjected to reverse phase protein array analysis. Experiments were done in triplicate.

B Thirty-three proteins were differentially regulated between epithelial and mesenchymal NSCLC cell lines after treatment with volasertib, including those involved in the cMet/FAK/Src signaling axis (blue text) and those involved in the PI3K/Akt signaling axis (orange text).

C The same cell lines treated identically were subjected to immunoblotting for the indicated proteins (upper) with densitometric quantification normalized with β-actin (lower).

D Epithelial (red text) and mesenchymal (blue text) NSCLC cell lines transfected with 10 nM siRNA as indicated for 48 h and subjected to Western blotting with the indicated antibodies (upper) with densitometric quantification normalized with β-actin (lower). NT, non-targeting control.

E H1975 and Calu6 cells were treated with indicated inhibitors for 4 h or 24 h. Cells were then harvested, and lysates were immunoblotted for the indicated proteins.

Data information: Data are means ± standard error of the mean from three independent experiments. Significant differences using two-sided Student's *t*-test are indicated by $*P < 0.05$.
Source data are available online for this figure.

FAK, or cMet only minimally affected Src activation. Src inhibition decreased phosphorylation of FAK (Y925) but did not significantly affect phosphorylation of cMet or FAK (Y397). Together, these results support a model in which Plk1 is robustly inhibited in all NSCLC cell lines, but only inhibits cMet phosphorylation in mesenchymal NSCLC lines.

The combination of Plk1 and cMet inhibition or knockdown enhances apoptosis in NSCLC cells

To test the hypothesis that cMet inhibition is important for Plk1 inhibitor–induced apoptosis, we treated eight NSCLC cell lines with a combination of volasertib and tepotinib for 72 h and measured viability (Fig 4A). To inhibit cMet, we chose tepotinib, which has been tested in NSCLC patients (Friese-Hamim *et al*, 2017; Reungwetwattana *et al*, 2017). We used relevant drug concentrations as defined by pharmacokinetic data and target inhibition data. Specifically, 400 nM tepotinib fully inhibits cMet in intact NSCLC cells (Bladt *et al*, 2013). Results of *in vitro* kinase assays with 242 kinases showed that only cMet had half-maximal inhibitory concentration values of less than 600 nM (Bladt *et al*, 2013). None of the cell lines used in this research harbor *MET* mutations or *MET* amplification. A synergistic or additive effect was observed in seven of eight cell lines (Fa = 0.5; Fig 4B and Appendix Table S2). Likewise, the combination led to more apoptosis than did single-agent treatment in two epithelial and two mesenchymal cell lines, as measured by BrdU, cleaved PARP, and cleaved caspase 3 (Fig 4C and D). We also observed higher DNA damage (γ-H2AX expression) in all cell lines after treatment with the combination compared with single-agent treatment or controls (Fig 4D).

We also assessed colony formation in these cells after 24 h of treatment with vehicle control, volasertib, tepotinib, or the combination followed by drug-free incubation for 12–15 days. The combination treatment significantly decreased the number and size of colonies in all cell lines tested compared with control or single-agent treatment, although, consistent with our prior results, Plk1 inhibition alone was effective in mesenchymal NSCLC cell lines (Fig 4E and Appendix Fig S4).

To demonstrate the specificity of Plk1 inhibitors, we knocked down *PLK1* and *MET* expression in NSCLC cell lines using siRNA for 48 h (Fig 4A) and observed a significant increase in apoptosis compared with non-targeting control and single-gene silencing (Fig 4F). Consistent with our inhibitor studies, silencing of Plk1 alone significantly increased the percentage of apoptotic cells in mesenchymal cell lines, and we observed persistent cMet (Y1234/1235) phosphorylation in epithelial/resistant cell lines and decreased cMet activation in mesenchymal/sensitive cell lines (Fig 4G). All tested cell lines demonstrated significant increases in expression of cleaved PARP, cleaved caspase 3, and γ-H2AX in combination silencing compared with non-targeting control or single-gene silencing (Fig 4G). These results demonstrate that simultaneous inhibition or silencing of cMet potentiates the apoptotic effect of Plk1 inhibition or silencing in NSCLC.

Inhibition of both Plk1 and cMet is more effective than inhibition of either target alone *in vivo* in NSCLC cell line and patient-derived xenograft (PDX) models

Encouraged by the *in vitro* activity, we next investigated the *in vivo* effect of Plk1 and cMet inhibition for the treatment of lung cancer in PDX and cell line xenograft models of NSCLC (Hao *et al*, 2015). We selected both epithelial (TC402) and mesenchymal (TC424) PDX and cell line models. We confirmed the xenografts' EMT status by checking the expression of EMT-related genes (Fig EV3A).

When tumors reached 150 mm^3, mice were randomized into one of four treatment groups: vehicle control, volasertib, tepotinib, or the combination of volasertib and tepotinib. Volasertib alone resulted in a significant reduction in tumor growth compared with vehicle control or tepotinib alone in both models. As expected, volasertib reduced tumor size more significantly in the mesenchymal than in the epithelial models (Figs 5A and B, and EV3B). Specifically, volasertib alone led to tumor regression (i.e., tumor smaller than at the start of the experiment) in eight of 10 mesenchymal PDX mice, with an overall −26.5% regression in tumor volume relative to day zero (immediately prior to starting treatment). In contrast, volasertib alone led to tumor regression in only one of 10 epithelial PDX mice and overall tumor size increased by 156% compared with day zero (Figs 5B and EV3C). Likewise, in cell line xenografts (Fig EV3D), Calu6 (mesenchymal) cells showed a better response than did H1975 (epithelial) cells when treated with volasertib alone, although tumors did not regress in either model (Figs 5C and D, and EV3E).

The combination of Plk1 and cMet inhibitors led to tumor regression in both of the PDX models that was statistically significant starting on day 7 ($P < 0.05$). The combination therapy led to tumor regression in nine of 10 epithelial and nine of 10 mesenchymal PDX mice (Figs 5B and EV3C). Likewise, both cell line models showed a significant reduction in tumor growth when the mice were treated with the combination compared with control and with tepotinib alone

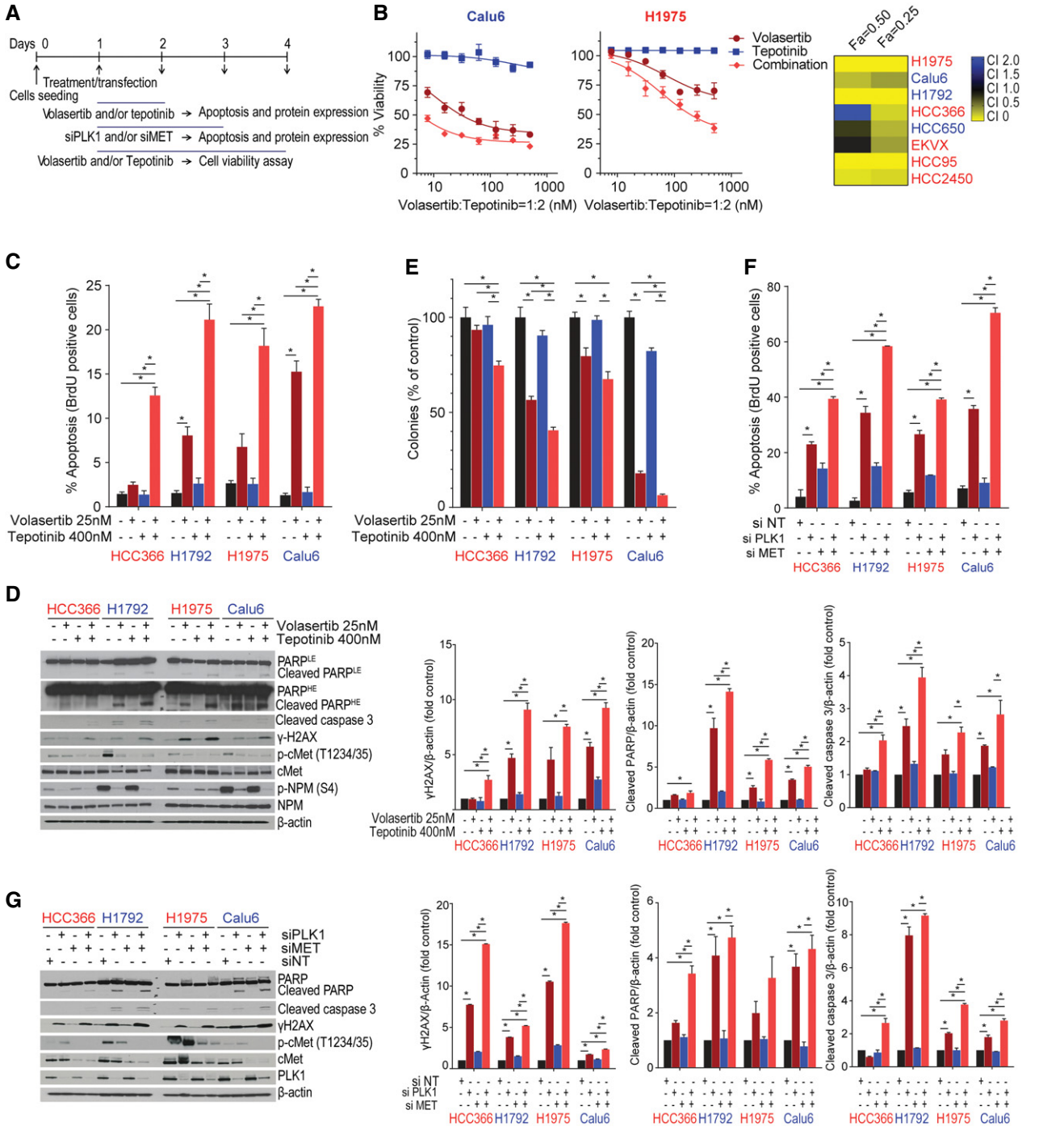

Figure 4. Co-targeting of cMet and Plk1 enhances apoptosis in non–small-cell lung cancer (NSCLC) *in vitro*.

A Schematic of the experimental plan for Plk1 and cMet inhibition/silencing for viability and apoptosis studies in mesenchymal and epithelial NSCLC cell lines.

B Cell viability was measured using CellTiter-Glo in NSCLC cell lines treated with volasertib, tepotinib, or a 1:2 ratio of both for 72 h. Left: representative cell viability graph of cells treated with the indicated drugs. Right: heatmap depicting the calculated combination indices at Fa = 0.25 and Fa = 0.5.

C Apoptosis was measured using the Apo-BrdU assay in the indicated cell lines treated with the indicated drugs for 24 h.

D Immunoblots from cells treated with indicated drugs for 24 h (left) with densitometric quantification normalized with β-actin (right).

E All tested cell lines were treated as indicated for 24 h and allowed to grow in drug-free medium for 15–20 days to form colonies, which were counted using ImageJ.

F Apoptosis was measured using the Apo-BrdU assay in the indicated cell lines transfected with 10 nM siRNA as indicated for 48 h. NT, non-targeting control.

G Immunoblots from cells transfected with siRNA as indicated for 48 h (left) with densitometric quantification normalized with β-actin (right).

Data information: Data are means ± standard error of the mean from three independent experiments. Significant differences using two-way analysis of variance with Bonferroni or Benjamini–Hochberg (BH) correction for multiple comparison are indicated (*$P < 0.01$). Mesenchymal and epithelial NSCLC cell lines are indicated in blue and red text, respectively.

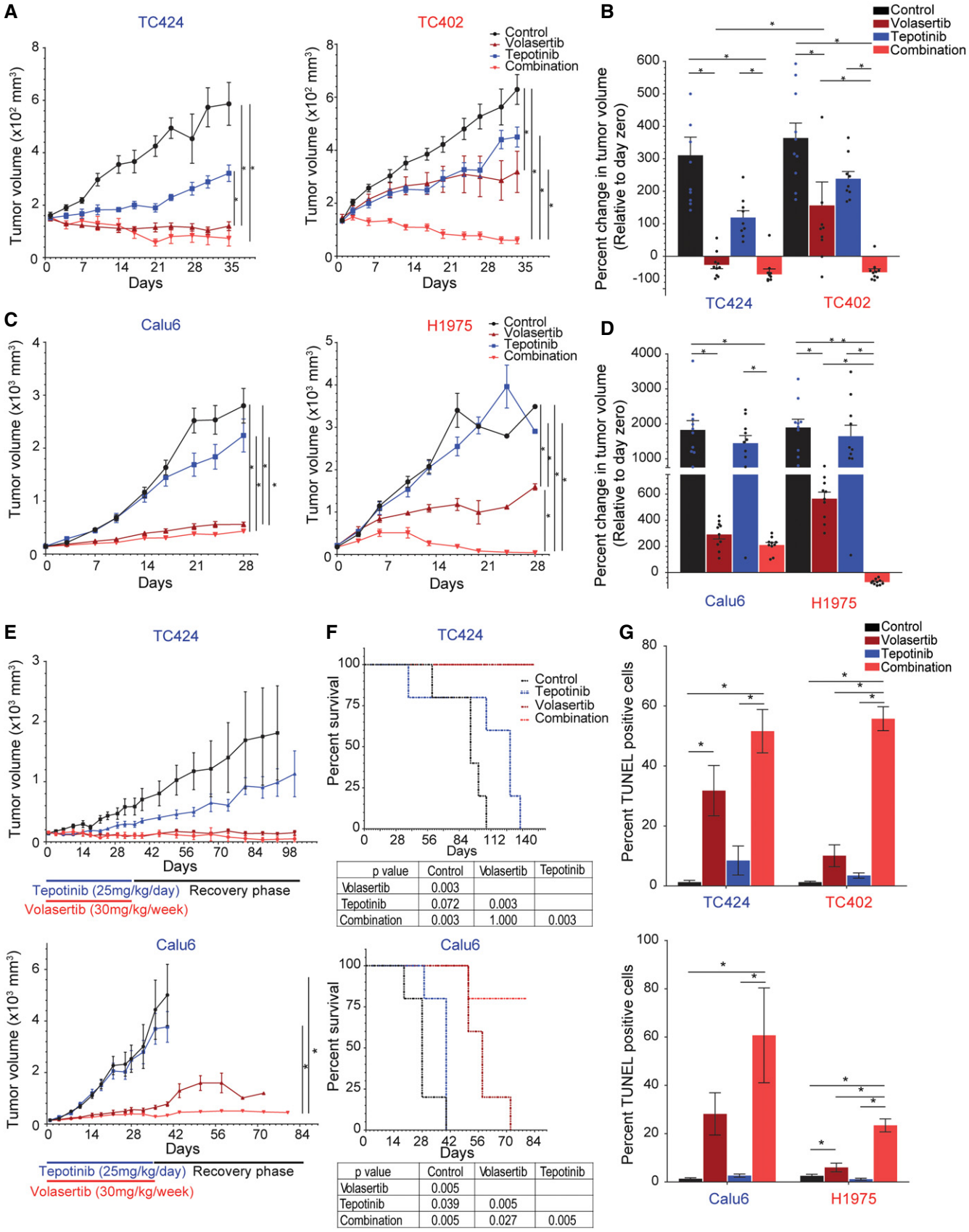

p value	Control	Volasertib	Tepotinib
Volasertib	0.003		
Tepotinib	0.072	0.003	
Combination	0.003	1.000	0.003

p value	Control	Volasertib	Tepotinib
Volasertib	0.005		
Tepotinib	0.039	0.005	
Combination	0.005	0.027	0.005

Figure 5.

Figure 5. Co-targeting of cMet and Plk1 induces apoptosis and reduces tumor size in non–small-cell lung cancer.

A–D Mice bearing epithelial (red text) and mesenchymal (blue text) non–small-cell lung cancer tumors were treated with vehicle control, volasertib (30 mg/kg per week intravenously), tepotinib (25 mg/kg per day orally), or the combination for 5 weeks to generate tumor growth curves of patient-derived xenografts (PDX; A) and cell line xenografts (C). The percent change in tumor volume at the end of treatment (normalized to day zero) was calculated with each data point representing an individual mouse, and the bar is the mean value ± standard error of 10 mice for each group (B, D).

E Tumor growth curve of mesenchymal PDX TC424 (top) and cell line xenograft Calu6 (bottom) upon treatment for 5 weeks and after cessation of treatment (recovery phase). Data are means ± standard error of the mean from five mice for each group.

F Kaplan–Meier survival curves for mesenchymal PDX TC424 (top) and cell line xenograft Calu6 (bottom) with death due to excessive tumor burden as the endpoint.

G Quantification of TUNEL-positive cells in paraffin-embedded xenograft tissue sections. Data are means ± standard error of the mean from six mice for each group.

Data information: Significant differences using two-way analysis of variance with Bonferroni or Benjamini–Hochberg correction for multiple comparisons are indicated. *$P < 0.01$.
Source data are available online for this figure.

($P < 0.05$; Fig 5D). All 10 of the mice bearing the epithelial xenograft showed tumor regression (Figs 5D and EV3F). In the mesenchymal xenograft, the combination was slightly more effective than volasertib alone, but this difference did not reach statistical significance. In both cell line models, mice in the combination arm showed a significant improvement in survival compared with control; volasertib alone improved the survival of mice bearing mesenchymal NSCLC (Fig EV3G). The combination treatment was well tolerated in all mice with no change in body weight over time (Fig EV3H).

To investigate the ability of treated tumors to recover, we treated mice bearing mesenchymal NSCLC for 5 weeks, then stopped drug treatment and examined the mice for tumor growth. The tumors in the mice treated with vehicle control or tepotinib continued to grow steadily. In contrast, tumors remained the same size in both the volasertib-only and combination treatment groups, with the exception of modest tumor growth in the volasertib-only Calu6-bearing mice (Fig 5E). The volasertib-only and combination treatment groups had significantly longer survival compared with other groups in both models ($P < 0.01$; Fig 5F).

To asses for apoptosis, we next performed TUNEL staining in paraffin-embedded tissues (Fig 5G). Similar to the *in vitro* finding, volasertib alone resulted in a larger increase in TUNEL-positive cells in the mesenchymal xenograft models (TC424 and Calu6) than in the epithelial xenograft models (TC202 and H1975). Co-treatment with Plk1 and cMet inhibitors significantly increased the percentage of TUNEL-positive cells in all mouse models. Taken together, these results support cMet as a driver of Plk1 inhibitor resistance in epithelial NSCLC *in vivo*, and the findings suggest that co-inhibition of Plk1 and cMet increases apoptosis, leading to tumor regression in NSCLC.

Constitutive activation of cMet abrogates Plk1 inhibition–induced apoptosis in mesenchymal NSCLC cell lines

To test cMet as a driver of resistance, we used constitutively active TPR-Met, which is a fusion protein that lacks the extracellular, transmembrane, and juxtamembrane domains of the cMet receptor and includes the TPR dimerization motif, which allows constitutive and ligand-independent activation of the kinase. Expression of the TPR-Met chimeric protein was biologically active in three mesenchymal cell lines (Calu6, H157, and H1355), which in turn increased downstream Akt (S473) and Erk (p42/44 T202/204) phosphorylation (Fig EV4A).

Compared with the control vector–transfected cells, TPR-Met–expressing cells showed less apoptosis, as measured by Apo-BrdU, cleaved PARP, and cleaved caspase 3, after treatment with volasertib (Fig 6A and B). Likewise, expression of TPR-Met increased resistance to Plk1 inhibition compared with control vector, as measured by colony formation (Figs 6C and EV4B) assays and CellTiter-Glo (Fig EV4C).

To determine whether we could overcome the effects of cMet activation by using a cMet inhibitor, we combined tepotinib and volasertib. Tepotinib inhibited cMet universally but did not completely abrogate cMet signaling in the TPR-Met–expressing cell lines. The addition of tepotinib significantly increased apoptosis in control vector–transfected cells, but apoptosis was only moderately increased in TPR-Met–transfected cells, consistent with a lack of full cMet inhibition (Fig 6A and B). The combination of volasertib and tepotinib significantly reduced the clonogenic potential compared with single-agent treatment in both control and TPR-Met–transfected cell lines (Fig 6C). Taken together, these results support cMet as a driver of Plk1 inhibitor sensitivity in mesenchymal NSCLC.

The ability of constitutively active TPR-Met to mediate resistance to Plk1 inhibition led us to ask whether Plk1 inhibition would affect cMet activation in NSCLC with constitutively active cMet. To test this hypothesis, we inhibited Plk1 in mesenchymal NSCLC cell lines with *MET* amplification and a *MET* exon 14 skipping mutation (Fig 6D). In both the cell line with marked *MET* amplification (H920, copy number 16.4) and the one with an activating *MET* mutation (H596), volasertib did not lead to a decreased in pMet. Both H596 and H920 were resistant to the Plk1 inhibition GSK461364 (Ferrarotto *et al*, 2016).

Acquired resistance to volasertib leads to a mesenchymal-to-epithelial transition and decreased Plk1 inhibitor–mediated cMet inhibition

To study the molecular mechanism by which acquired resistance to volasertib emerges, we exposed the Calu6 cell line to increasing concentrations of the drug over time until resistance emerged (Fig 7A). The resulting Calu6-VAR (volasertib acquired resistance) cell line showed an epithelial morphology (Fig 7B), increased expression of E-cadherin, and decreased expression of vimentin compared with the parental cell line. Similar to the protein changes, mRNA expression also showed about a 70-fold increase in *CDH1* ($P < 0.01$) and a decrease in the mesenchymal genes *VIM* (0.1-fold), *ZEB1* (0.001-fold), *TWIST* (0.3-fold), and *SNAIL* (0.001-fold; $P < 0.01$) compared with the parental cell line (Fig 7C). We did not observe any significant change in basal cMet or p-cMet (Y1234/1235) protein expression in Calu6-VAR cells compared with parental cells. We observed persistent p-cMet (Y1234/1235) phosphorylation

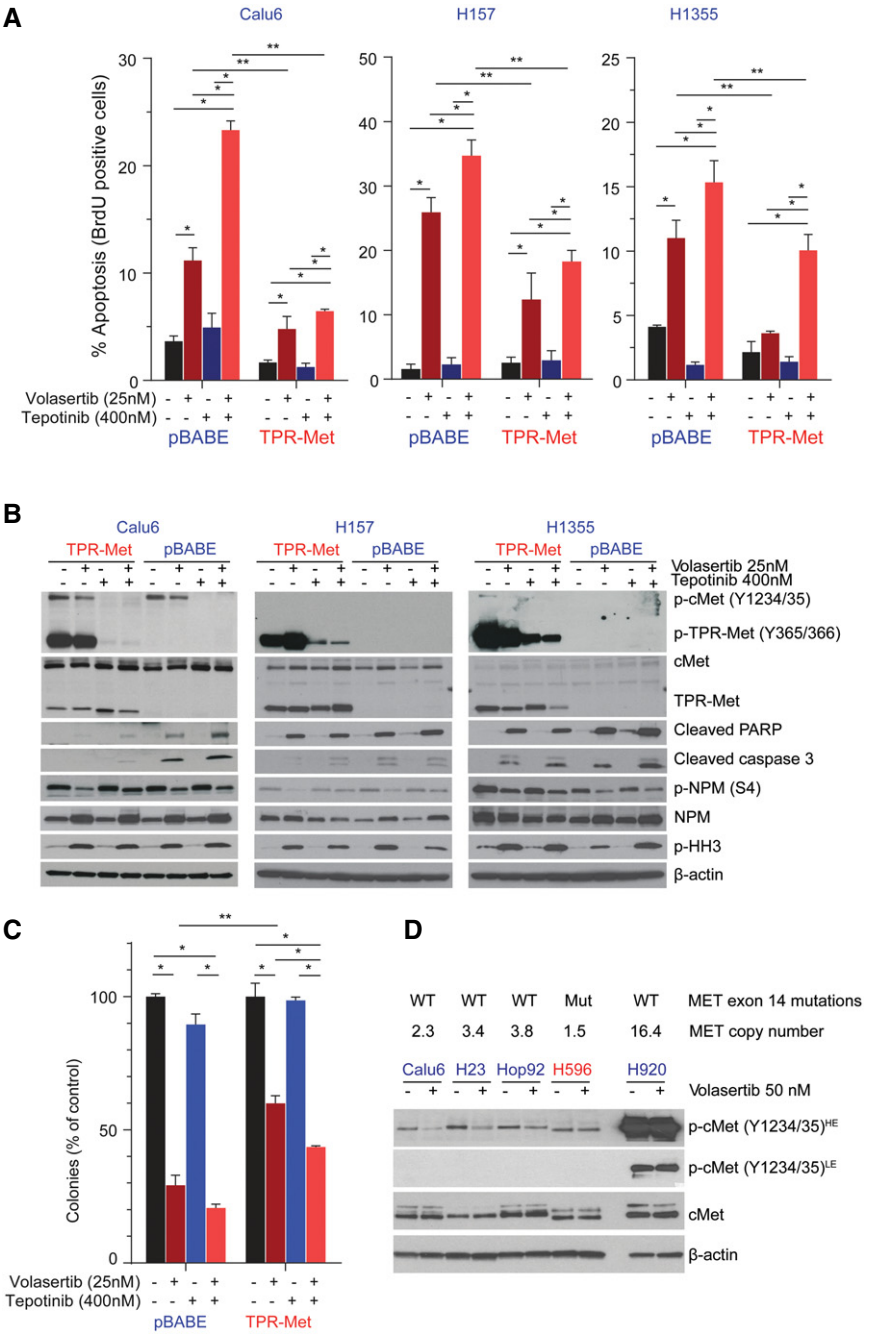

Figure 6. Constitutively active cMet expression reduces sensitivity to Plk1 inhibition.

A Calu6, H157, and H1355 TPR-Met–expressing or vector control (pBABE)–expressing cells were treated as indicated for 24 h, and apoptosis was measured using the Apo-BrdU assay.

B Parental and TPR-Met–expressing cell lines were treated with the indicated drugs for 24 h. Cells were then harvested, and lysates were immunoblotted for the indicated proteins. β-Actin was used as a loading control.

C Parental and TPR-Met–expressing cell lines were treated as indicated for 24 h and allowed to grow in drug-free medium for 15–20 days to form colonies, which were counted using ImageJ.

D Mesenchymal NSCLC cell lines with the noted *MET* alterations were incubated with 50 nM volasertib for 4 h and subjected to immunoblotting with the indicated antibodies.

Data information: (A and C) Data are means ± standard error of the mean from three independent experiments. Significant differences using two-way analysis of variance with Bonferroni or Benjamini–Hochberg correction for multiple comparisons are indicated. *$P < 0.05$. **$P < 0.01$.
Source data are available online for this figure.

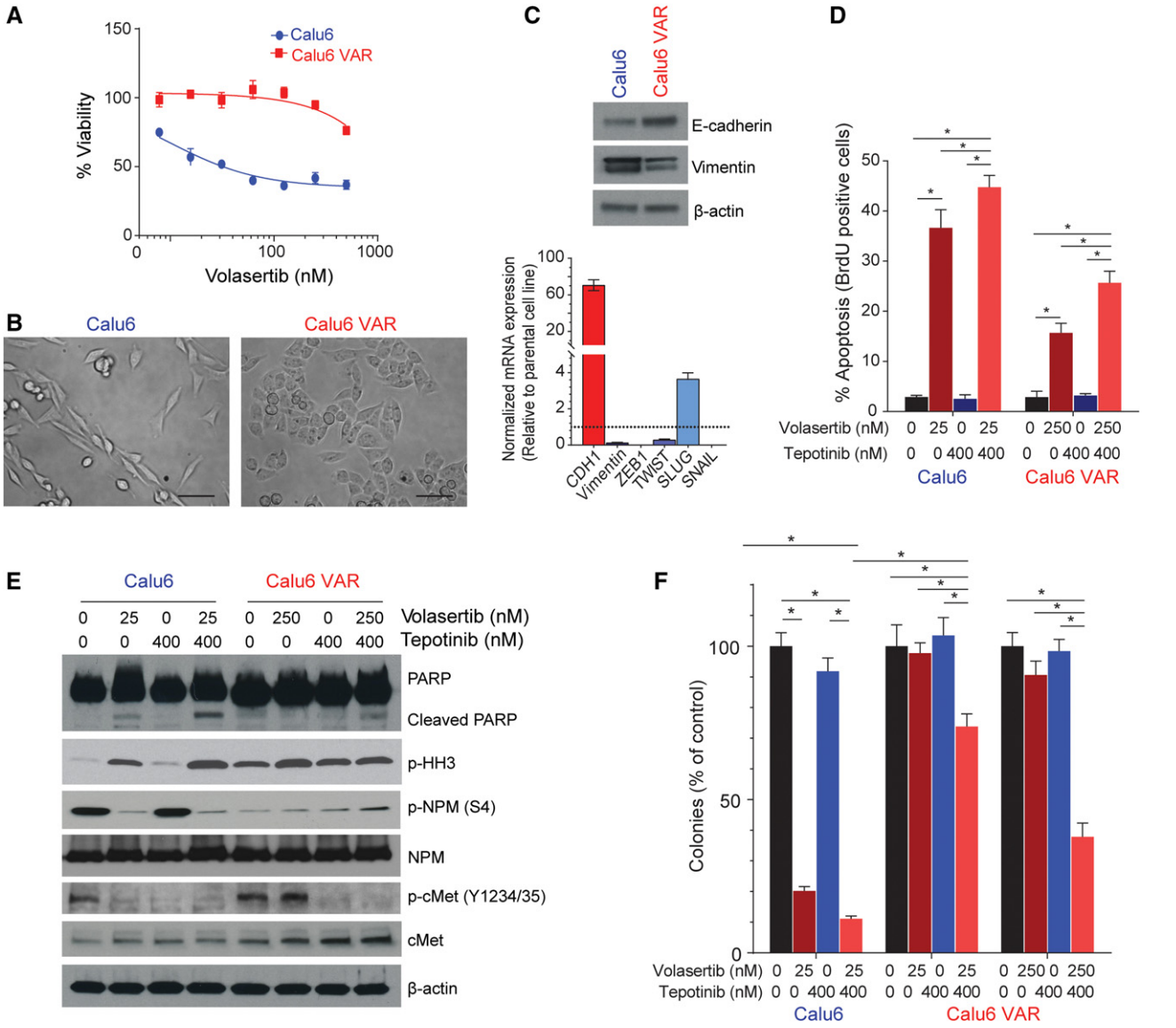

Figure 7. The volasertib acquired resistance (VAR) cell line shows mesenchymal-to-epithelial transition and persistent cMet phosphorylation.

A Cell viability measured by CellTiter-Glo in Calu6 parental and Calu6-VAR cells treated with different concentrations of volasertib for 72 h.

B Micrograph shows acquisition of a mesenchymal-to-epithelial transition phenotype in VAR cells. Scale bar: 100 μm.

C Basal protein and mRNA expression in parental and VAR cells for the indicated proteins was measured using immunoblotting (upper) and reverse-transcription PCR (lower), with GAPDH expression used for normalization.

D Parental and VAR cells were treated as indicated for 48 h, and apoptosis was measured using the Apo-BrdU assay.

E Parental and VAR cells were treated with the indicated drug concentrations for 48 h. Cells were then harvested, and lysates were immunoblotted for the indicated proteins.

F Parental and VAR cells were treated as indicated for 24 h and allowed to grow in drug-free medium for 15–20 days to form colonies, which were counted using ImageJ.

Data information: Data are means ± standard error of the mean from three independent experiments. Significant differences using two-way analysis of variance with Bonferroni or Benjamini–Hochberg correction for multiple comparisons are indicated. *$P < 0.01$.
Source data are available online for this figure.

after treatment with volasertib in Calu6-VAR cells, as well as in cell lines with *de novo* resistance.

The differential effects on cMet activation led us to analyze the effect of co-targeting Plk1 and cMet with volasertib and tepotinib on apoptosis and cell viability. Plk1 inhibition alone led to less apoptosis in Calu6-VAR cells than in parental cells ($P < 0.01$), as measured by Apo-BrdU and cleaved PARP (Fig 7D and E). Simultaneous inhibition of both cMet and Plk1 significantly increased the percentage of apoptotic BrdU-positive cells and PARP cleavage compared with single-agent treatment ($P < 0.05$) in both parental

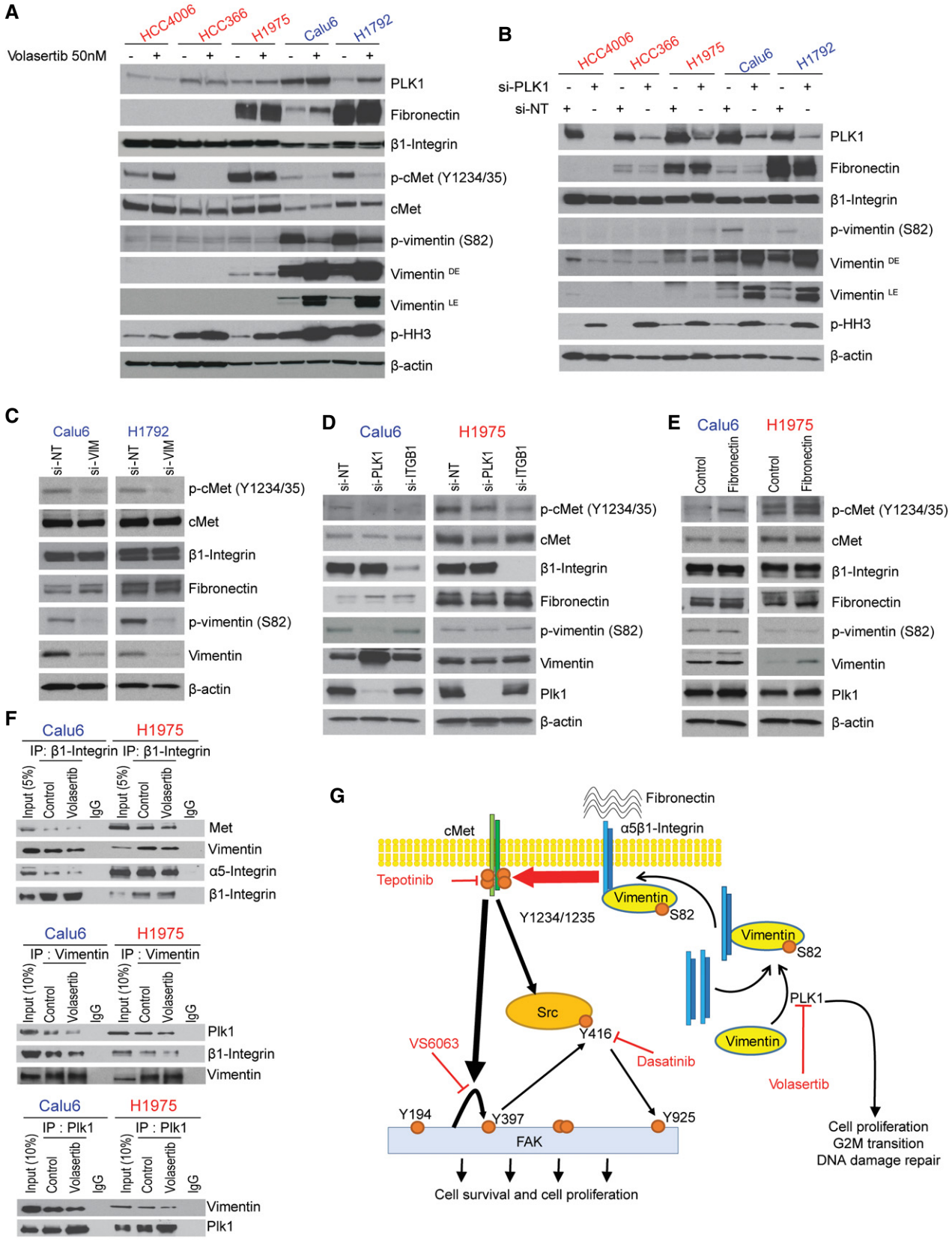

Figure 8.

Figure 8. Plk1 inhibition or silencing decreases vimentin phosphorylation and regulates cMet phosphorylation via β1-integrin.

A Epithelial and mesenchymal non–small-cell lung cancer (NSCLC) cell lines after treatment with 50 nM volasertib for 24 h. Cells were then harvested, and lysates were immunoblotted for the indicated proteins.

B Epithelial and mesenchymal NSCLC cell lines after Plk1 silencing with siRNA for 48 h. Cells were then harvested, and lysates were immunoblotted for the indicated proteins.

C Calu6 and H1792 mesenchymal NSCLC cell lines after *VIM* silencing with siRNA for 48 h. Cells were then harvested, and lysates were immunoblotted for the indicated proteins.

D Calu6 (mesenchymal) and H1975 (epithelial) NSCLC cell lines after *PLK1* and *ITGB1* silencing with siRNA for 48 h. Cells were then harvested, and lysates were immunoblotted for the indicated proteins.

E Calu6 (mesenchymal) and H1975 (epithelial) NSCLC cell lines after treatment with fibronectin for 24 h. Cells were then harvested, and lysates were immunoblotted for the indicated proteins.

F Calu6 and H1975 NSCLC cell lines after treatment with 50 nM volasertib for 24 h. Cells were then harvested, and lysates were immunoprecipitated (IP) using β1-integrin, vimentin, and Plk1 antibodies, then immunoblotted for the indicated proteins.

G Schematic summary of the proposed mechanism by which cMet drives primary and acquired resistance to volasertib in NSCLC and possible treatment combinations to overcome this resistance.

Source data are available online for this figure.

and Calu6-VAR cells (Fig 7D and E). We also assessed the colony formation of these cells after 24 h of treatment with vehicle control, volasertib, tepotinib, or both followed by drug-free incubation for 12–15 days. Volasertib alone was not effective in Calu6-VAR cells, but combination treatment significantly decreased the number of colonies with both low (25 nM) and high (250 nM) concentrations of volasertib ($P < 0.01$; Fig 7F and Appendix Fig S5A). Likewise, CellTiter-Glo analysis showed more sensitivity when Calu6 parental and Calu6-VAR cells were treated with the combination of volasertib and tepotinib compared with single-agent treatment (Appendix Fig S5B).

Plk1 inhibition or silencing decreases vimentin phosphorylation and regulates cMet phosphorylation via β1-integrin trafficking

To determine whether cMet inhibition following Plk1 inhibition is ligand-dependent, we measured hepatocyte growth factor (HGF) in conditioned medium and in cellular lysates after Plk1 inhibition in both mesenchymal and epithelial cell lines. Neither the secreted nor cellular HGF levels were affected by Plk1 inhibition in all tested NSCLC cell lines (Fig EV5A). Likewise, an HGF neutralizing antibody did not affect basal cMet activation or Plk1 inhibition–induced cMet inhibition in the mesenchymal NSCLC cell line Calu6. In a second mesenchymal NSCLC cell line (H1792), the HGF neutralizing antibody did reduce basal cMet activation consistent with cancer cell production of HGF leading to cMet activation that has previously been well established in some NSCLC tumors (Salgia, 2017). In H1792 cells, the combination of the HGF neutralizing antibody and Plk1 inhibition had an additive effect on cMet activation (Fig EV5B).

We next investigated the interaction of cMet, Plk1, β1-integrin (*ITGB1*), and vimentin (*VIM*) because this is a ligand-independent pathway that involves proteins associated with EMT. Plk1 maintains cell surface levels of β1-integrin via phosphorylation of vimentin on S82 (Rizki *et al*, 2007). β1-integrin can form a heterodimer complex with cMet, resulting in ligand-independent cross-activation invasive oncologic processes (Jahangiri *et al*, 2017). We hypothesized that Plk1 regulates vimentin phosphorylation, which in turn regulates the β1-integrin trafficking to the membrane and maintains cMet phosphorylation in a ligand-independent manner. Because mesenchymal cells have higher vimentin levels than epithelial cells do, cMet activation using this pathway would be more significant in mesenchymal cells than in epithelial cells. To test this hypothesis, we first checked the expression of vimentin and β1-integrin in NSCLC cell lines. As expected, we observed a significant positive correlation between expression of mesenchymal markers, according to an EMT score (Byers *et al*, 2013), and expression of *ITGB1* ($r = 0.528$, $P < 0.001$) and *VIM* ($r = 0.777$, $P < 0.001$; Fig EV5C).

We then tested the effect of Plk1 inhibition or silencing on vimentin (S82) phosphorylation. Inhibition or silencing of Plk1 by volasertib or siRNA markedly decreased the S82 vimentin phosphorylation in two mesenchymal cell lines. The resulting increase in total vimentin may be a compensatory change. Vimentin levels were very low in epithelial cell lines without consistent effects by Plk1 inhibition (Fig 8A and B); total β1-integrin levels were not affected.

To test the role of vimentin, we silenced it in two mesenchymal cell lines, which led to a decrease in cMet phosphorylation at Y1234/1235 (Fig 8C), supporting the role of vimentin in cMet activation. We also observed an increase in cleaved PARP and caspase 3 expression when silencing of vimentin was followed by treatment with volasertib in these cell lines compared with cells treated with volasertib alone (Fig EV5D). Knockdown of vimentin or treatment with volasertib did not affect the expression of total levels of β1-integrin, cMet, or fibronectin (Figs 8C and EV5D).

To confirm the involvement of β1-integrin in cMet phosphorylation, we manipulated β1-integrin levels by siRNA and β1-integrin activation with fibronectin. Knocking down *ITGB1* in both epithelial and mesenchymal cell lines led to a decrease in cMet phosphorylation (Figs 8D and EV5E), demonstrating that this axis is intact in both cell types. Co-silencing of *Plk1* and *ITGB1* led to an increase in cleaved PARP and cleaved caspase 3 expression compared with *Plk1* silencing alone (Fig EV5E). Consistent with these results, treatment with fibronectin led to an increase in cMet phosphorylation in both epithelial and mesenchymal NSCLC cell lines (Fig 8E). Fibronectin was not able to abrogate Plk1 inhibitor–induced cMet inactivation and likewise had no effect in rescuing the cells from apoptosis by volasertib (Fig EV5F), likely because of a lack of available cell surface β1-integrin. Manipulation of β1-integrin did not affect the total levels of cMet, Plk1, or vimentin.

Next, we investigated the interaction between Plk1, vimentin, β1-integrin, and cMet in NSCLC cell lines after treatment with volasertib. Plk1, vimentin, and β1-integrin were immunoprecipitated from volasertib-treated and volasertib-untreated Calu6 and H1975 cell lysates, and immunoprecipitated protein was resolved by SDS–

PAGE and probed for Plk1, vimentin, β1-integrin, and cMet. Results in Fig 8F show that vimentin co-immunoprecipitated with Plk1. A reverse immunoprecipitation was performed, and Plk1 was found to co-immunoprecipitate with vimentin in both NSCLC lines. Similarly, β1-integrin co-immunoprecipitated with vimentin and vimentin co-immunoprecipitated with β1-integrin. We also observed that cMet co-immunoprecipitated with β1-integrin. Altogether, these findings confirm that cMet phosphorylation is regulated by Plk1-mediated vimentin phosphorylation via β1-integrin in these cells (Fig 8G).

Discussion

The current study yielded five main findings that follow from our prior discovery that mesenchymal NSCLC is more sensitive to Plk1 inhibitors than epithelial NSCLC (Ferrarotto *et al*, 2016). First, Plk1 inhibitor sensitivity correlates with cMet and EMT protein expression in a large, independent dataset, validating our prior study. Second, cMet phosphorylation is differentially regulated after Plk1 inhibition in epithelial and mesenchymal NSCLC. Third, pharmacologic and genetic manipulation of cMet affects Plk1 inhibitor–induced apoptosis, establishing this pathway as a bona fide mechanism of resistance. This conclusion was further supported by the finding that a cell line with acquired resistance to Plk1 inhibition showed mesenchymal-to-epithelial transition and persistent cMet phosphorylation after Plk1 inhibition, similar to cells with *de novo* resistance. Fourth, this resistance pathway functions *in vivo*; significant tumor regression was demonstrated in multiple NSCLC models treated with clinically relevant drugs. Finally, the sensitivity of mesenchymal NSCLC cells to Plk1 inhibition is linked to cMet phosphorylation via the vimentin and β1-integrin pathway (a ligand-independent and understudied pathway), leading to cMet activation in NSCLC.

Our work has important clinical implications for the treatment of NSCLC. Previously, we demonstrated that 63 NSCLC cell lines have diverse sensitivities to Plk1 inhibition (Ferrarotto *et al*, 2016), which is consistent with the results of clinical trials of Plk1 inhibitors for solid tumors, in which response rates were low (4–14%) in unselected patients with stable disease rates of 26–42% (Schoffski *et al*, 2012, 2010; Sebastian *et al*, 2010; Stadler *et al*, 2014). Although approximately 20% of NSCLC tumors are mesenchymal (Akbani *et al*, 2014; Chen *et al*, 2014) and predicted to be sensitive to Plk1 inhibition, the reversibility of EMT and intratumoral heterogeneity may diminish the efficacy of Plk1 inhibitors, contributing to low response rates. Recently, Lee *et al* (2018) measured the same 76-gene EMT score that we had used to classify NSCLC cell lines (Byers *et al*, 2013) in 35 regions from 10 NSCLC tumors. Considerable differences in the EMT scores were observed between regions in two of the 10 tumors; in the other eight tumors, different regions within each tumor had very similar EMT scores. The finding that the combination of Plk1 and cMet inhibition led to striking tumor regression *in vivo* in both epithelial and mesenchymal NSCLC suggests that this combination would be broadly effective in NSCLC patients who may have tumors with heterogeneity or dynamic changes in EMT status. In addition, it is rational to target a pathway that may mediate acquired resistance upfront to achieve a more durable response to therapy (Neel & Bivona, 2017). Because both cMet and Plk1 inhibitors are in clinical development, our work could be rapidly translated to clinical testing.

Recently published work using a novel drug (Poloppin) that inhibits phosphopeptide binding by the Plk1 polo-binding domain supports our findings (Narvaez *et al*, 2017). Poloppin led to cell death in *KRAS* mutant cancer cells *in vitro* and decreased tumor size *in vivo*. Because cMet was upregulated in a colon cancer cell line (SW48) expressing $KRAS^{G12D}$, Narvaez, *et al* investigated the combination of MET knockdown and cMet inhibition with Poloppin. Both cMet inhibition and knockdown did sensitize five *KRAS* mutant cell lines and one pancreatic organoid to Poloppin *in vitro*.

Dysregulation of cMet signaling–mediated proliferation, apoptosis, and migration through cMet overexpression, *MET* amplification, *MET* mutation, or HGF-induced activation has been widely demonstrated in oncogenic processes across multiple tumor types, including NSCLC (Smyth *et al*, 2014; Tsuta *et al*, 2012; Van Der Steen *et al*, 2015). cMet inhibitors have been extensively studied in NSCLC (Salgia, 2017). Recently, mutations in exon 14 of *MET* that lead to an in-frame deletion of the negative regulatory juxtamembrane domain were identified in 4% of lung adenocarcinomas. These mutations result in cMet activation and clinical sensitivity to cMet inhibition (Paik *et al*, 2015). cMet inhibitors are actively being studied in cancers bearing these mutations; a phase II clinical trial of tepotinib in NSCLC harboring *MET* exon 14 skipping alterations (NCT02864992) is underway. *MET* is also amplified in 5% of newly diagnosed lung adenocarcinomas (Cappuzzo *et al*, 2009; Kong-Beltran *et al*, 2006; Tsuta *et al*, 2012), and cMet inhibitors are effective in patients with gene copy numbers > 5 (Salgia, 2017). The presence of cMet/GRB2 complexes is associated with response to cMet inhibitors and may serve as an additional biomarker to select patients who are sensitive to cMet inhibitors in the future (Smith *et al*, 2017). In the current study, the expression of total cMet protein predicted resistance to four Plk1 inhibitors, although cMet protein and gene expression did not correlate with response in our prior study (Ferrarotto *et al*, 2016). Our data suggest that vimentin-dependent cMet activation is independent of canonical mechanisms of cMet activation because a HGF neutralizing antibody can still affect cMet activation in mesenchymal NSCLC and because robust cMet activation by an activating mutation or amplification was not affected by Plk1 inhibition.

Several reports established the cooperativity of cMet and the epidermal growth factor receptor (EGFR) in various cancers, including NSCLC. Co-targeting of these kinases potentially produces synergistic antitumor effects (Chae *et al*, 2016; Puri & Salgia, 2008; Wu *et al*, 2016a), although responses in clinical studies of the combination in NSCLC patients have been modest (Ma, 2015). Both cMet activation and EMT function as resistance mechanisms to EGFR tyrosine kinase inhibitors in NSCLC (Jakobsen *et al*, 2017; Ninomiya *et al*, 2018; Rotow & Bivona, 2017; Stewart *et al*, 2015; Yoshida *et al*, 2016). Clinical studies combining cMet and EGFR inhibitors in *MET*-amplified, *EGFR*-mutant NSCLC are ongoing (Rotow & Bivona, 2017). We previously tested the efficacy of Plk1 inhibition in NSCLC cell lines with acquired resistance to EGFR inhibitors and found that cell lines that had undergone EMT, but not those with *T790M* mutations, became more sensitive to Plk1 inhibition (Wang *et al*, 2016).

During the reversible process of EMT, epithelial cells lose cell–cell contacts, increase motility, and develop resistance to apoptosis

induced by chemotherapy, targeted therapy, and radiotherapy. Changes in gene expression during EMT reflect these characteristics and include repression of E-cadherin expression with the dissolution of cell–cell junctions; changes in genes encoding cytoskeletal proteins, including the activation of vimentin; and alterations in proteins that affect extracellular matrix interactions, including β1-integrin. Inhibition of EMT in genetically diverse NSCLC cell lines led to growth inhibition (Burns *et al*, 2013). Recent studies have demonstrated that Plk1 has a cell cycle–independent function in the regulation of EMT by activating CRAF/ERK signaling in prostate cancer (Wu *et al*, 2016b) or by activating AKT in gastric cancer (Cai *et al*, 2016). Plk1 may also indirectly contribute to EMT through regulation of its substrate, the transcription factor Forkhead box M1 (Kong *et al*, 2014; Wang *et al*, 2014). However, when we manipulated Plk1, NSCLC cells did not undergo morphologic changes consistent with EMT or show changes in expression of EMT-related proteins, suggesting that Plk1 is not a driver of EMT in NSCLC (Ferrarotto *et al*, 2016).

The link between EMT and Plk1 inhibition–induced apoptosis is not explained by canonical signaling pathways, but we hypothesized that proteins that were differentially expressed during EMT, such as vimentin, might be important in this process. CDK1 phosphorylates vimentin at S56, which provides a Plk1 binding site. Plk1 further phosphorylates vimentin at S82 (Oguri *et al*, 2006; Yamaguchi *et al*, 2005), which regulates vimentin filament segregation, coordinately with rho-kinase and Aurora-B (Yamaguchi *et al*, 2005). Recently, another study also demonstrated that Plk1 regulates smooth muscle contraction by modulating vimentin phosphorylation at S56 (Li *et al*, 2016). In addition, Plk1 regulates cell surface levels of β1-integrin and invasion by phosphorylating vimentin in breast cancer cells (Rizki *et al*, 2007).

Integrins and other cell surface receptors can lead to ligand-independent activation of cMet (Mitra *et al*, 2011; Varkaris *et al*, 2013). β1-Integrin positively regulates the endocytosis of activated cMet, as well as cMet signaling after endocytosis in some breast and lung cancer cell lines. cMet and β1-integrin form a complex on the plasma membrane. cMet activation in either a ligand-dependent or ligand-independent manner results in internalization and activation of β1-integrin. Additionally, β1-integrin in its active conformation positively regulates the endocytosis of activated cMet. Thus, both cMet and β1-integrin mutually interact with each other for optimal internalization in a clathrin-dependent manner. After internalization, the cMet/β1-integrin complex gradually accumulates on autophagy-related endomembranes, where β1-integrin promotes downstream cMet signaling via p52Shc adaptor protein that in turn activates the ERK1/2 signaling pathway. This β1-integrin–dependent cMet-sustained signaling regulates cell survival and growth, tumorigenesis, invasion, and lung colonization *in vivo* (Barrow-McGee *et al*, 2016).

Recently, Jahangiri *et al* demonstrated cMet displaces the α-heterodimer partner of β1-integrin, resulting in cMet/β1-integrin complex formation. This switching of the β1-integrin binding partner from α5-integrin to cMet significantly increases fibronectin affinity. Because β1-integrin lacks enzymatic activity, its signaling depends on the kinase adaptor protein ILK, which binds the cytoplasmic domain of β1-integrin. In the cMet/β1-integrin complex, fibronectin promotes ILK-mediated cMet phosphorylation even in the absence of HGF. Formation of this complex is regulated by tumor microenvironmental factors associated with metastasis and therapeutic resistance (Jahangiri *et al*, 2017). This activation could lead to Plk1 inhibitor resistance in mesenchymal NSCLC by bypassing Plk1 inhibition–mediated cMet inhibition. This residual cMet/β1-integrin complex activity, which is dependent upon ligands in the tumor microenvironment, may explain why the combination of PLK1 and cMet inhibition is more effective than single drugs in some mesenchymal NSCLC models and why we observed differences in single-agent PLK1 inhibitor efficacy *in vitro* compared with *in vivo*. Consistent with that study, we also observed that cMet and β1-integrin interact in NSCLC and that manipulation of β1-integrin affected cMet phosphorylation. Furthermore, we demonstrated that Plk1 regulates vimentin phosphorylation, which in turn regulates cMet phosphorylation. We are the first to connect these signaling pathways from Plk1 to cMet and the first to study this pathway in NSCLC. Future studies will include fibronectin affinity studies and subcellular localization studies of β1-integrin, cMet, vimentin, and Plk1 to assess the specific effects of these pathways on β1-integrin trafficking.

In conclusion, we demonstrated that Plk1 inhibition leads to apoptosis in mesenchymal NSCLC owing to direct effects on Plk1, as well as parallel vimentin and β1-integrin–mediated, ligand-independent inhibition of cMet. Moreover, the lack of cMet inhibition in epithelial NSCLC defines a previously unknown pathway of resistance to Plk1 inhibition. Although EMT proteins could serve as candidate biomarkers to select patients for Plk1 inhibition, intratumoral heterogeneity of EMT may limit this approach. The addition of cMet inhibitors is a promising therapeutic strategy to overcome *de novo* and acquired resistance to Plk1 inhibitors in patients with NSCLC.

Materials and Methods

Reagents and cell lines

All drugs were purchased from Selleck Chemicals (Houston, TX) and prepared as 10 mmol/l stock solutions in dimethyl sulfoxide. Predesigned sets of four independent siRNA sequences of the target genes *Plk1* and *MET* (siGENOME SMARTpool; Dharmacon, Lafayette, CO) were used. Human TGF-β1 was purchased from Cell Signaling Technology (Danvers, MA). Human fibronectin was purchased from Sigma-Aldrich (St. Louis, MO). Constitutive active TPR-Met plasmid and control pBABE plasmid were obtained from Addgene (Cambridge, MA). Antibodies and dilutions used in the study are listed in Appendix Table S3. The HGF neutralizing monoclonal antibody (24612.111) was acquired from Invitrogen (Catalog # MA1-24767, Thermo Fisher Scientific, Waltham, MA).

Human NSCLC cell lines were obtained, maintained, and genotyped by STR profiling as previously described (Ferrarotto *et al*, 2016; Peng *et al*, 2016) and routinely tested for the presence of mycoplasma species using the Mycoplasma Detection Kit (Lonza, Basel, Switzerland).

Development of VAR cell line

For generation of the VAR cell line, the Calu6 cell line was incubated with stepwise increasing concentrations of volasertib. The established Calu6 VAR cell line was maintained in 250 nM volasertib.

Transfections and transduction

Retroviruses were produced by co-transfecting HEK293 cells with 1 μg of the viral packaging vector pUMVC3 and envelope vector pCMV-VSV-G (8:1 ratio) and 1 μg of retroviral plasmid pBABE–TPR-Met or the control vector using Lipofectamine 3000. The HEK293 cell medium was changed 24 h after transfection, and the cells were incubated at 37°C for 48 h to allow for virus production. After 48 h, HEK293 medium containing viral particles was filtered and transferred onto NSCLC cell culture plates and incubated at 37°C for 48 h. After transduction, fresh RPMI 1640 medium with 10% fetal bovine serum was added to the cell culture plates, and the NSCLC cells were allowed to recover for 24 h. NSCLC cells were selected using 3 μg/ml puromycin.

For knockdown experiments, NSCLC cells were transfected with predesigned sets of four independent siRNAs against Plk1 and cMet using Lipofectamine RNAiMAX Transfection Reagent (Thermo Fisher Scientific, Waltham, MA), as we previously described (Zhang *et al*, 2017).

Cell viability assays

Cell viability assays were conducted with the CellTiter-Glo Luminescent Assay (Promega, Fitchburg, WI) after 72 h of exposure to serial fold drug dilutions, as described previously (Ferrarotto *et al*, 2016; Wang *et al*, 2016). Drug synergy between volasertib and tepotinib was determined by the combination index, which was generated according to the Chou–Talalay median effect method (Chou, 2010) using the CalcuSyn software (Biosoft, Cambridge, UK).

Colony formation assays

For clonogenic assays, cells were treated for 24 h with dimethyl sulfoxide, volasertib, tepotinib, or the combination of volasertib and tepotinib and then incubated in drug-free medium for 14–21 days. At the end of the assay, cells were washed, fixed, and stained with crystal violet as described previously (Kalu *et al*, 2018). The total number of colonies per well was estimated using the ImageJ software program (National Institutes of Health, Bethesda, MD). All clonogenic assays were performed in triplicate, and each test was completed twice on different days.

Reverse phase protein array

Reverse phase protein array was used to compare the expression of 301 proteins (Kalu *et al*, 2017) using techniques we recently described (Mazumdar *et al*, 2014), in three parental epithelial NSCLC cell lines, three TGF-β–induced isogenic mesenchymal NSCLC cell lines, and two mesenchymal NSCLC cell lines after incubation with 50 nM volasertib or vehicle for 24 h. The experiments were performed in triplicate on three different days.

Western blot analysis

Equal amounts of NSCLC cell lysates were separated using 4–20% SDS–PAGE, transferred, and immunoblotted with the indicated primary antibodies, and detected using a horseradish peroxidase–conjugated secondary antibody and an enhanced chemiluminescence reagent, as described previously (Wang *et al*, 2016). Densitometry quantification of the bands was performed with the ImageJ software program (National Institutes of Health).

Immunoprecipitation assay

Immunoprecipitation was done with Magnetic Dynabeads (Thermo Fisher Scientific, Waltham, MA) according to the manufacturer's protocol. Briefly, control and treated cell lysates were incubated with the indicated antibody–Dynabeads conjugate followed by purification of antigen–antibody–Dynabeads conjugate and separation on SDS–PAGE for immunoblotting.

Apoptosis analyses

Apoptosis was measured by TUNEL (terminal deoxynucleotidyl transferase dUTP nick end labeling) staining (Apo-BrdU Kit; BD Biosciences, San Jose, CA) as described previously (Kalu *et al*, 2017; Wang *et al*, 2016). Data were acquired using a flow cytometer (Gallios; Beckman Coulter, Brea, CA) and analyzed using Kaluza software (Beckman Coulter, Brea, CA).

Comet assay

The comet assay was done to detect DNA fragmentation, according to the manufacturer's instructions (Trevigen, Gaithersburg, MD) and as we previously described (Peng *et al*, 2016; Sen *et al*, 2012). After fixation, lysis and electrophoresis slides were stained with Vista Green for fluorescence imaging. For evaluation of the comet patterns, about 100 nuclei from each slide were analyzed by Comet Score Pro (TriTek Corp., Sumerduck, VA), and tail moment was calculated by multiplying tail DNA percentage by the length of the tail (Wang *et al*, 2016).

Quantitative PCR

Total cellular RNA was isolated using the RNeasy Mini Kit (Qiagen, Hilden, Germany), and complementary DNAs (cDNAs) were synthesized using iScript Reverse Transcription Supermix (Bio-Rad Laboratories, Hercules, CA). Quantitative real-time PCR assays were done with iTaq Universal SYBR Green Supermix (Bio-Rad Laboratories) and the CFX96 Real-time System (Bio-Rad Laboratories) as described previously (Kalu *et al*, 2017). Primers are listed in Appendix Table S4.

HGF estimation

Secretory HGF was estimated using the HGF ELISA Kit (Abcam, Cambridge, MA) according to the manufacturer's protocol. Briefly, NSCLC cell lines were treated with 50 nM volasertib in serum-free medium for 24 h, and HGF levels were measured in conditioned medium.

Subcutaneous xenograft animal models

In conducting research using animals, the investigators adhered to the laws of the United States and regulations of the US Department of Agriculture. All animal experiments were reviewed and approved

The paper explained

Problem
Most NSCLC remains incurable despite survival benefits from targeted and immunotherapy. Thus, there is still an urgent need for effective systemic therapy. While Plk1 inhibitors are well tolerated by patients and some striking clinical responses were observed, response rates were generally low. Likewise, Plk1 inhibitors lead to diverse biological effects in cancer cells. Understanding the basis for Plk1 inhibitor–induced apoptosis is essential to maximizing their antitumor efficacy. To address this need, our laboratory previously discovered that mesenchymal NSCLC cell lines are more sensitive to Plk1 inhibitors than epithelial cell lines *in vitro* and *in vivo*. However, mechanisms of resistance to Plk1 inhibitors have not been elucidated and this unknown is a major gap in knowledge.

Results
We used isogenic pairs of epithelial and mesenchymal NSCLC cell lines to measure changes in the expression of 301 proteins after Plk1 inhibition. We observed differential regulation of the cMet/FAK/Src axis, which is intact in both mesenchymal and epithelial cells. However, Plk1 inhibition inhibits cMet phosphorylation only in mesenchymal NSCLC cells, leading to subsequent inhibition of FAK and Src. Constitutively active cMet abrogates Plk1 inhibitor–induced apoptosis. Likewise, cMet silencing or inhibition enhances Plk1 inhibitor–induced apoptosis. Additionally, cells with acquired resistance to Plk1 inhibitors are more epithelial than their parental cells and maintain cMet activation after Plk1 inhibition. In both patient-derived and cell line xenografts, mesenchymal NSCLC was more sensitive to Plk1 inhibition alone than was epithelial NSCLC. The combination of cMet and Plk1 inhibition led to regression of tumors in three models and marked tumor size reduction in the fourth model. When drug treatment was stopped, tumors treated with the combination did not regrow. Plk1 regulates cMet via the vimentin protein that is only expressed in mesenchymal NSCLC.

Impact
NSCLC cell lines have diverse sensitivities to Plk1 inhibition, which is consistent with the results of clinical trials of Plk1 inhibitors in solid tumors. This study reveals a novel mechanism of non-canonical cMet activation in resistant/epithelial NSCLC after Plk1 inhibition. The addition of cMet inhibitors is a promising therapeutic strategy to overcome *de novo* and acquired resistance to Plk1 inhibitors in patients with NSCLC.

by the Institutional Animal Care and Use Committee (IACUC) at The University of Texas MD Anderson Cancer Center and conducted in accordance with MD Anderson's Office of Research Administration and IACUC guidelines. Two million NSCLC cells per mouse were injected subcutaneously, or logarithmically growing PDXs (Hao *et al*, 2015) were implanted subcutaneously into the flanks of 6- to 8-week-old female nude mice (Harlan Laboratories, Indianapolis, IN). Tumors were measured by caliper twice weekly by two, non-blinded, independent investigators. Tumor volumes were calculated as follows: $(\text{length} \times \text{width}^2)/2$. When tumor volumes reached 150 mm^3, the mice were randomized and treated with 30 mg/kg volasertib intravenously weekly, 25 mg/kg tepotinib daily (5 days on and 2 days off) by oral gavage, both agents, or vehicle control for 5 weeks. Mice were then euthanized and tumors excised.

A linear model was fit to the data using generalized least squares with two variables (treatment and day) and an autocorrelation structure of order 1 in residuals, given that we had a single grouping variable of mouse identification. The Tukey test was used for pairwise comparisons between treatment groups, and therefore, *P*-values corrected for multiple comparisons were produced, as described previously (Zhang *et al*, 2017). Log-rank tests were conducted to assess the association of the treatment type with survival. Benjamini–Hochberg correction was applied to *P*-values from pairwise comparisons between treatment groups to adjust for multiple comparisons. In addition, Kaplan–Meier curves were generated.

TUNEL tissue staining

Harvested tumor tissues were fixed in 10% formalin, embedded in paraffin, and sectioned at 5 μM. Briefly, after deparaffinization and rehydration, tissue sections were subsequently processed for DNA labeling by TdT dNTP followed by Strep-HRP/DAB detection using the TUNEL Apoptosis Detection Kit (Trevigen, Gaithersburg, MD). Images were taken at 40× magnification, and image analysis was performed to calculate the percentage of TUNEL-positive cells using ImageJ software (National Institutes of Health).

Statistical analysis

All statistical analyses were performed using R packages (https://www.r-project.org/), a publically available and widely used statistical computing tool. RPPA protein expression and Plk1 inhibitor (BI2536, GSK461364, BRD-K70511574, and GW-843682X) sensitivity data were downloaded from the MD Anderson Cell Line Project (http://tcpaportal.org/mclp/#/) and CTRPv2 (Broad Institute; https://portals.broadinstitute.org/ctrp/) databases and curated for NSCLC cell lines on March 5, 2017. RPPA data for 71 cell lines were available for BI2536, 69 cell lines for GSK461364, 68 cell lines for BRD-K70511574, and 64 cell lines for GW-843682X. To identify correlation between drug sensitivity and protein expression, we applied Spearman's correlation using R. For RPPA proteins to be compared between cell lines after treatment with a Plk1 inhibitor, it is necessary to treat cell line as a random effect because the cell line variation is dominant in principal component analysis. Further contrasts were conducted to compare changes in epithelial cells after treatment with the Plk1 inhibitor, changes in mesenchymal cells after treatment with the Plk1 inhibitor, and changes between the two, which is the interaction term. The analysis was carried out by the limma package in R. To correct for multiple hypotheses testing, we adjusted the resulting *P*-values using the Benjamini–Hochberg method.

There are a variety of group comparisons with respect to different study designs, including two-factor and three-factor factorial designs. All *in vitro* experiments were repeated at least twice (biological replicates) with three or more technical replicates. Analysis of variance was applied, and various contrasts were set up to test the significance of difference between groups of interest and of the interaction of two factors. Bonferroni or Benjamini–Hochberg correction was applied to adjust for multiple testing. For tumor growth curve analysis, linear modeling using generalized least squares with two variables (treatment and day) and an autocorrelation structure of order 1 in residuals were applied. The Tukey test was used for pairwise comparisons among treatment groups, and *P*-values corrected for multiple comparisons were produced. For

survival analysis, log-rank tests were conducted to assess the association of the treatment type with survival. Benjamini–Hochberg correction was applied to *P*-values from pairwise comparisons between treatment groups to adjust for multiple comparisons. In addition, Kaplan–Meier curves were generated. A summary of statistical methods for each specific Figure is provided in Appendix Table S5.

Expanded View for this article is available online.

Acknowledgements
We thank Erica Goodoff of the Department of Scientific Publications at MD Anderson for editing this manuscript. Flow cytometry, bioinformatics, and animal facilities are supported by the National Cancer Institute Cancer Center Support Grant P30CA016672. PDX generation and annotation were supported by philanthropic contributions to The University of Texas MD Anderson Cancer Center Lung Moon Shot Program, Specialized Program of Research Excellence (SPORE) grant CA070907, and University of Texas PDX Development and Trial Center grant U54CA224065. The research was supported by generous donations and by the Office of the Assistant Secretary of Defense for Health Affairs through the Lung Cancer Research Program, under Award No. W81XWH-17-1-0206 (F.M.J.). Opinions, interpretations, conclusions, and recommendations are those of the authors and are not necessarily endorsed by the Department of Defense.

Author contributions
RS designed and performed most of the experiments and wrote the first draft of the manuscript. SP, PV, and VS assisted with experimental design and conduct of the animal experiments. BF provided and characterized several PDX models. LS, XR, and JW performed the bioinformatics and statistical analyses. FMJ oversaw the study design and wrote the final draft of the paper.

Conflict of interest
Faye M. Johnson has received research funding from PIQUR Therapeutics and Trovagene. Other authors have no conflicts of interest to declare.

For more information
https://www.mdanderson.org/research/departments-labs-institutes/labs/faye-johnson-laboratory.html
https://portals.broadinstitute.org/ccle
https://tcpaportal.org/mclp/#/
https://portals.broadinstitute.org/ctrp/

References

Akbani R, Ng PK, Werner HM, Shahmoradgoli M, Zhang F, Ju Z, Liu W, Yang JY, Yoshihara K, Li J, *et al* (2014) A pan-cancer proteomic perspective on The Cancer Genome Atlas. *Nat Commun* 5: 3887

Barrow-McGee R, Kishi N, Joffre C, Menard L, Hervieu A, Bakhouche BA, Noval AJ, Mai A, Guzman C, Robbez-Masson L, *et al* (2016) Beta 1-integrin-c-Met cooperation reveals an inside-in survival signalling on autophagy-related endomembranes. *Nat Commun* 7: 11942

Bladt F, Faden B, Friese-Hamim M, Knuehl C, Wilm C, Fittschen C, Gradler U, Meyring M, Dorsch D, Jaehrling F, *et al* (2013) EMD 1214063 and EMD 1204831 constitute a new class of potent and highly selective c-Met inhibitors. *Clin Cancer Res* 19: 2941 – 2951

Burns TF, Dobromilskaya I, Murphy SC, Gajula RP, Thiyagarajan S, Chatley SN, Aziz K, Cho YJ, Tran PT, Rudin CM (2013) Inhibition of TWIST1 leads to activation of oncogene-induced senescence in oncogene-driven non-small cell lung cancer. *Mol Cancer Res* 11: 329 – 338

Byers LA, Diao L, Wang J, Saintigny P, Girard L, Peyton M, Shen L, Fan Y, Giri U, Tumula PK, *et al* (2013) An epithelial-mesenchymal transition gene signature predicts resistance to EGFR and PI3K inhibitors and identifies Axl as a therapeutic target for overcoming EGFR inhibitor resistance. *Clin Cancer Res* 19: 279 – 290

Cai XP, Chen LD, Song HB, Zhang CX, Yuan ZW, Xiang ZX (2016) PLK1 promotes epithelial-mesenchymal transition and metastasis of gastric carcinoma cells. *Am J Transl Res* 8: 4172 – 4183

Cappuzzo F, Marchetti A, Skokan M, Rossi E, Gajapathy S, Felicioni L, Del Grammastro M, Sciarrotta MG, Buttitta F, Incarbone M, *et al* (2009) Increased MET gene copy number negatively affects survival of surgically resected non-small-cell lung cancer patients. *J Clin Oncol* 27: 1667 – 1674

Chae YK, Gagliato Dde M, Pai SG, Carneiro B, Mohindra N, Giles FJ, Ramakrishnan-Geethakumari P, Sohn J, Liu S, Chen H, *et al* (2016) The association between EGFR and cMET expression and phosphorylation and its prognostic implication in patients with breast cancer. *PLoS One* 11: e0152585

Chen L, Gibbons DL, Goswami S, Cortez MA, Ahn YH, Byers LA, Zhang X, Yi X, Dwyer D, Lin W, *et al* (2014) Metastasis is regulated via microRNA-200/ZEB1 axis control of tumour cell PD-L1 expression and intratumoral immunosuppression. *Nat Commun* 5: 5241

Choi M, Kim W, Cheon MG, Lee CW, Kim JE (2015) Polo-like kinase 1 inhibitor BI2536 causes mitotic catastrophe following activation of the spindle assembly checkpoint in non-small cell lung cancer cells. *Cancer Lett* 357: 591 – 601

Chou TC (2010) Drug combination studies and their synergy quantification using the Chou-Talalay method. *Cancer Res* 70: 440 – 446

Craig SN, Wyatt MD, McInnes C (2014) Current assessment of polo-like kinases as anti-tumor drug targets. *Expert Opin Drug Discov* 9: 773 – 789

Degenhardt Y, Greshock J, Laquerre S, Gilmartin AG, Jing J, Richter M, Zhang X, Bleam M, Halsey W, Hughes A, *et al* (2010) Sensitivity of cancer cells to Plk1 inhibitor GSK461364A is associated with loss of p53 function and chromosome instability. *Mol Cancer Ther* 9: 2079 – 2089

Driscoll DL, Chakravarty A, Bowman D, Shinde V, Lasky K, Shi J, Vos T, Stringer B, Amidon B, D'Amore N, *et al* (2014) Plk1 inhibition causes post-mitotic DNA damage and senescence in a range of human tumor cell lines. *PLoS One* 9: e111060

Ferrarotto R, Goonatilake R, Yoo SY, Tong P, Giri U, Peng S, Minna J, Girard L, Wang Y, Wang L, *et al* (2016) Epithelial-mesenchymal transition predicts polo-like kinase 1 inhibitor-mediated apoptosis in non-small cell lung cancer. *Clin Cancer Res* 22: 1674 – 1686

Friese-Hamim M, Bladt F, Locatelli G, Stammberger U, Blaukat A (2017) The selective c-Met inhibitor tepotinib can overcome epidermal growth factor receptor inhibitor resistance mediated by aberrant c-Met activation in NSCLC models. *Am J Cancer Res* 7: 962 – 972

Gjertsen BT, Schoffski P (2015) Discovery and development of the Polo-like kinase inhibitor volasertib in cancer therapy. *Leukemia* 29: 11 – 19

Hao C, Wang L, Peng S, Cao M, Li H, Hu J, Huang X, Liu W, Zhang H, Wu S, *et al* (2015) Gene mutations in primary tumors and corresponding patient-derived xenografts derived from non-small cell lung cancer. *Cancer Lett* 357: 179 – 185

Jahangiri A, Nguyen A, Chandra A, Sidorov MK, Yagnik G, Rick J, Han SW, Chen W, Flanigan PM, Schneidman-Duhovny D, *et al* (2017) Cross-activating c-Met/beta1 integrin complex drives metastasis and invasive resistance in cancer. *Proc Natl Acad Sci USA* 114: E8685 – E8694

Jakobsen KR, Demuth C, Madsen AT, Hussmann D, Vad-Nielsen J, Nielsen AL, Sorensen BS (2017) MET amplification and epithelial-to-mesenchymal transition exist as parallel resistance mechanisms in erlotinib-resistant, EGFR-mutated, NSCLC HCC827 cells. *Oncogenesis* 6: e307

Kalu NN, Mazumdar T, Peng S, Shen L, Sambandam V, Rao X, Xi Y, Li L, Qi Y, Gleber-Netto FO, *et al* (2017) Genomic characterization of human papillomavirus-positive and -negative human squamous cell cancer cell lines. *Oncotarget* 8: 86369 – 86383

Kalu NN, Mazumdar T, Peng S, Tong P, Shen L, Wang J, Banerjee U, Myers JN, Pickering CR, Brunell D, *et al* (2018) Comprehensive pharmacogenomic profiling of human papillomavirus-positive and -negative squamous cell carcinoma identifies sensitivity to aurora kinase inhibition in KMT2D mutants. *Cancer Lett* 431: 64 – 72

Kong FF, Qu ZQ, Yuan HH, Wang JY, Zhao M, Guo YH, Shi J, Gong XD, Zhu YL, Liu F, *et al* (2014) Overexpression of FOXM1 is associated with EMT and is a predictor of poor prognosis in non-small cell lung cancer. *Oncol Rep* 31: 2660 – 2668

Kong-Beltran M, Seshagiri S, Zha J, Zhu W, Bhawe K, Mendoza N, Holcomb T, Pujara K, Stinson J, Fu L, *et al* (2006) Somatic mutations lead to an oncogenic deletion of met in lung cancer. *Cancer Res* 66: 283 – 289

Kubo T, Yamamoto H, Lockwood WW, Valencia I, Soh J, Peyton M, Jida M, Otani H, Fujii T, Ouchida M, *et al* (2009) MET gene amplification or EGFR mutation activate MET in lung cancers untreated with EGFR tyrosine kinase inhibitors. *Int J Cancer* 124: 1778 – 1784

Lee WC, Diao L, Wang J, Zhang J, Roarty EB, Varghese S, Chow CW, Fujimoto J, Behrens C, Cascone T, *et al* (2018) Multiregion gene expression profiling reveals heterogeneity in molecular subtypes and immunotherapy response signatures in lung cancer. *Mod Pathol* 31: 947 – 955

Li J, Wang R, Gannon OJ, Rezey AC, Jiang S, Gerlach BD, Liao G, Tang DD (2016) Polo-like kinase 1 regulates vimentin phosphorylation at ser-56 and contraction in smooth muscle. *J Biol Chem* 291: 23693 – 23703

Li J, Zhao W, Akbani R, Liu W, Ju Z, Ling S, Vellano CP, Roebuck P, Yu Q, Eterovic AK, *et al* (2017) Characterization of human cancer cell lines by reverse-phase protein arrays. *Cancer Cell* 31: 225 – 239

Luo J, Emanuele MJ, Li D, Creighton CJ, Schlabach MR, Westbrook TF, Wong KK, Elledge SJ (2009) A genome-wide RNAi screen identifies multiple synthetic lethal interactions with the Ras oncogene. *Cell* 137: 835 – 848

Ma PC (2015) MET receptor juxtamembrane exon 14 alternative spliced variant: novel cancer genomic predictive biomarker. *Cancer Discov* 5: 802 – 805

Mazumdar T, Byers LA, Ng PK, Mills GB, Peng S, Diao L, Fan YH, Stemke-Hale K, Heymach JV, Myers JN, *et al* (2014) A comprehensive evaluation of biomarkers predictive of response to PI3K inhibitors and of resistance mechanisms in head and neck squamous cell carcinoma. *Mol Cancer Ther* 13: 2738 – 2750

McCarroll JA, Dwarte T, Baigude H, Dang J, Yang L, Erlich RB, Kimpton K, Teo J, Sagnella SM, Akerfeldt MC, *et al* (2015) Therapeutic targeting of polo-like kinase 1 using RNA-interfering nanoparticles (iNOPs) for the treatment of non-small cell lung cancer. *Oncotarget* 6: 12020 – 12034

Medema RH, Lin CC, Yang JC (2011) Polo-like kinase 1 inhibitors and their potential role in anticancer therapy, with a focus on NSCLC. *Clin Cancer Res* 17: 6459 – 6466

Mitra AK, Sawada K, Tiwari P, Mui K, Gwin K, Lengyel E (2011) Ligand-independent activation of c-Met by fibronectin and alpha(5)beta(1)-integrin regulates ovarian cancer invasion and metastasis. *Oncogene* 30: 1566 – 1576

Narvaez AJ, Ber S, Crooks A, Emery A, Hardwick B, Guarino Almeida E, Huggins DJ, Perera D, Roberts-Thomson M, Azzarelli R, *et al* (2017) Modulating protein-protein interactions of the mitotic polo-like kinases to target mutant KRAS. *Cell Chem Biol* 24: 1017 – 1028 e1017

Neel DS, Bivona TG (2017) Resistance is futile: overcoming resistance to targeted therapies in lung adenocarcinoma. *NPJ Precis Oncol* 1: 3

Ninomiya K, Ohashi K, Makimoto G, Tomida S, Higo H, Kayatani H, Ninomiya T, Kubo T, Ichihara E, Hotta K, *et al* (2018) MET or NRAS amplification is an acquired resistance mechanism to the third-generation EGFR inhibitor naquotinib. *Sci Rep* 8: 1955

Nokihara H, Yamada Y, Fujiwara Y, Yamamoto N, Wakui H, Nakamichi S, Kitazono S, Inoue K, Harada A, Taube T, *et al* (2016) Phase I trial of volasertib, a Polo-like kinase inhibitor, in Japanese patients with advanced solid tumors. *Invest New Drugs* 34: 66 – 74

Oguri T, Inoko A, Shima H, Izawa I, Arimura N, Yamaguchi T, Inagaki N, Kaibuchi K, Kikuchi K, Inagaki M (2006) Vimentin-Ser82 as a memory phosphorylation site in astrocytes. *Genes Cells* 11: 531 – 540

Paik PK, Drilon A, Fan PD, Yu H, Rekhtman N, Ginsberg MS, Borsu L, Schultz N, Berger MF, Rudin CM, *et al* (2015) Response to MET inhibitors in patients with stage IV lung adenocarcinomas harboring MET mutations causing exon 14 skipping. *Cancer Discov* 5: 842 – 849

Peng S, Sen B, Mazumdar T, Byers LA, Diao L, Wang J, Tong P, Giri U, Heymach JV, Kadara HN, *et al* (2016) Dasatinib induces DNA damage and activates DNA repair pathways leading to senescence in non-small cell lung cancer cell lines with kinase-inactivating BRAF mutations. *Oncotarget* 7: 565 – 579

Pujade-Lauraine E, Selle F, Weber B, Ray-Coquard IL, Vergote I, Sufliarsky J, Del Campo JM, Lortholary A, Lesoin A, Follana P, *et al* (2016) Volasertib versus chemotherapy in platinum-resistant or -refractory ovarian cancer: a randomized phase II groupe des investigateurs nationaux pour l'etude des cancers de l'ovaire study. *J Clin Oncol* 34: 706 – 713

Puri N, Salgia R (2008) Synergism of EGFR and c-Met pathways, cross-talk and inhibition, in non-small cell lung cancer. *J Carcinog* 7: 9

Reungwetwattana T, Liang Y, Zhu V, Ou SI (2017) The race to target MET exon 14 skipping alterations in non-small cell lung cancer: the why, the how, the who, the unknown, and the inevitable. *Lung Cancer* 103: 27 – 37

Rizki A, Mott JD, Bissell MJ (2007) Polo-like kinase 1 is involved in invasion through extracellular matrix. *Cancer Res* 67: 11106 – 11110

Rotow J, Bivona TG (2017) Understanding and targeting resistance mechanisms in NSCLC. *Nat Rev Cancer* 17: 637 – 658

Rudolph D, Steegmaier M, Hoffmann M, Grauert M, Baum A, Quant J, Haslinger C, Garin-Chesa P, Adolf GR (2009) BI 6727, a Polo-like kinase inhibitor with improved pharmacokinetic profile and broad antitumor activity. *Clin Cancer Res* 15: 3094 – 3102

Salgia R (2017) MET in lung cancer: biomarker selection based on scientific rationale. *Mol Cancer Ther* 16: 555 – 565

Sanhaji M, Kreis NN, Zimmer B, Berg T, Louwen F, Yuan J (2012) p53 is not directly relevant to the response of Polo-like kinase 1 inhibitors. *Cell Cycle* 11: 543 – 553

Sanhaji M, Louwen F, Zimmer B, Kreis NN, Roth S, Yuan J (2013) Polo-like kinase 1 inhibitors, mitotic stress and the tumor suppressor p53. *Cell Cycle* 12: 1340 – 1351

Schoffski P, Blay JY, De Greve J, Brain E, Machiels JP, Soria JC, Sleijfer S, Wolter P, Ray-Coquard I, Fontaine C, *et al* (2010) Multicentric parallel phase II trial of the polo-like kinase 1 inhibitor BI 2536 in patients with advanced head and neck cancer, breast cancer, ovarian cancer, soft tissue sarcoma and melanoma. The first protocol of the European Organization for Research and Treatment of Cancer (EORTC) Network Of Core Institutes (NOCI). *Eur J Cancer* 46: 2206 – 2215

Schoffski P, Awada A, Dumez H, Gil T, Bartholomeus S, Wolter P, Taton M, Fritsch H, Glomb P, Munzert G (2012) A phase I, dose-escalation study of the novel Polo-like kinase inhibitor volasertib (BI 6727) in patients with advanced solid tumours. *Eur J Cancer* 48: 179 – 186

Seashore-Ludlow B, Rees MG, Cheah JH, Cokol M, Price EV, Coletti ME, Jones V, Bodycombe NE, Soule CK, Gould J, *et al* (2015) Harnessing connectivity in a large-scale small-molecule sensitivity dataset. *Cancer Discov* 5: 1210 – 1223

Sebastian M, Reck M, Waller CF, Kortsik C, Frickhofen N, Schuler M, Fritsch H, Gaschler-Markefski B, Hanft G, Munzert G, *et al* (2010) The efficacy and safety of BI 2536, a novel Plk-1 inhibitor, in patients with stage IIIB/IV non-small cell lung cancer who had relapsed after, or failed, chemotherapy: results from an open-label, randomized phase II clinical trial. *J Thorac Oncol* 5: 1060 – 1067

Sen B, Peng S, Saigal B, Williams MD, Johnson FM (2011) Distinct interactions between c-Src and c-Met in mediating resistance to c-Src inhibition in head and neck cancer. *Clin Cancer Res* 17: 514 – 524

Sen B, Peng S, Tang X, Erickson HS, Galindo H, Mazumdar T, Stewart DJ, Wistuba I, Johnson FM (2012) Kinase-impaired BRAF mutations in lung cancer confer sensitivity to dasatinib. *Sci Transl Med* 4: 136ra170

Siegel RL, Miller KD, Jemal A (2018) Cancer statistics, 2018. *CA Cancer J Clin* 68: 7 – 30

Smith MA, Licata T, Lakhani A, Garcia MV, Schildhaus HU, Vuaroqueaux V, Halmos B, Borczuk AC, Chen YA, Creelan BC, *et al* (2017) MET-GRB2 signaling-associated complexes correlate with oncogenic MET signaling and sensitivity to MET kinase inhibitors. *Clin Cancer Res* 23: 7084 – 7096

Smyth EC, Sclafani F, Cunningham D (2014) Emerging molecular targets in oncology: clinical potential of MET/hepatocyte growth-factor inhibitors. *Onco Targets Ther* 7: 1001 – 1014

Spankuch-Schmitt B, Bereiter-Hahn J, Kaufmann M, Strebhardt K (2002) Effect of RNA silencing of polo-like kinase-1 (PLK1) on apoptosis and spindle formation in human cancer cells. *J Natl Cancer Inst* 94: 1863 – 1877

Stadler WM, Vaughn DJ, Sonpavde G, Vogelzang NJ, Tagawa ST, Petrylak DP, Rosen P, Lin CC, Mahoney J, Modi S, *et al* (2014) An open-label, single-arm, phase 2 trial of the polo-like kinase inhibitor volasertib (BI 6727) in patients with locally advanced or metastatic urothelial cancer. *Cancer* 120: 976 – 982

Stewart EL, Tan SZ, Liu G, Tsao MS (2015) Known and putative mechanisms of resistance to EGFR targeted therapies in NSCLC patients with EGFR mutations-a review. *Transl Lung Cancer Res* 4: 67 – 81

Tsuta K, Kozu Y, Mimae T, Yoshida A, Kohno T, Sekine I, Tamura T, Asamura H, Furuta K, Tsuda H (2012) c-MET/phospho-MET protein expression and MET gene copy number in non-small cell lung carcinomas. *J Thorac Oncol* 7: 331 – 339

Van den Bossche J, Lardon F, Deschoolmeester V, De Pauw I, Vermorken JB, Specenier P, Pauwels P, Peeters M, Wouters A (2016) Spotlight on volasertib: preclinical and clinical evaluation of a promising Plk1 inhibitor. *Med Res Rev* 36: 749 – 786

Van Der Steen N, Pauwels P, Gil-Bazo I, Castanon E, Raez L, Cappuzzo F, Rolfo C (2015) cMET in NSCLC: can we cut off the head of the hydra? From the pathway to the resistance. *Cancers* 7: 556 – 573

Varkaris A, Gaur S, Parikh NU, Song JH, Dayyani F, Jin JK, Logothetis CJ, Gallick GE (2013) Ligand-independent activation of MET through IGF-1/IGF-1R signaling. *Int J Cancer* 133: 1536 – 1546

Wang Y, Yao B, Wang Y, Zhang M, Fu S, Gao H, Peng R, Zhang L, Tang J (2014) Increased FoxM1 expression is a target for metformin in the suppression of EMT in prostate cancer. *Int J Mol Med* 33: 1514 – 1522

Wang Y, Singh R, Wang L, Nilsson M, Goonatilake R, Tong P, Li L, Giri U, Villalobos P, Mino B, *et al* (2016) Polo-like kinase 1 inhibition diminishes acquired resistance to epidermal growth factor receptor inhibition in non-small cell lung cancer with T790M mutations. *Oncotarget* 7: 47998 – 48010

Wang Y, Wu L, Yao Y, Lu G, Xu L, Zhou J (2018) Polo-like kinase 1 inhibitor BI 6727 induces DNA damage and exerts strong antitumor activity in small cell lung cancer. *Cancer Lett* 436: 1 – 9

Wu DW, Chen TC, Huang HS, Lee H (2016a) TC-N19, a novel dual inhibitor of EGFR and cMET, efficiently overcomes EGFR-TKI resistance in non-small-cell lung cancer cells. *Cell Death Dis* 7: e2290

Wu J, Ivanov AI, Fisher PB, Fu Z (2016b) Polo-like kinase 1 induces epithelial-to-mesenchymal transition and promotes epithelial cell motility by activating CRAF/ERK signaling. *Elife* 5: e10734

Yamaguchi T, Goto H, Yokoyama T, Sillje H, Hanisch A, Uldschmid A, Takai Y, Oguri T, Nigg EA, Inagaki M (2005) Phosphorylation by Cdk1 induces Plk1-mediated vimentin phosphorylation during mitosis. *J Cell Biol* 171: 431 – 436

Yim H, Erikson RL (2009) Polo-like kinase 1 depletion induces DNA damage in early S prior to caspase activation. *Mol Cell Biol* 29: 2609 – 2621

Yoshida T, Song L, Bai Y, Kinose F, Li J, Ohaegbulam KC, Munoz-Antonia T, Qu X, Eschrich S, Uramoto H, *et al* (2016) ZEB1 mediates acquired resistance to the epidermal growth factor receptor-tyrosine kinase inhibitors in non-small cell lung cancer. *PLoS One* 11: e0147344

Zhang M, Singh R, Peng S, Mazumdar T, Sambandam V, Shen L, Tong P, Li L, Kalu NN, Pickering CR, *et al* (2017) Mutations of the LIM protein AJUBA mediate sensitivity of head and neck squamous cell carcinoma to treatment with cell-cycle inhibitors. *Cancer Lett* 392: 71 – 82

NEOPLASIA
www.neoplasia.com

Volume 20 Number 10 October 2018 pp. 975–984 975

A Novel Method for Quantifying Total Thoracic Tumor Burden in Mice[1]

Pavitra Viswanath[*†], Shaohua Peng[*], Ratnakar Singh[*2], Charles Kingsley[‡], Peter A. Balter[§] and Faye M. Johnson[*†]

[*]Department of Thoracic Head & Neck Medical Oncology, The University of Texas MD Anderson Cancer Center, Houston, TX; [†]The University of Texas Graduate School of Biomedical Sciences, Houston, TX; [‡]Department of Imaging Physics, The University of Texas MD Anderson Cancer Center, Houston, TX; [§]Department of Radiation Physics, The University of Texas MD Anderson Cancer Center, Houston, TX

Abstract

Mouse models are powerful tools to study lung cancer initiation and progression *in vivo* and have contributed significantly to recent advances in therapy. Using micro-computed tomography to monitor and study parenchymal and extra-parenchymal metastases in existing murine models of lung cancer is challenging owing to a lack of radiographic contrast and difficulty in achieving respiratory gating. To facilitate the analysis of these *in vivo* imaging studies and study of tumor progression in murine models we developed a novel, rapid, semi-automated method of calculating thoracic tumor burden from computed tomography images. This method, in which commercially available software is used to calculate the mass of the thoracic cavity (MTC), takes into account the aggregate tumor burden in the thoracic cavity. The present study showed that in tumor-free mice, the MTC does not change over time and is not affected by breathing, whereas in tumor-bearing mice, the increase in the MTC is a measure of tumor mass that correlates well with tumor burden measured by lung weight. Tumor burden calculated with our MTC method correlated with that measured by lung weight as well as or better than that calculated using four established methods. To test this method, we assessed metastatic tumor development and response to a pharmacologic PLK1 inhibitor in an orthotopic xenograft mouse model. PLK1 inhibition significantly inhibited tumor growth. Our results demonstrate that the MTC method can be used to study dynamic changes in tumor growth and response to therapeutics in genetically engineered mouse models and orthotopic xenograft mouse models of lung cancer.

Neoplasia (2018) 20, 975–984

Abbreviations: DICOM, Digital Imaging and Communications in Medicine; GEMM, genetically engineered mouse model; KP, KRAS TP53; micro-CT, micro–computed tomography; MTC, mass of the thoracic cavity; PLK1, polo-like kinase 1; RECIST, Response Evaluation Criteria in Solid Tumors; ROI, region of interest; SCP, sum of cross-product; T&V, tumor and vessel volume.

Address all correspondence to: Faye M. Johnson, Department of Thoracic Head & Neck Medical Oncology, Unit 432, The University of Texas MD Anderson Cancer Center, 1515 Holcombe Blvd, Houston, TX 77030, USA.
E-mail:; fmjohns@mdanderson.org

[1] Funding: MD Anderson's animal facilities are supported by the National Institutes of Health through MD Anderson's Cancer Center Support Grant (P30CA016672). This work was supported by individual donations (FMJ) and by the Office of the Assistant Secretary of Defense for Health Affairs through the Lung Cancer Research Program (award no. W81XWH-17-1-0206). Opinions, interpretations, conclusions, and recommendations are those of the authors and are not necessarily endorsed by the Department of Defense.

[2] Present address: Department of Comparative Biosciences, University of Illinois Urbana-Champaign, Champaign, Illinois.

Received 26 June 2018; Accepted 2 August 2018

1476-5586
https://doi.org/10.1016/j.neo.2018.08.003

Introduction

Lung cancer is the second most common cancer in men and women, with about 234,030 American adults being diagnosed with the disease in 2018 alone. Despite advances in its treatment, lung cancer remains the leading cause of cancer death [1]; patients have a five-year survival rate of less than 15%. The development of better lung cancer therapies requires a deeper understanding of the molecular signaling mechanisms that drive the disease's formation, maintenance, and progression. Cancer disease progression studies are very important in assessing response-guided treatment strategies in patients with solid tumors as they allow for clinical trial analysis to calculate time-to-event endpoints and more importantly, assist in determining clinical treatment response and/or failure.

In vivo studies in murine models play important roles in identifying the mechanisms of lung tumorigenesis and assessing the safety and efficacy of novel drug therapies. The models most commonly used to study lung tumorigenesis and therapeutic strategies are subcutaneous xenograft models created by implanting human cell lines or patient tissues into immunocompromised mice [2]. However, murine orthotopic models of lung cancer, although technically more challenging than subcutaneous models, have a tumor microenvironment more representative of that in humans, making them better suited for the study of disease progression *in vivo* [3]. Orthotopic models of lung cancer can be generated in immunocompromised or immunocompetent mice by intrabronchial injections [4], intrathoracic injections [5], tail vein injections that result in lung metastasis [6], or percutaneous injections of lung cancer cells into the left lung [7]. Most genetically engineered mouse models (GEMMs) have the advantages of being orthotopic and having an intact immune system. Many GEMMs encompass several mutations found in non–small cell lung cancer (NSCLC), including KRAS, BRAF, EGFR, LKB1, TP53, and NFκB [8]. Most GEMMs of NSCLC are adenocarcinoma models and one of the most commonly used models was established by engineering a Lox-Stop-Lox conditional KRAS G12D mutation in the endogenous KRAS locus [9,10]. Combining KRAS activation with the concomitant inactivation of p53 results in more aggressive tumors that also metastasize. The relationship between primary tumor nodules and individual metastases could be established in studies in which KRAS activation and p53 inactivation are achieved by infecting the mouse lung with lentiviral Cre [11].

The evaluation of lung cancer progression in the lungs of mice is primarily based on end-stage procedures performed after necropsy, such as histopathologically analyzing lung tissue, weighing the lungs, or counting lung tumors. Although these *ex vivo* procedures offer many opportunities to perform molecular and cellular analyses, they are limited to only one measurement and do not provide details about the dynamic processes that occur over time *in vivo*. In contrast, micro–computed tomography (micro-CT) can be used to noninvasively study the dynamic changes of tumor progression in preclinical models [12]. Although micro-CT is technically challenging because of respiratory movement artifacts, it provides visual and quantitative information about the whole lung in a three-dimensional manner with high resolution and sensitivity. More importantly, micro-CT allows for the longitudinal assessment of therapeutic interventions in different treatment groups as well as that of the extent of disease in individual mice. In addition, despite delivering a relatively large radiation dose per acquisition, micro-CT is safe, causing no radiotoxicity to the lungs of mice undergoing weekly micro-CT for up to 12 weeks [13]. However, unlike CT in humans, micro-CT in mice does not include the use of radiographic contrast, and achieving respiratory gating with micro-CT in mice is difficult.

Micro-CT has been successfully used to detect lung tumors and evaluate lung tumor burden in many NSCLC mouse models [14–16]. Methods previously used to quantify metastatic tumor burden relied on Response Evaluation Criteria in Solid Tumors (RECIST)-like assessment, in which the maximal tumor diameter and largest perpendicular diameter were measured in the coronal plane and the tumor burden was calculated from the sum of the cross products [17]. However, such methods may have reader bias, and variability has been observed among readers. In addition, these methods measure only the largest tumors and ignore small tumors that, in aggregate, may contribute significantly to the total tumor burden. Other methods that have been used to quantify tumor burden include tumor nodule segmentation [18]; segmentation of the aerated lung volume with respiratory gating [19]; manual segmentation of the chest space [16]; tracking of individual nodules [20]; modeling of tumors as ellipsoids [21]; and volumetric measurement of the combined tumor and vasculature from a threshold-based region growing algorithm with manual and semi-automated segmentation [22]. However, these methods are labor-intensive, require specific skill sets in radiology, and do not take all thoracic metastases into consideration. Murine micro-CT imaging has limitations that are not present for human CT imaging. As the murine micro-CT imaging is not respiratory gated, the probability of air escaping into the lungs and variance in the breathing period is high despite breath hold at the time of imaging. Also, tumor tissue and vasculature cannot be distinguished in the non-contrast micro-CT imaging as they have similar X-ray densities.

Therefore, we developed a semi-automated, unbiased method of analyzing micro-CT without respiratory gating for the *in vivo* quantitative assessment of lung tumor mass in mice. We propose this imaging technique and tumor mass analysis as a quantitative tool that is reliable and yields dynamic information on disease progression. Given the basic assumption that the aerated mass of the thoracic cavity (MTC) in an adult mouse does not change over time unless disease progresses, our imaging and analysis protocol is designed to permit comparisons between different groups, enable the evaluation of individual animals over time, and provide specific information about disease progression and metastasis. Unlike aerated lung volume, which is dependent upon the respiratory phase of breath hold, MTC is dependent on the differences in density between tumors and parenchymal tissue independent of respiratory state. In the present study, we evaluated our model by comparing its performance with that of with four established methods and a reference method in assessing tumor burden in a murine orthotopic model of metastatic lung cancer.

Materials and Methods

Cells

Highly metastatic 344SQ (miR200-expressing) cells were derived from transgenic mice with KRAS (G12D) TP53 (R172H) mutations (KP mice) [23] and were a generous gift from Dr. Don Gibbons. The cells were maintained in RPMI 1640 with 10% fetal bovine serum in a humidified 5% CO_2 atmosphere at 37°C as described previously [24].

Mice

All animal experiments were conducted in accordance with the laws of the United States and the regulations of the U.S. Department of Agriculture. All animal experiments were reviewed and approved

by the Institutional Animal Care and Use Committee at The University of Texas MD Anderson Cancer Center and conducted in accordance with MD Anderson's Office of Research Administration and Institutional Animal Care and Use Committee guidelines. Four- to six-week-old 129/sv male mice were purchased from Charles River Laboratory (Wilmington, MA). The mice were 8 weeks old at the start of the study. At the end of the study, lungs were embedded in paraffin and stained with hematoxylin and eosin (H&E) to check for the presence of tumor cells as described previously [25].

Murine Orthotopic Model of Lung Cancer

For the creation of the orthotopic model, the mice were first fully anesthetized with 2–4% isoflurane and placed in a right lateral decubitus position. The lower edge of the right rib cage was identified by palpation, and fur in the area was trimmed with a hair clipper. After it was cleaned with 70% ethanol solution, the area was shaved with a razor blade to remove any remaining fur. The incision site was sterilized with povidone-iodine solution. A 1-cm incision was made through the skin along the lower edge of the rib cage. The cephalic edge of the skin was retracted with forceps to reveal the underlying subcutaneous tissue and fat. A second incision was made through the fatty tissue to reveal the rib cage and the thoracic cavity. The respiring lung was identified as a pale structure under the rib cage, whereas the more caudal spleen was identified as a dark red organ. Tumor cells ($2x10^5$ 344SQ cells in 50 μl of serum free medium) were injected into the lower third of the left lung using an insulin syringe. The left lung was then checked to ensure the absence of intra-thoracic hemorrhage or collapse. For the incision closure, the opposing skin was held together with forceps and then closed with two or three 9-mm staples applied with an Autoclip stapler. The mice were then given 0.05–0.10 mg/kg buprenorphine, placed under a heat lamp, and monitored for recovery. Mice were returned to their cages once they were able to move on all four limbs.

Endotracheal Intubation and Micro-CT

Micro-CT imaging of the lungs was carried out to serve as baseline study. For micro-CT, the mice were first placed in an inhalation anesthesia induction chamber and exposed to 5% isoflurane. When the mice were fully anesthetized, a BioLite mouse intubation system (Braintree Scientific) was used to place a 22-gauge, 2.5-cm endotracheal tube. Anesthesia was then maintained with 1.5–3.0% isoflurane. The mice were then placed onto a holder and moved to the micro-CT system (XRAD 225Cx, Precision X-Ray Incorporated, North Branford, CT).The micro-CT parameters used were 60 Kv, 4 mA, and 3 RPM. The mice were mechanically ventilated at 60 BPM throughout the procedure. A 20-second breath hold at 20 cmH_2O was applied during the acquisition as described previously [26]. The pressure was monitored with an inline manometer. After the acquisition was complete, the mice were extubated and allowed to recover in a clean, warm cage.

Murine Drug Therapy

In order to validate the ability to noninvasively record patterns of lung tumor growth and response to therapy in orthotopically injected tumors, mice bearing 344SQ tumors were treated with intraperitoneal injections of vehicle only or 30 mg/kg volasertib (Selleck Chemicals, Houston, TX) once per week for 3 weeks to evaluate anticancer efficacy. Micro-CT was performed before injection (baseline) and then once per week for 3 weeks until the end of the study.

CT Image Analysis: MTC Method

The micro-CT images were exported in Digital Imaging and Communications in Medicine (DICOM) format. The DICOM image sequence was uploaded to the RayStation 5.0.2 treatment planning system (Raysearch, Sweden). The lung volume was determined based on a growing algorithm using a threshold of −800 to 0 HU to remove bias. A region of interest (ROI) in the chest cavity was drawn from the base of the lungs to the top of the trachea using RayStation's smart contour option. The MTC was calculated as a function of ROI volume and CT intensity. Tumor mass was determined by comparing the MTC of the diseased mice with the aerated MTC calculated from the baseline micro-CT images.

CT Image Analysis: Sum of Cross-Product Method

The quantification of tumor burden by the manual sum of cross-product (SCP) analysis of the micro-CT images was performed as described previously [17]. The SCP method is very similar to RECIST, a standardized measure of tumor response, especially in clinical trials [27]. The lung micro-CT DICOM images were viewed using the Fiji distribution of the NIH ImageJ software program (http://fiji.sc/Fiji). The tumors were visualized in the coronal plane, and the largest cross-sectional plane of each tumor was identified. A ruler was placed on the screen to measure the maximal tumor diameter (d_1) and largest perpendicular tumor diameter (d_2). The total tumor burden was then determined by calculating the SCP ($SCP = \sum[d_1 * d_2]$) of all tumors per animal. This method has been validated by *ex vivo* micro-CT analysis [17,28].

CT Image Analysis: Tumor and Vessel Volume Method

Tumor and vessel volume (T&V) was calculated as described previously [22]. In brief, the functional lung volume was calculated based on a region growing algorithm with the threshold value set at [−800 to 0 HU], these values were chosen empirically based on the visual inspection of a few mice on the RayStation system. The total chest space volume excluding the heart was calculated using the region growing algorithm and semi-automated contouring. The combined T&V was determined by subtracting the functional lung volume from the total chest space volume [22].

CT Image Analysis: Ellipsoidal Tumor Volume Method

The micro-CT images were viewed using the MicroView 2.2 software program (GE Healthcare). One to five tumors in each mouse were identified and selected on the axial view. The three greatest diameters of each tumor on the axial, coronal, and sagittal views (referred to as x, y, and z, respectively) were measured. These values were then used to calculate the volume of the tumor using the formula for determining the volume of an ellipsoid ($[4\pi/3][x/2][y/2][z/2]$) [29–31].

CT Image Analysis: Aerated Lung Volume Method

Functional lung volume measurement, a fully automated method that utilizes gray-level, morphological, and texture features to segment the aerated lung region using a region growing algorithm, was performed as described previously [19]. Measurement of the functional lung volume is an inverse surrogate measure of tumor burden [19]. Owing to the lack of respiratory gating facility, the aerated lung volume was measured immediately before mice were euthanized on day 33.

Statistical Analysis

Statistical analysis was carried out using GraphPad Prism 7 software (GraphPad, La Jolla, CA). One-way analysis of variance and the Tukey's multiple comparison test were used to assess changes in the MTCs of the disease-free mice over time in comparison to baseline. Pearson correlation was used to compare tumor burden calculated using the different

methods with lung weight and with MTC method. All data values presented are mean ± standard deviation (SD), and the error bars on the graphs represent standard error of mean (SEM).

Results

The MTCs of Adult Mice Do Not Change Over Time

To test the assumption that the aerated MTC does not change over time unless the tumor burden changes, we periodically imaged five non–tumor-bearing mice using the same schedule as that used for the tumor-bearing mice and calculated the MTC. The MTCs of non–tumor-bearing mice did not change over time (Figure 1, *A* and *B*); the percent change in MTC was 0 ± 0.2 ($P > .99$). No changes in MTC were observed despite the mice being at different breath hold stages during image acquisition.

However, aerated lung volume in the same mice varied significantly over time, likely because the breath holds for the imaging were initiated at random respiratory states (Figure 1*C*). The

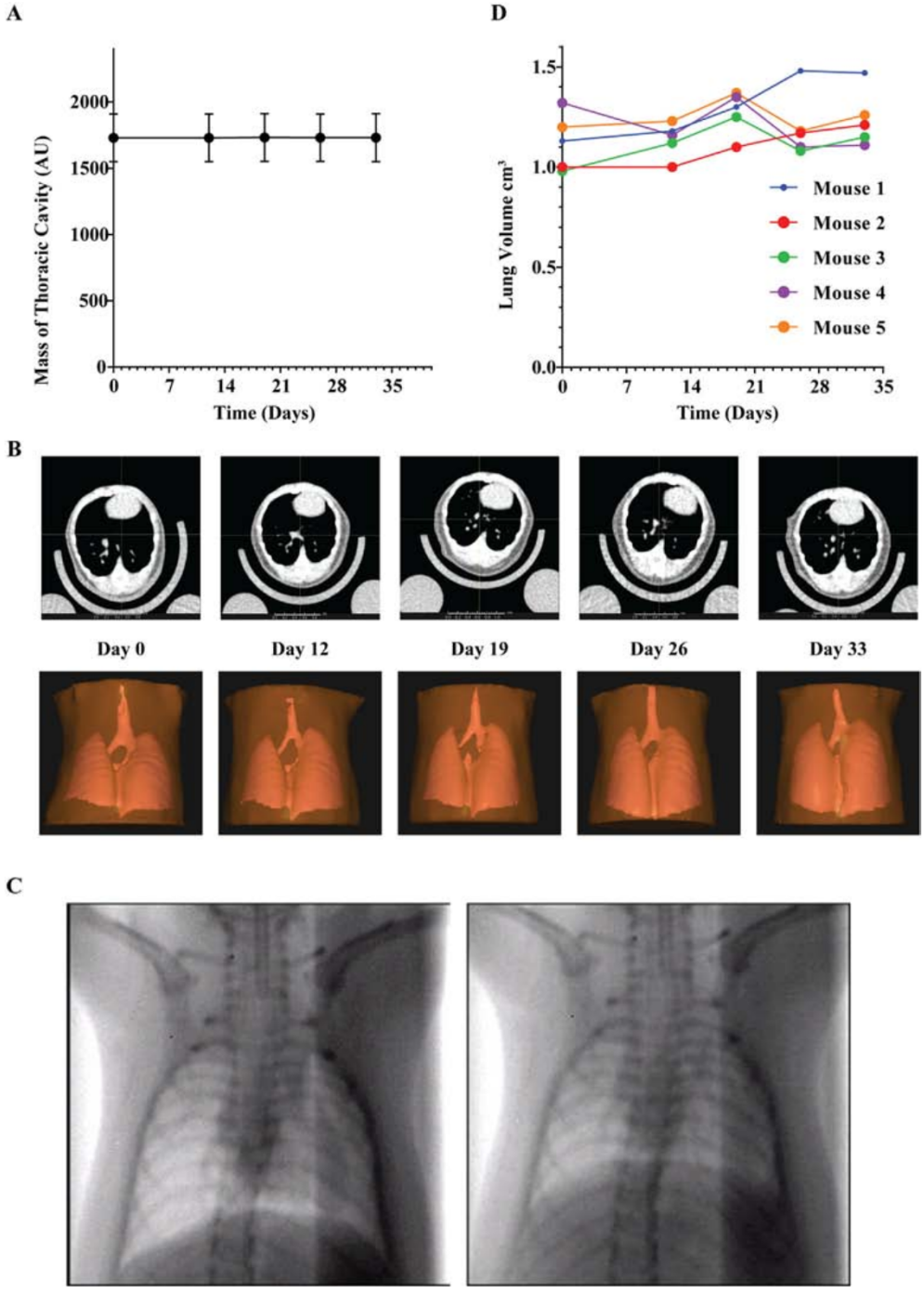

Figure 1. The MTC does not change over time in tumor-free mice. **(A)** The MTCs of five non–tumor-bearing mice were calculated over time as a product of volume and intensity. The error bars show standard deviations. **(B)** Representative micro-CT images (upper panel) and MTCs (lower panel) of non–tumor-bearing mice over time. **(C)** Representative scout images of breath hold in mice after tracheal intubation. **(D)** Aerated lung volumes of non–tumor-bearing mice over time. AU, arbitrary units.

percent changes in lung volume on days 12, 19, 26, and 33 were 1.8 ± 9.5, 13.8 ± 9.2, 8.0 ± 18.1, and 11.5 ± 17.8, respectively (Figure 1*D*). This substantial variability suggests that the measured aerated lung volume does not accurately depict disease progression over time.

Quantitative Measurement of Lung Tumor Mass in a Murine Orthotopic Lung Cancer Model Accurately Determines Tumor Burden

Eleven mice were imaged at baseline and the MTC was calculated. 344SQ murine lung adenocarcinoma cells were then injected into the left lung of the mice *via* orthotopic injection. The mice were then serially imaged on days 12, 19, 26 and 33 to study the course of tumor development and MTC was calculated. The tumor mass was then calculated by subtracting the MTC on the specific day from the baseline MTC (Figure 2*A*). Tumor-bearing mice survived an average of 3 weeks after the 344SQ cell injection. The mice were euthanized when they were moribound or on day 33 immediately after the last micro-CT imaging session. The mice were necropsied, the number of primary and metastatic tumors were counted and the lungs were collected and weighed. The calculated tumor mass was then compared to the gold standard of tumor burden, lung weight. Tumor mass calculated using the MTC method was correlated with lung weight (r = 0.78, P = .005) (Figure 2*B*).

Lung Tumor Burden Measured Using Established Methods Correlates with Lung Weight

We evaluated four other methods of lung tumor burden measurement: the RECIST-like method (SCP) [17]; aerated lung volume [19] without respiratory gating; volumetric measurement of combined tumor and vasculature from a threshold-based region growing algorithm with manual and semi-automated segmentation (T&V) [22]; and the ellipsoid tumor burden measurement [21]. To determine the intrinsic accuracy of each method in determining tumor burden, the tumor burden of the same 10 mice with lung adenocarcinoma was calculated using each method and compared to lung weight. Lung weight correlated with tumor burden measured using the SCP method (r = 0.63, P = .03) (Figure 3*A*), ellipsoid tumor volume method (r = 0.78, P = .004) (Figure 3*B*), T&V method (r = 0.65, P = .02) (Figure 3*C*), and aerated lung volume method (r = −0.69, P = .01) (Figure 3*D*), confirming that these methods can accurately determine tumor burden in mice with lung adenocarcinoma.

Comparison of Methods of Lung Tumor Burden Quantification with MTC Method

The tumor burdens calculated with four established methods were plotted against the tumor mass calculated with our MTC method. Tumor burden calculated using the MTC method correlated significantly with all the methods of tumor burden quantification including the SCP method (r = 0.69, P = .0006) (Figure 4*A*); the ellipsoid tumor volume method (r = 0.62, P = .003) (Figure 4*B*); the T&V method (r = 0.51, P = .01) (Figure 4*C*); and the aerated lung volume method (r = −0.60, P = .0044) (Figure 4*D*). Features of the MTC method, the other four micro-CT analysis methods of tumor burden measurement, and the reference method (lung weight assessment) are shown in Table 1.

Application Study for MTC Method Demonstrates that Volasertib Treatment Reduces Tumor Mass in an Orthotopic Mouse Model of Mesenchymal Metastasis

To test the MTC method in an independent dataset, we assessed the anti-cancer effect of the polo-like kinase 1 (PLK1)

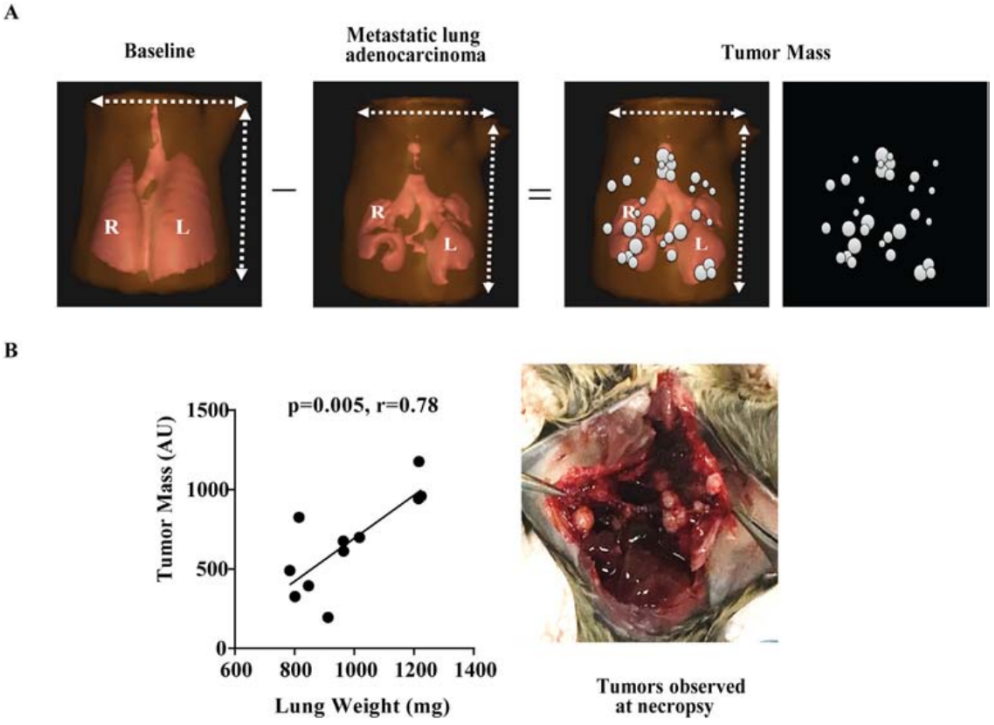

Figure 2. Tumor mass calculated using the MTC method accurately measures thoracic tumor burden in a murine orthotopic model of lung cancer. (**A**) Representative images illustrating the MTC method of calculating tumor burden. The baseline MTC is calculated before cancer cell injection. Tumor mass is calculated by subtracting the MTC of the tumor-bearing mouse from the mouse's baseline MTC. (**B**) Tumor mass calculated using the MTC method on day 33 was correlated with lung weight at the end of the experiment (day 33).

inhibitor volasertib in an orthotopic mouse model. Our previous work suggested that PLK1 inhibition would be effective against mesenchymal NSCLC [32,33]. Epithelial-mesenchymal transition (EMT) is an important process during the progression of lung cancer. Epithelial cells lose the polarity, which contributes to uncontrolled invasion and metastasis of cancer cells. Most lung cancer patients have an extensive array of secondary tumor sites, which are established through the metastatic cascade of which EMT is a direct regulator.

Twenty-five mice were imaged at baseline. We injected 344SQ cells into the left lungs of 20 mice. On day 12 (*i.e.*, 12 days after tumor cell injection), the mice had measurable tumors and were randomized to receive weekly intravenous injections of vehicle only (control) or 30 mg/kg volasertib for 4 weeks. Five mice that did not receive cancer cell injections served as negative controls. All mice were serially imaged on days 12, 19, 26, and 33.

We found significant differences in the tumor mass calculated using the MTC method between the vehicle and volasertib-treated

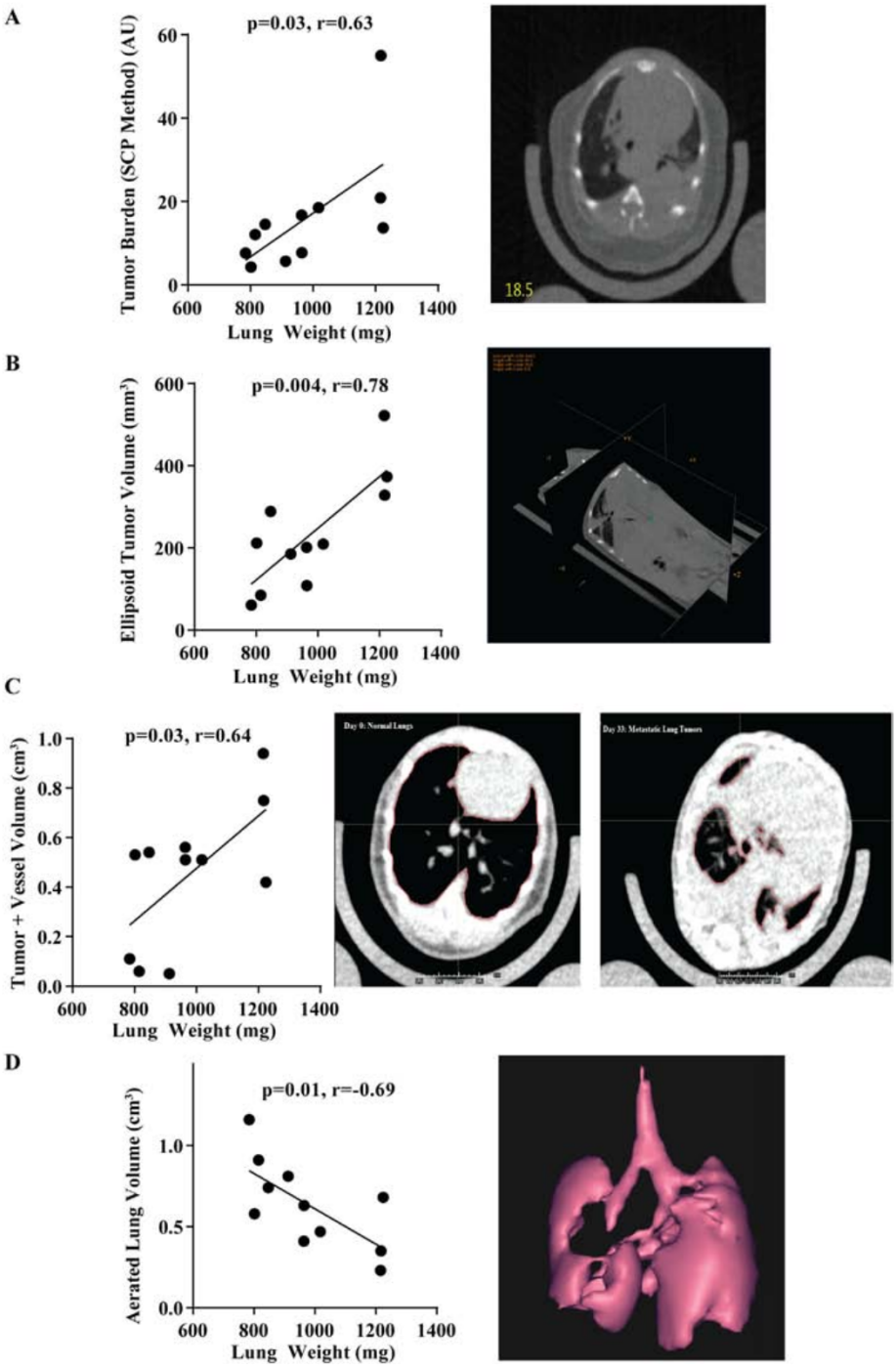

Figure 3. Lung tumor burden assessed using four established methods correlated well with tumor mass estimated using lung weight. Lung weight in 11 mice at the end of the experiment was compared with tumor burden as measured using the SCP (**A),** ellipsoid tumor volume (**B**), T&V (**C**), and aerated lung volume (**D**) methods. Pearson correlation was used to compute the R values. The representative images for calculation of tumor burden for each method is also represented.

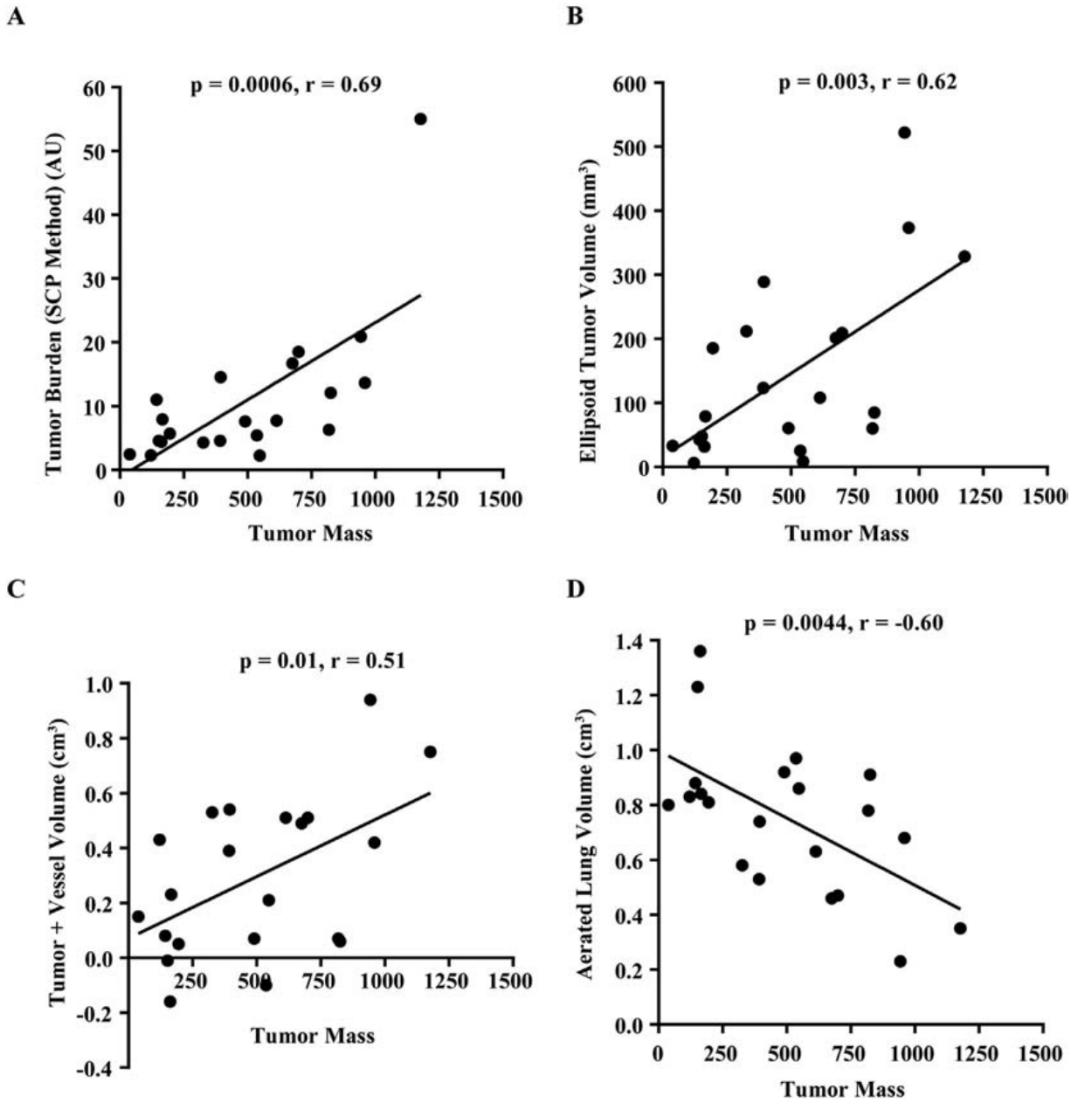

Figure 4. Tumor mass calculated using the MTC method correlated with tumor burden measured using four established techniques. Tumor mass calculated using the MTC method was compared with tumor burden measured using the SCP method (**A**), ellipsoid tumor volume method (**B**), T&V method (**C**), and end point lung volume method (**D**). Pearson correlation was used to compute the R values.

mice on days 19 ($P = .035$), 26 ($P = .008$), and 33 ($P = .004$) (Figure 5*A*). We also found a significant difference in the percent change in tumor mass at day 33 between the control and volasertib-treated mice ($P = .0064$) based on non-parametric Mann–Whitney t-test analysis (Figure 5*B*) depicting tumor regression in the mice treated with volasertib compared to the vehicle control treated mice at the end of the study. All 10 mice treated with volasertib had stable disease or regression, whereas all but one of the 11 control mice had an increase in tumor mass (Figure 5*C*). Hematoxylin and eosin staining of lung tissues collected at the end of treatment showed that the lungs of the control mice had many tumor cells present, whereas the lungs of the volasertib-treated mice had very few tumor cells remaining (Figure 5*D*). Representative images of the control and volasertib-treated mice over time are shown in Figure 5*E*.

Table 1. Comparison of Different Methods of Measuring Lung Tumor Burden

	MTC Method (Study Method)	SCP (RECIST-Like) Method	Ellipsoidal Method	T&V Volume Method	Aerated Lung Volume Method	Lung Weight (Reference Method)
Primary tumor measurement	YES	YES	YES	YES	YES	YES
Metastatic of parenchymal lung tumors	ALL	Largest 5	Largest 5	ALL	ALL	ALL
Measurement of extra-parenchymal thoracic tumors	YES	NO	NO	NO	NO	NO
Dynamic changes in tumor volume or mass	YES	YES	YES	YES	NO	NO
Semi-automated analysis	YES	NO	NO	YES	YES	NO
Dimensional measurement	3D	2D	3D	3D	3D	
Time taken for analysis per mouse	5–8 min	12–15 min	15–20 min	10–15 min	3–5 min	2–5 min
Software/tool used	RayStation	ImageJ	MicroView	RayStation	RayStation	Surgical tools and weighing scale
Correlation with reference method (R value/p value)	0.78/0.005	0.63/0.03	0.78/0.004	0.65/0.02	–0.69/0.01	

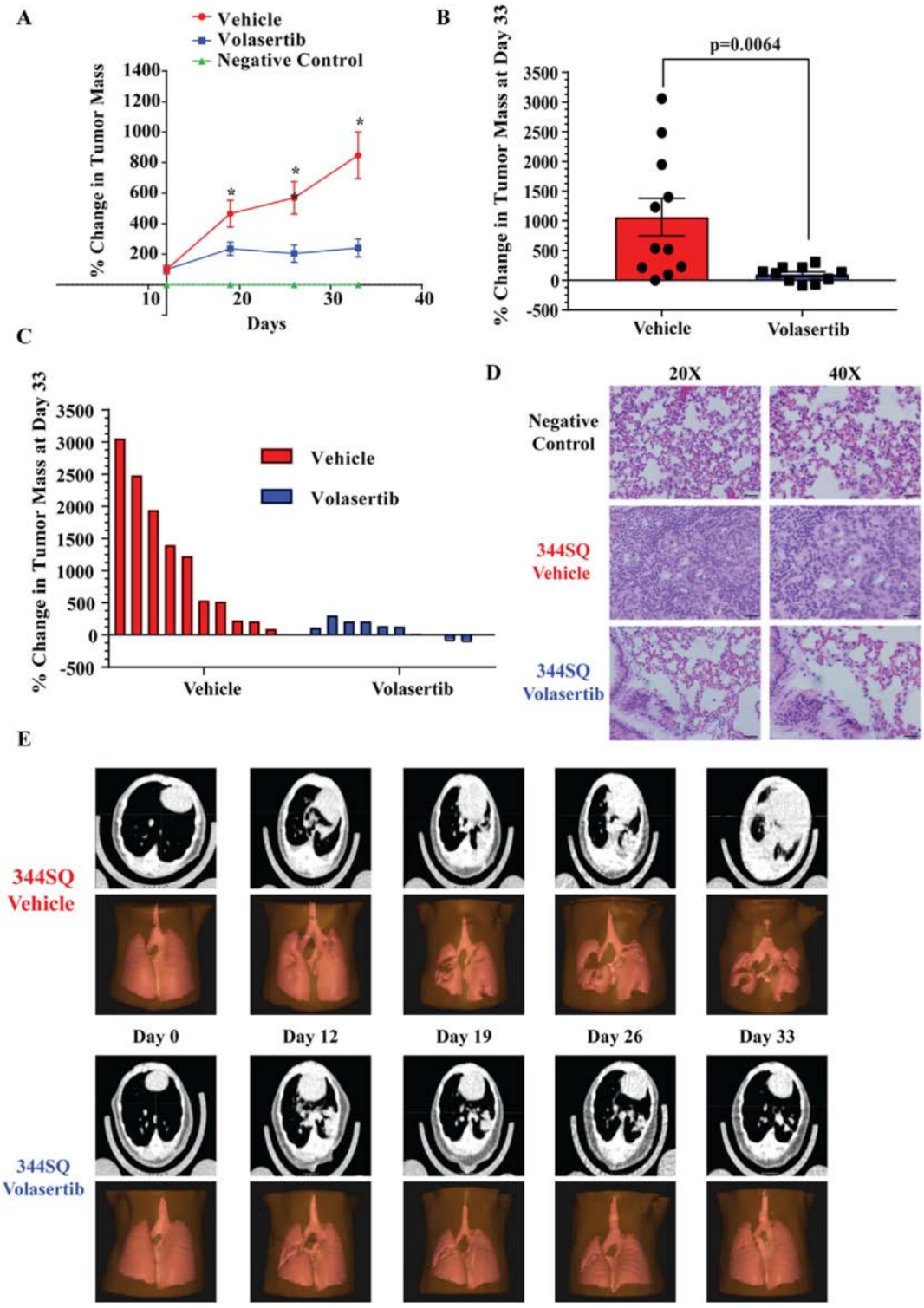

Figure 5. Tumor mass measured with the MTC method accurately reflected the effect of PLK1 inhibition in a murine orthotopic model of mesenchymal metastatic NSCLC. Mice without cancer (negative control) and 344SQ tumor-bearing mice treated with volasertib or vehicle starting on day 12 underwent micro-CT imaging on days 12, 19, 26, and 33 and tumor mass was calculated using the MTC method. **(A–C)** The percent change in tumor mass from day 12 to the indicated time point for each treatment group (**A-B**) and for each individual tumor (**C**). Error bars represent standard deviations. *$P < .05$. Representative hematoxylin and eosin–stained lung sections at the end of the experiment (**D**) and representative micro-CT and 3D MTC images over time (**E**) of negative control mice and mice bearing 344SQ tumors treated with vehicle only or with volasertib are shown.

Discussion

In the current study, we utilized micro-CT imaging in a KRAS/p53-driven orthotopic lung cancer model to monitor lung cancer initiation and progression. We developed a micro-CT image analysis method to quantitatively measure tumor mass as a measure of total thoracic tumor burden in murine lung cancer models. This method of tumor

mass calculation takes into account both the primary and the metastatic tumors present in the thoracic cavity from the base of the lung to the top of the trachea. In addition, we successfully demonstrated the efficacy of PLK1 inhibition in a mesenchymal metastatic lung orthotopic mouse model by using micro-CT imaging. These results highlight the advantage of micro-CT guided analysis that makes it possible to measure tumor development, select animals with a certain range of tumor size, and follow response to drug treatment.

We found that tumor mass calculated using our MTC method was strongly correlated with lung weight in the murine orthotopic lung cancer model (r = 0.78), which demonstrates that our method can be used to accurately assess the growth of intra- and extra-parenchymal tumors in mice over time. We also found that tumor mass calculated with our MTC method was strongly correlated with the tumor burden calculated with all tested methods including the SCP method [17], whose process of using of bi-directional measurements to assess tumor response to therapy is similar to that used with RECIST and World Health Organization criteria. RECIST is the most common method used to estimate tumor burden in humans with cancer. We noticed that the MTC method outperformed the other four methods in the three mice with the highest tumor burdens as determined by lung weight. One of the possible reasons for this finding is that growing tumors sometimes meld together, making them difficult to distinguish, which leads to inaccurate estimations of tumor burden by methods that rely on the measurement of multiple individual tumors. The advantage of the MTC method over the four other tested methods is the accurate measurement of extra-parenchymal metastatic tumors in tumor burden calculation in a rapid manner.

The MTC method could be applied to assess tumor burden in GEMMs of lung cancer because GEMMs mimic human disease by the metastatic spread of *de novo* tumors in an immune-competent microenvironment. GEMM models are very important for studying lung cancer biology and for preclinical drug studies, as they have a tumor microenvironment that more closely reflects that in humans and thus could predict drug responses better than subcutaneous tumor models can. GEMMs are used to study the cellular processes that contribute to cancer initiation, progression, and metastasis. The GEMMs that recapitulate the natural history of human cancers and their clinical response to therapy constitute a major prerequisite for bench-to-bedside translation of investigational anticancer therapies and diagnostic imaging. Also, the evaluation of mouse models of lung cancer has improved our understanding of the genetic processes that lead to known genetic phenotypes of the disease, varying lung cancer histopathology, and certain tumor cell characteristics [34].

One limitation of our study is that the T&V method may not have been faithfully reproduced because the software used for that method is not commercially available. We used RayStation to calculate the tumor and vessel volume, and we used a threshold based on RayStation that is not the same as that suggested by Haines et al. [22]. A second limitation is that the measured mass using MTC might not include just tumor mass but also include blood mass due to thoracic hemorrhaging that occurs because of incorrect intubation and the extra-calcification of the rib cage. Lung obstruction with resulting lung collapse can also affect tumor measurement with all methods. Also, the presented method does not address a potential heterogeneity of treatment response in tumors, which would require identification and measurement of individual tumors at different times. We also did not histologically quantify tumors to determine the extent to which such measurements are correlated with tumor mass.

In conclusion, the findings of the present study demonstrate that our MTC method for the longitudinal assessment of lung cancer progression in murine models is unbiased, rapid, and accurate. Given that the software we used is commercially available, the method will be easy for others to reproduce. Combining this method with high-throughput micro-CT scanning in preclinical research could provide a rapid means of assessing tumor burden to help advance our understanding of lung cancer progression.

Acknowledgments

We thank Joe Munch in MD Anderson's Department of Scientific Publications for editing the manuscript.

References

[1] Siegel RL, Miller KD, and Jemal A (2018). Cancer statistics, 2018. *CA Cancer J Clin* **68**, 7–30.

[2] Hoffman RM (1999). Orthotopic metastatic mouse models for anticancer drug discovery and evaluation: a bridge to the clinic. *Investig New Drugs* **17**, 343–359.

[3] Killion JJ, Radinsky R, and Fidler IJ (1998). Orthotopic models are necessary to predict therapy of transplantable tumors in mice. *Cancer Metastasis Rev* **17**, 279–284.

[4] McLemore TL, Liu MC, Blacker PC, Gregg M, Alley MC, Abbott BJ, Shoemaker RH, Bohlman ME, Litterst CC, and Hubbard WC, et al (1987). Novel intrapulmonary model for orthotopic propagation of human lung cancers in athymic nude mice. *Cancer Res* **47**, 5132–5140.

[5] McLemore TL, Eggleston JC, Shoemaker RH, Abbott BJ, Bohlman ME, Liu MC, Fine DL, Mayo JG, and Boyd MR (1988). Comparison of intrapulmonary, percutaneous intrathoracic, and subcutaneous models for the propagation of human pulmonary and nonpulmonary cancer cell lines in athymic nude mice. *Cancer Res* **48**, 2880–2886.

[6] Goto H, Yano S, Zhang H, Matsumori Y, Ogawa H, Blakey DC, and Sone S (2002). Activity of a new vascular targeting agent, ZD6126, in pulmonary metastases by human lung adenocarcinoma in nude mice. *Cancer Res* **62**, 3711–3715.

[7] Onn A, Isobe T, Itasaka S, Wu W, O'Reilly MS, Ki Hong W, Fidler IJ, and Herbst RS (2003). Development of an orthotopic model to study the biology and therapy of primary human lung cancer in nude mice. *Clin Cancer Res* **9**, 5532–5539.

[8] Kwon MC and Berns A (2013). Mouse models for lung cancer. *Mol Oncol* **7**, 165–177.

[9] Guerra C, Mijimolle N, Dhawahir A, Dubus P, Barradas M, Serrano M, Campuzano V, and Barbacid M (2003). Tumor induction by an endogenous K-ras oncogene is highly dependent on cellular context. *Cancer Cell* **4**, 111–120.

[10] Jackson EL, Willis N, Mercer K, Bronson RT, Crowley D, Montoya R, Jacks T, and Tuveson DA (2001). Analysis of lung tumor initiation and progression using conditional expression of oncogenic K-ras. *Genes Dev* **15**, 3243–3248.

[11] Winslow MM, Dayton TL, Verhaak RG, Kim-Kiselak C, Snyder EL, Feldser DM, Hubbard DD, DuPage MJ, Whittaker CA, and Hoersch S, et al (2011). Suppression of lung adenocarcinoma progression by Nkx2–1. *Nature* **473**, 101–104.

[12] Gammon ST, Foje N, Brewer EM, Owers E, Downs CA, Budde MD, Leevy WM, and Helms MN (2014). Preclinical anatomical, molecular, and functional imaging of the lung with multiple modalities. *Am J Physiol Lung Cell Mol Physiol* **306**, L897–L914.

[13] Vande Velde G, De Langhe E, Poelmans J, Bruyndonckx P, d'Agostino E, Verbeken E, Bogaerts R, Lories R, and Himmelreich U (2015). Longitudinal in vivo microcomputed tomography of mouse lungs: No evidence for radiotoxicity. *Am J Physiol Lung Cell Mol Physiol* **309**, L271–L279.

[14] De Clerck NM, Meurrens K, Weiler H, Van Dyck D, Van Houtte G, Terpstra P, and Postnov AA (2004). High-resolution X-ray microtomography for the detection of lung tumors in living mice. *Neoplasia* **6**, 374–379.

[15] Cavanaugh D, Johnson E, Price RE, Kurie J, Travis EL, and Cody DD (2004). In vivo respiratory-gated micro-CT imaging in small-animal oncology models. *Mol Imaging* **3**, 55–62.

[16] Fushiki H, Kanoh-Azuma T, Katoh M, Kawabata K, Jiang J, Tsuchiya N, Satow A, Tamai Y, and Hayakawa Y (2009). Quantification of mouse pulmonary cancer models by microcomputed tomography imaging. *Cancer Sci* **100**, 1544–1549.

[17] Singh M, Lima A, Molina R, Hamilton P, Clermont AC, Devasthali V, Thompson JD, Cheng JH, Bou Reslan H, and Ho CC, et al (2010). Assessing therapeutic responses in Kras mutant cancers using genetically engineered mouse models. *Nat Biotechnol* **28**, 585–593.

[18] Namati E, Thiesse J, Sieren JC, Ross A, Hoffman EA, and McLennan G (2010). Longitudinal assessment of lung cancer progression in the mouse using in vivo micro-CT imaging. *Med Phys* **37**, 4793–4805.

[19] Rodt T, von Falck C, Dettmer S, Hueper K, Halter R, Hoy L, Luepke M, Borlak J, and Wacker F (2012). Lung tumour growth kinetics in SPC-c-Raf-1-BB transgenic mice assessed by longitudinal in-vivo micro-CT quantification. *J Exp Clin Cancer Res* **31**, 15–21.

[20] Rudyanto RD, Bastarrika G, de Biurrun G, Agorreta J, Montuenga LM, Ortiz-de-Solorzano C, and Munoz-Barrutia A (2013). Individual nodule tracking in micro-CT images of a longitudinal lung cancer mouse model. *Med Image Anal* **17**, 1095–1105.

[21] Li XF, Zanzonico P, Ling CC, and O'Donoghue J (2006). Visualization of experimental lung and bone metastases in live nude mice by X-ray micro-computed tomography. *Technol Cancer Res Treat* **5**, 147–155.

[22] Haines BB, Bettano KA, Chenard M, Sevilla RS, Ware C, Angagaw MH, Winkelmann CT, Tong C, Reilly JF, and Sur C, et al (2009). A quantitative volumetric micro-computed tomography method to analyze lung tumors in genetically engineered mouse models. *Neoplasia* **11**, 39–47.

[23] Gill BJ, Gibbons DL, Roudsari LC, Saik JE, Rizvi ZH, Roybal JD, Kurie JM, and West JL (2012). A synthetic matrix with independently tunable biochemistry and mechanical properties to study epithelial morphogenesis and EMT in a lung adenocarcinoma model. *Cancer Res* **72**, 6013–6023.

[24] Ungewiss C, Rizvi ZH, Roybal JD, Peng DH, Gold KA, Shin DH, Creighton CJ, and Gibbons DL (2016). The microRNA-200/Zeb1 axis regulates ECM-dependent beta1-integrin/FAK signaling, cancer cell invasion and metastasis through CRKL. *Sci Rep* **6**, 18652.

[25] Gibbons DL, Lin W, Creighton CJ, Rizvi ZH, Gregory PA, Goodall GJ, Thilaganathan N, Du L, Zhang Y, and Pertsemlidis A, et al (2009). Contextual extracellular cues promote tumor cell EMT and metastasis by regulating miR-200 family expression. *Genes Dev* **23**, 2140–2151.

[26] Rivera B, Bushman MJ, Beaver RG, Cody DD, and Price RE (2006). Breath-hold device for laboratory rodents undergoing imaging procedures. *J Am Assoc Lab Anim Sci* **45**, 54–59.

[27] Eisenhauer EA, Therasse P, Bogaerts J, Schwartz LH, Sargent D, Ford R, Dancey J, Arbuck S, Gwyther S, and Mooney M, et al (2009). New response evaluation criteria in solid tumours: revised RECIST guideline (version 1.1). *Eur J Cancer* **45**, 228–247.

[28] Schindelin J, Arganda-Carreras I, Frise E, Kaynig V, Longair M, Pietzsch T, Preibisch S, Rueden C, Saalfeld S, and Schmid B, et al (2012). Fiji: an open-source platform for biological-image analysis. *Nat Methods* **9**, 676–682.

[29] Dachman AH, MacEneaney PM, Adedipe A, Carlin M, and Schumm LP (2001). Tumor size on computed tomography scans: is one measurement enough? *Cancer* **91**, 555–560.

[30] Asteriti IA, De Mattia F, and Guarguaglini G (2015). Cross-talk between AURKA and Plk1 in Mitotic Entry and Spindle Assembly. *Front Oncol* **5**, 283–291.

[31] Sapi J, Kovacs L, Drexler DA, Kocsis P, Gajari D, and Sapi Z (2015). Tumor volume estimation and quasi-continuous administration for most effective bevacizumab therapy. *PLoS One* **10**e0142190.

[32] Ferrarotto R, Goonatilake R, Young Yoo S, Tong P, Giri U, Peng S, Minna J, Girard L, Wang Y, and Wang L, et al (2016). Epithelial-mesenchymal transition predicts polo-like kinase 1 inhibitor-mediated apoptosis in non-small cell lung cancer. *Clin Cancer Res* **22**, 1674–1686.

[33] Wang Y, Singh R, Wang L, Nilsson M, Goonatilake R, Tong P, Li L, Giri U, Villalobos P, and Mino B, et al (2016). Polo-like kinase 1 inhibition diminishes acquired resistance to epidermal growth factor receptor inhibition in non-small cell lung cancer with T790M mutations. *Oncotarget* **7**, 47998–48010.

[34] Safari R and Meuwissen R (2015). Practical use of advanced mouse models for lung cancer. *Methods Mol Biol* **1267**, 93–124.

Modern Pathology (2018) 31:947–955
https://doi.org/10.1038/s41379-018-0029-3

ARTICLE

Multiregion gene expression profiling reveals heterogeneity in molecular subtypes and immunotherapy response signatures in lung cancer

Won-Chul Lee[1,2] · Lixia Diao[3] · Jing Wang[3] · Jianhua Zhang[1] · Emily B. Roarty[2] · Susan Varghese[2] · Chi-Wan Chow[4] · Junya Fujimoto[4] · Carmen Behrens[2] · Tina Cascone[2] · Weiyi Peng[5] · Neda Kalhor[6] · Cesar A. Moran[6] · Annikka Weissferdt[6] · Faye M. Johnson[2] · William N. William Jr.[2] · Stephen G. Swisher[7] · J. Jack Lee[8] · Waun Ki Hong[2] · John V. Heymach[2] · Ignacio I. Wistuba[2,4] · P. Andrew Futreal[1] · Jianjun Zhang[1,2]

Received: 25 October 2017 / Revised: 7 December 2017 / Accepted: 10 December 2017 / Published online: 6 February 2018

Abstract

Intra-tumor heterogeneity may be present at all molecular levels. Genomic intra-tumor heterogeneity at the exome level has been reported in many cancer types, but comprehensive gene expression intra-tumor heterogeneity has not been well studied. Here, we delineated the gene expression intra-tumor heterogeneity by exploring gene expression profiles of 35 tumor regions from 10 non-small cell lung cancer tumors (three or four regions/tumor), including adenocarcinoma, squamous cell carcinoma, large-cell carcinoma, and pleomorphic carcinoma of the lung. Using Affymetrix Gene 1.0 ST arrays, we generated the gene expression data for every sample. Inter-tumor heterogeneity was generally higher than intra-tumor heterogeneity, but some tumors showed a substantial level of intra-tumor heterogeneity. The analysis of various clinically relevant gene expression signatures including molecular subtype, epithelial-to-mesenchymal transition, and anti-PD-1 resistance signatures also revealed heterogeneity between different regions of the same tumor. The gene expression intra-tumor heterogeneity we observed was associated with heterogeneous tumor microenvironments represented by stromal and immune cells infiltrated. Our data suggest that RNA-based prognostic or predictive molecular tests should be carefully conducted in consideration of the gene expression intra-tumor heterogeneity.

Cancers are heterogeneous diseases. Substantial inter-tumor heterogeneity of many cancers has been well documented [1]. Heterogeneity also exists within individual tumors, as a single tumor can display multiple different molecular features within it, a phenomenon termed intra-tumor heterogeneity. Genomic intra-tumor heterogeneity has been

These authors contributed equally: Won-Chul Lee, Lixia Diao, Jing Wang.

Electronic supplementary material The online version of this article (https://doi.org/10.1038/s41379-018-0029-3) contains supplementary material, which is available to authorized users.

✉ Ignacio I. Wistuba
iiwistuba@mdanderson.org

✉ P. Andrew Futreal
afutreal@mdanderson.org

✉ Jianjun Zhang
jzhang20@mdanderson.org

[1] Department of Genomic Medicine, The University of Texas MD Anderson Cancer Center, Houston, TX, USA

[2] Department of Thoracic/Head and Neck Medical Oncology, The University of Texas MD Anderson Cancer Center, Houston, TX, USA

[3] Department of Bioinformatics and Computational Biology, The University of Texas MD Anderson Cancer Center, Houston, TX, USA

[4] Department of Translational Molecular Pathology, The University of Texas MD Anderson Cancer Center, Houston, TX, USA

[5] Department of Melanoma Medical Oncology, The University of Texas MD Anderson Cancer Center, Houston, TX, USA

[6] Department of Pathology, The University of Texas MD Anderson Cancer Center, Houston, TX, USA

[7] Department of Thoracic Surgery, The University of Texas MD Anderson Cancer Center, Houston, TX, USA

[8] Department of Biostatistics, The University of Texas MD Anderson Cancer Center, Houston, TX, USA

reported in both hematologic and solid tumors and may be associated with treatment failure and emergence of drug resistance [2]. Gerlinger and colleagues [3, 4] demonstrated profound genomic intra-tumor heterogeneity in renal cell carcinomas using a multiregion whole-exome sequencing approach. Using similar approach, our group [5] and de Bruin et al. [6] have independently shown clear evidence of genomic intra-tumor heterogeneity of non-small cell lung cancers, but to a much less extent compared to that in renal cell carcinomas, suggesting different cancers may have different genomic intra-tumor heterogeneity architecture.

RNA and protein expression intra-tumor heterogeneity has also been studied, but only at single gene and limited gene panel levels. For example, spatial heterogeneity of estrogen receptor and human epidermal growth factor receptor 2 (HER-2) protein was reported in breast cancers [7, 8] and HER-2 protein expression was found to be discordant between different regions within the same gastric cancers [9]. Gyanchandani and colleagues [10] analyzed five RNA expression-based prognostic panels on 181 tumor samples from 71 estrogen receptor-positive breast cancers and revealed discordant risk of recurrence by using different regions from the same tumors, suggesting that a single biopsy could either under- or over-estimate recurrence risks of breast cancer due to the intra-tumor heterogeneity. To the best of our knowledge, comprehensive gene expression intra-tumor heterogeneity is not well defined in any cancer types. Here, we present our analyses of gene expression profiles of 35 spatially separated regions from 10 patients with resected non-small cell lung cancer.

Materials and methods

Multiregion sampling and clinical information

We collected 35 tumor samples from 10 patients with non-small cell lung cancer (three or four regions/tumor) including lung adenocarcinoma ($n = 6$), squamous cell carcinoma ($n = 2$), large-cell carcinoma ($n = 1$), and pleomorphic carcinoma ($n = 1$). Multiregion sampling was done as illustrated in Supplementary Figure 1. Detailed clinical information for every patient, such as tumor size, stage, prognosis, and treatment history, can be found in Supplementary Table 1.

Data preprocessing and normalization

The gene expression data were generated by using the Affymetrix GeneChip® Human Gene 1.0 ST arrays. The platform contains 33,252 transcript clusters (corresponding to 20,009 unique genes). The R package, aroma.affymetrix, was used to process the expression measurements. Briefly, the CEL formatted files were loaded first, and then the robust multiarray analysis method was used for data processing and background adjustment. The background-corrected measurements were then logarithm transformed (base 2) and quantile normalization was applied.

Gene annotation to transcript cluster

Once the data were processed, we updated the annotation based on the most recent annotation file (HuGene-1_0-st-v1.na36.hg19.transcript.csv, 7/6/16) obtained from the NetAffx™ Analysis Center of Affymetrix, and annotated transcript clusters with NCBI RefSeq genes. For a cluster with multiple unique gene symbols, we aligned the sequence of the cluster with each of the candidate genes using bl2seq (BLAST 2 Sequences) in BLAST package (v2.2.12). A gene with the highest bit-score was considered as the gene for the cluster. If multiple genes show the same best score for a cluster, we assigned them all to the cluster.

Unique gene-level expression profiling

If a gene is assigned with only one transcript cluster, the cluster represents the expression level of the gene. If multiple transcript clusters point to the same gene, we first calculated Pearson correlation coefficient between them and took the average if they are correlated ($r > 0.7$). Otherwise, individual sequences from the clusters were compared with the gene sequence with bl2seq, and the best matching cluster was selected to represent expression level for the gene. If there are multiple transcript clusters reaching the same best score, we selected one with the highest average expression level across all samples.

Molecular subtyping and epithelial–mesenchymal transition score calculation

To calculate molecular subtype scores, we obtained subtype predictor centroids for lung adenocarcinoma and squamous cell carcinoma [11, 12]. For lung adenocarcinoma, we renamed subtypes as proposed by The Cancer Genome Atlas [13]: bronchioid to terminal respiratory unit, magnoid to proximal proliferative, and squamoid to proximal inflammatory. Molecular subtype scores were calculated with the method previously used [14]. Briefly, we used the following procedure: (i) extracting expression values of the genes overlapped with the gene lists of subtype centroids, (ii) mean centering within the specific histological group (adenocarcinoma or squamous), (iii) averaging the expression values if there are multiple probes indicating the same gene, (iv) calculating Spearman rank correlation between values of a given sample and centroids, and (v) selecting the subtype showing the highest correlation coefficient with p

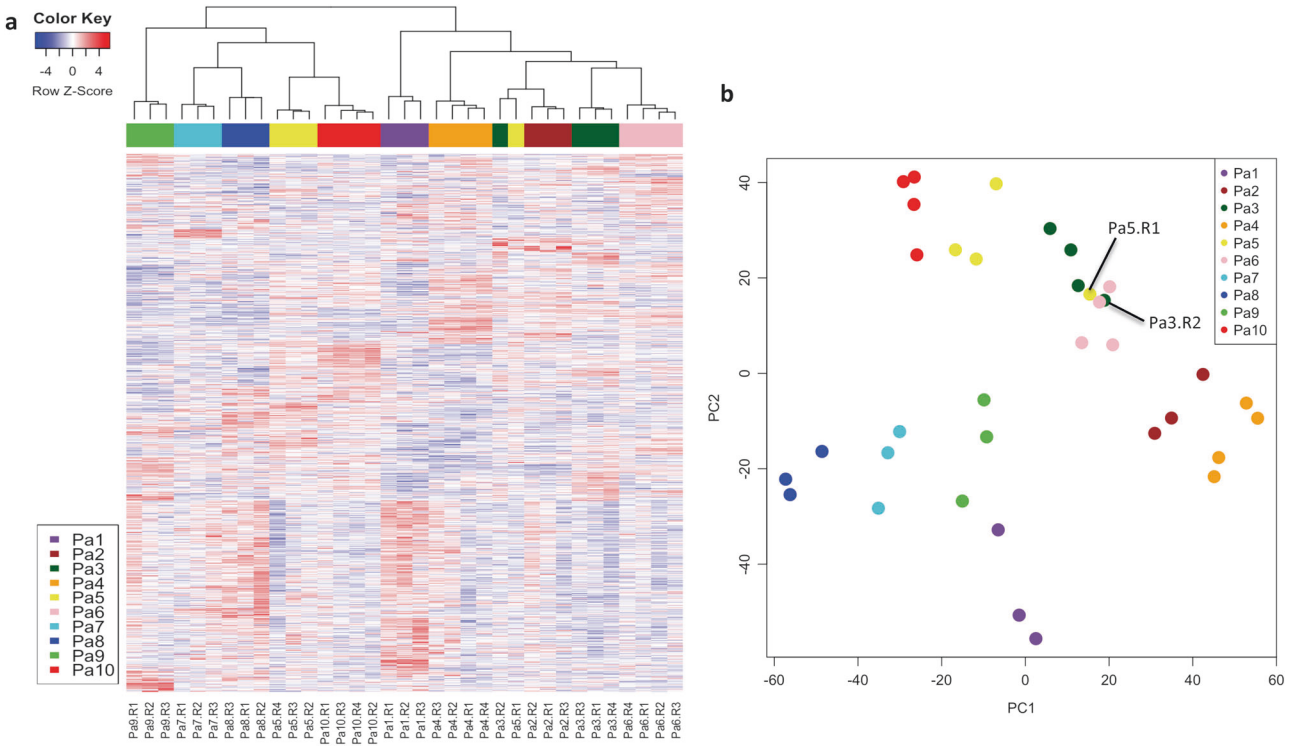

Fig. 1 **a** Heat map generated by unsupervised hierarchical clustering with all transcript clusters ($n = 21{,}052$). The 1-correlation distance and ward.D2 linkage were used for clustering. The rows and columns represent transcript clusters and tumor samples, respectively. Samples from the same patients were illustrated in the same colors below the column dendrogram. **b** Principal component analysis plot with the two dimensions (PC1 and PC2) along which the data are the largest spread. Samples from the same patients were shown in the same colors. Two samples (Pa3.R2 and Pa5.R1), which clustered with tumor samples from other patients, are indicated

value <0.01 as a predicted molecular subtype. We did not calculate subtype scores for large-cell and pleomorphic carcinoma samples.

For epithelial–mesenchymal transition score calculation, we used the 76-gene epithelial–mesenchymal transition signature panel [15] with the average-based method introduced previously [16]. First, expression values of each gene were standardized by the mean and standard deviation. For each sample, an epithelial–mesenchymal transition score was calculated as the average expression values for mesenchymal genes minus the average expression values for epithelial genes.

Prognostic gene signature analysis

We queried published studies on mRNA microarray-based prognostic signatures for non-small cell lung cancer [17] and selected two frequently cited prognostic signatures for further analyses [18, 19]. The first signature consisting of six genes [18] was originally developed using RT-PCR and validated on four independent public microarray data sets. For each of the six genes, expression values were subtracted by the median of the gene. We skipped housekeeping gene normalization, which was done for the RT-PCR data in the original paper. Euclidean distances to the training cluster medians (high- or low-risk cluster provided by the original paper) were used to predict prognostic subgroups. The prediction was performed only when the ratio of two distances to the training cluster medians is less than 0.9. The second signature consisting of 15 genes [19] uses supervised principal component analysis to calculate risk scores. For each of the 15 genes, expression values were transformed to *Z*-scores by centering to the mean and scaling to the standard deviation of the gene. In the original paper, the risk scores of four independent published microarray data sets for validation were dichotomized at −0.1, the median risk score determined in the training data set. With the same principal component analysis rotation matrix and Cox regression coefficients, we derived risk scores for our samples and classified them based on the same cutoff −0.1.

Calculation of scores for innate anti-PD-1 resistance content signatures

We used the gene set variation analysis program with default settings to calculate the enrichment scores for the 22 innate anti-PD-1 resistance content signatures reported by the previous publication [20]. The definition files of these signatures were downloaded either from the Molecular Signature Database (MSigDB) [21] or the supplementary

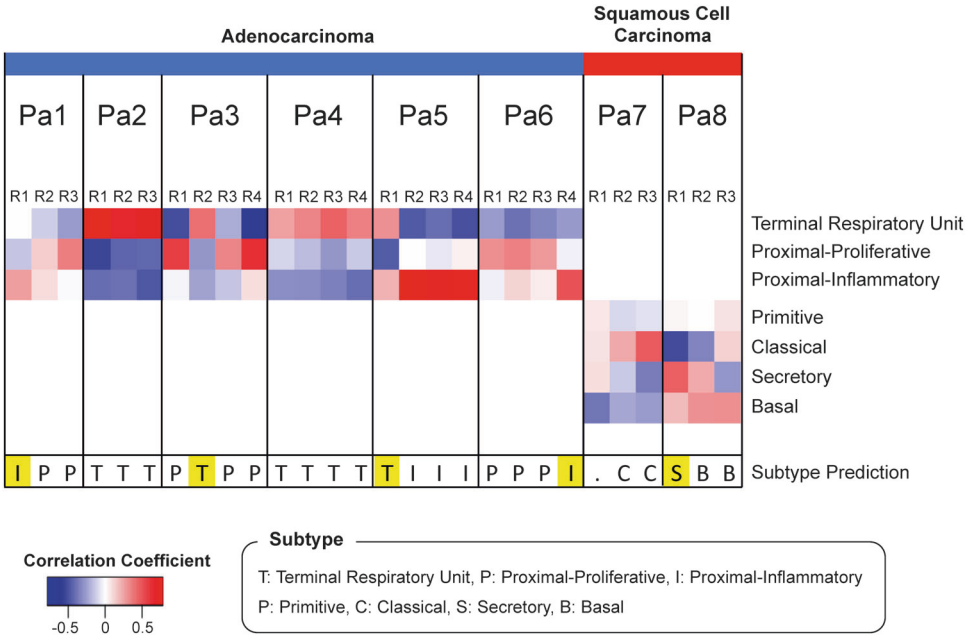

Fig. 2 Heat maps for adenocarcinoma subtype scores (top heat map) and for squamous cell carcinoma subtype scores (bottom heat map). The predicted molecular subtypes are shown with corresponding abbreviations (a "dot" represents no statistically significant molecular subtype)

file of the publication. For each signature, the enrichment scores across all samples were converted to *Z*-scores. To compute the innate anti-PD-1 resistance "co-enrichment" score for a given sample, we averaged *Z*-scores for the sample across the 22 innate anti-PD-1 resistance content signatures.

Impact of tumor microenvironment on gene expression heterogeneity

Using a gene expression-based algorithm ESTIMATE [22], we calculated tumor microenvironment scores (stromal score, immune score, and corresponding tumor purity) for each sample. Then, we correlated them with epithelial–mesenchymal transition, innate anti-PD-1 resistance, and lung adenocarcinoma subtype scores. Overall gene expression profiles were represented by the first principal components and correlated with the tumor microenvironment scores. Pearson correlation coefficient was used to measure the degree of correlation.

Results

Gene expression heterogeneity between and within non-small cell lung cancers

To determine the variation of gene expression patterns between different regions of the individual tumors and across the different tumors, we performed unsupervised hierarchical clustering. When comparing all samples across the different patients, different tumor regions from the same patients clustered together for all patients except two tumor samples Pa3.R2 and Pa5.R1, which clustered with tumor samples from other patients (Fig. 1a). The principal component analysis also showed a similar pattern with the two tumor samples mixing with tumors from different patients (intraclass correlation coefficient of the first principal component: 0.96, 95% CI (0.9, 0.98), Fig. 1b). These results suggest marked inter-individual gene expression heterogeneity and to a less extent intra-tumor heterogeneity. However, certain tumors may have high level of gene expression intra-tumor heterogeneity that is comparable to the heterogeneity between different tumors.

Varied molecular subtypes within the same tumors

Molecular subtyping has become a critical component of precision oncology and gene expression profiling has been used for molecular subtyping in many types of cancers including breast cancer [23], glioblastoma [24], colorectal cancer [25], and lung cancer [11–13, 26]. Lung adenocarcinomas can be classified into terminal respiratory unit, proximal proliferative, and the proximal inflammatory subtypes [13], while lung squamous cell carcinomas can be classified into classical, basal, secretory, and primitive subtypes [11]. In the previous studies, the molecular subtyping has been based on a single tumor sample. Since we observed evidence of gene expression intra-tumor heterogeneity, we next investigated whether the molecular subtype is concordant between different tumor regions within the same tumors. As shown in Fig. 2 and Supplementary Table 2, heterogeneous molecular subtype scores were observed between different tumor regions within the same

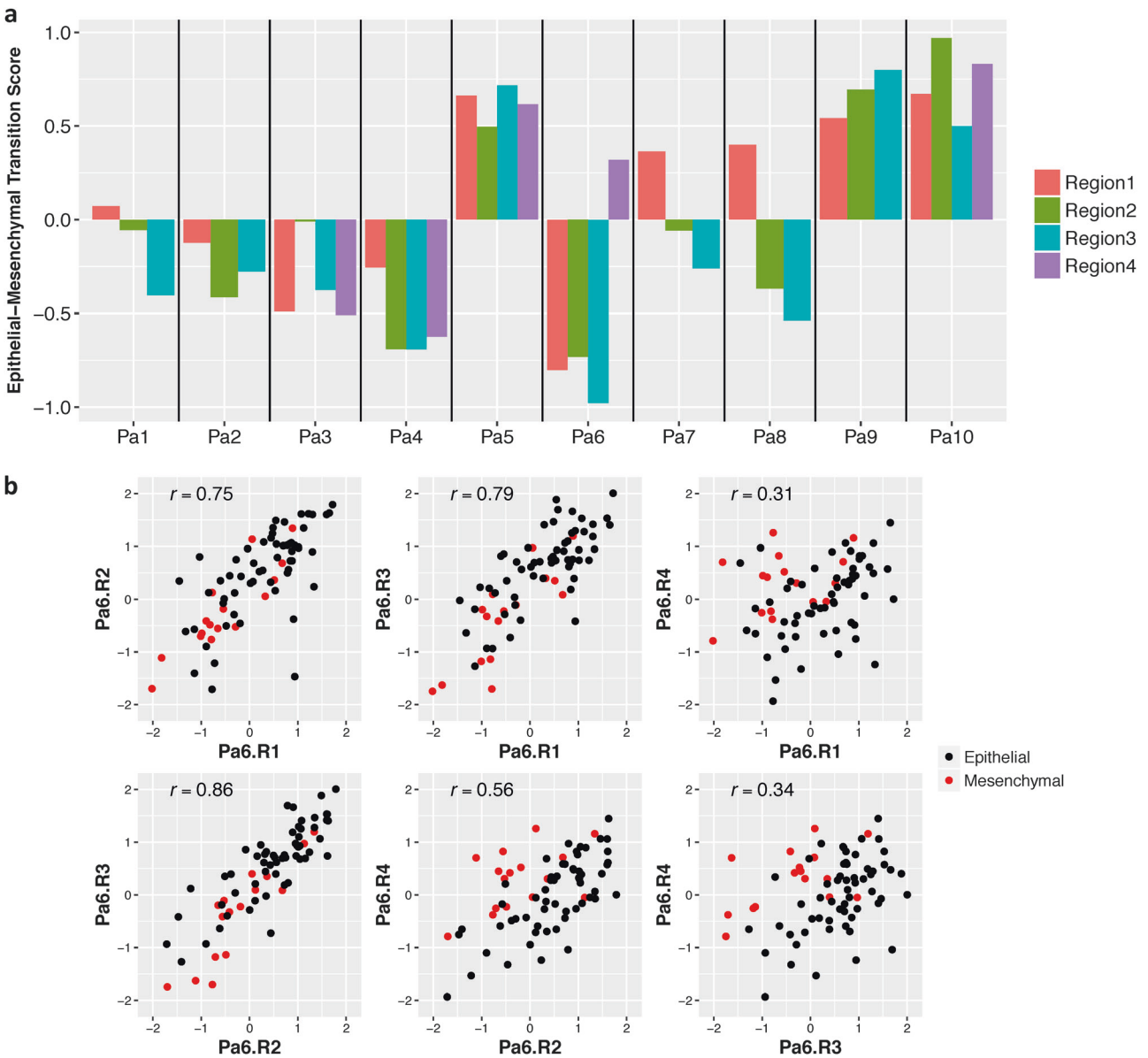

Fig. 3 **a** Epithelial–mesenchymal transition scores for all tumor samples. Pa1 to Pa6: adenocarcinoma, Pa7 and Pa8: squamous cell carcinoma, Pa9: large-cell carcinoma and Pa10: pleomorphic carcinoma. **b** All pairwise epithelial–mesenchymal transition-related gene expression correlations for Pa6. The Pearson correlation coefficient is shown within each plot

tumors. For example, Pa1.R1 had the highest score for proximal inflammatory subtype, while the other two tumor regions of Pa1 demonstrated the highest scores for proximal proliferative subtype. In Pa3, terminal respiratory unit is the predicted subtype in Pa3.R2 while all three other samples from Pa3 are predicted to be proximal proliferative subtype.

Varied prognostic gene signatures within the same tumors

Numerous gene expression-based profiles of non-small cell lung cancer have been generated over the past 20 years and many diagnostic and prognostic gene signatures have been proposed. Given the substantial gene expression intra-tumor heterogeneity observed in our cohort, we next investigated whether different tumor regions would show different gene signatures that are associated with prognosis of lung cancer patients.

The first signature we looked at was epithelial–mesenchymal transition. Epithelial–mesenchymal transition is a biological process, by which epithelial cells lose cell adhesion molecules and become more like mesenchymal cells with high migratory and invasive capabilities. Epithelial–mesenchymal transition was reported to be a potential prognostic and predictive marker in patients

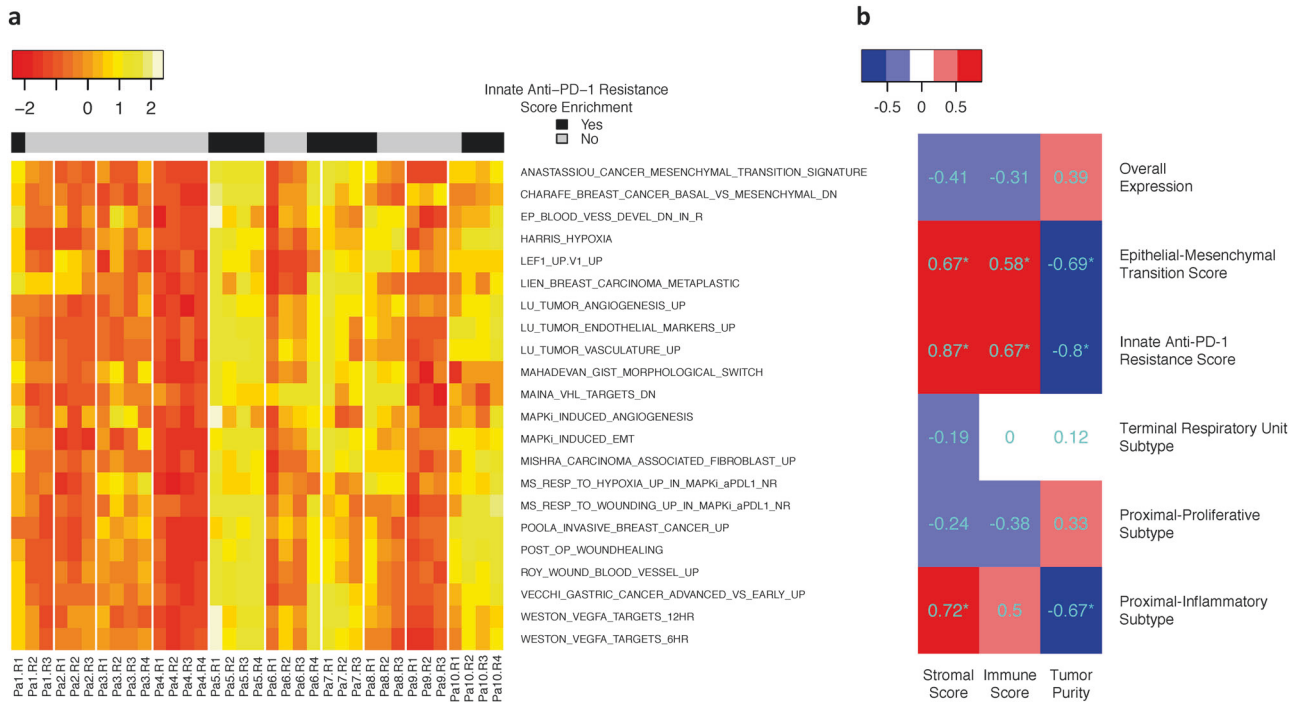

Fig. 4 **a** Gene set variation analysis enrichment scores for 22 innate anti-PD-1 resistance content signatures were calculated for each sample. The rows represent signatures and the columns represent samples. Innate anti-PD-1 resistance co-enrichment status was determined by the innate anti-PD-1 resistance co-enrichment score cutoff 0.35 and shown on top of the heat map. **b** Correlation of tumor microenvironment scores with various gene expression signatures examined in this study. Pearson correlation coefficients are shown and the ones with p value <0.01 are marked with an asterisk

with lung cancer [27–30]. Using our previously developed 76-gene epithelial–mesenchymal transition signature panel [15], we computed an epithelial–mesenchymal transition score for each sample (Fig. 3a and Supplementary Table 3). Consistent with previous studies [31, 32], different tumors demonstrated different epithelial–mesenchymal transition scores and the poorly differentiated large-cell carcinoma, pleomorphic carcinoma, and squamous cell carcinomas showed higher (i.e., more mesenchymal) scores than adenocarcinomas (p value: 0.003). Different regions of the same tumors demonstrated similar epithelial–mesenchymal transition scores for the most part (intraclass correlation coefficient of epithelial–mesenchymal transition score: 0.71, 95% CI (0.43, 0.90)); however, considerable intra-tumor heterogeneity of epithelial–mesenchymal transition scores were observed in some tumors. For example, within tumor Pa6, only Pa6.R4 clearly demonstrated over-expression of mesenchymal-specific genes and corresponding high epithelial–mesenchymal transition score, while all the other three tumor regions showed very low epithelial–mesenchymal transition scores (Fig. 3a). In addition, although the expression levels of epithelial–mesenchymal transition-related genes were mostly correlated between different regions within the same tumors, the correlation was weak for many tumor pairs further suggesting the spatially heterogeneous expression of epithelial–mesenchymal transition-related genes (Fig. 3b and Supplementary Figure 2).

Next, we selected two other frequently cited mRNA microarray-based prognostic signatures [18, 19] and calculated the risk scores in each tumor region. As expected, the risk score varied between different tumor regions within the same tumors (Supplementary Table 4). Interestingly, when every tumor region was classified into high- and low-risk prognostic subgroups based on the same criteria in the original studies, discordant prognostication derived from different tumor regions within the same tumor was observed in 1 of the 10 patients using the 6-gene signature and in 7 of the 10 patients using the 15-gene signature, respectively. These results suggest that gene expression-based prognostic signature from a single biopsy could either under- or over-estimate the risk of recurrence of patients with non-small cell lung cancer due to the gene expression intra-tumor heterogeneity.

Varied innate anti-PD-1 resistance signatures within the same tumor

Recent studies have shown that gene expression-based molecular subtypes were associated with response to immune checkpoint inhibition in bladder cancer [33] and melanoma [20]. Hugo et al. reported innate anti-PD-1

resistance transcriptomic signature in melanoma and other cancers including lung cancer [20]. Using the same innate anti-PD-1 resistance signature, we characterized our tumor samples (Fig. 4a). For a given sample, we computed the innate anti-PD-1 resistance co-enrichment score to measure the level of co-enrichment of the 22 innate anti-PD-1 resistance content signatures (Supplementary Table 5). In general, innate anti-PD-1 resistance co-enrichment score was similar within the same tumor (intraclass correlation coefficient of innate anti-PD-1 resistance co-enrichment score: 0.77, 95% CI (0.52, 0.93)). However, spatial heterogeneity was observed in multiple tumors. When we dichotomized samples by the innate anti-PD-1 resistance co-enrichment score cutoff (0.35) that was used in the original literature, 4 in 10 patients harbored at least one discordant tumor region. For example, in tumor Pa6, Pa6.R4 is considered as an anti-PD-1-resistant tumor by showing the high innate anti-PD-1 resistance co-enrichment score of 0.94. However, the other three tumor regions (Pa6.R1, Pa6.R2, and Pa6.R3) showed low innate anti-PD-1 resistance co-enrichment scores of −0.94, 0.06, and −0.29, respectively. Our data suggest that the intra-tumor heterogeneity may need to be taken into consideration if gene expression-associated signatures were to be used as biomarkers for immune checkpoint blockade therapy.

Varied tumor microenvironment

Cancers are not homogenous masses of malignant cells. Many other cells are recruited to the tumor tissue including fibroblasts, blood and lymphatic vessel endothelial cells, and infiltrating immune cells, which constitute the tumor microenvironment. Each cell type may have distinct gene expression profile of its own and the overall gene expression profile of a given tumor sample reflects the amount of each cell type and the interactions between cancer cells and non-transformed cells in that tumor microenvironment. To understand the impact of tumor microenvironment on gene expression intra-tumor heterogeneity, we inferred the proportions of infiltrating stromal and immune cells for each tumor region using a gene expression-based algorithm ESTIMATE [22] and correlated tumor microenvironment scores with the gene expression signatures examined in this study. Our results showed that different tumor regions have different proportions of cancer cells, infiltrating stromal and immune cells (Supplementary Table 6). As shown in Fig. 4b and Supplementary Figure 3a, the overall gene expression variation was only weakly correlated with stromal score, immune score, or tumor purity with Pearson correlation coefficient of −0.41, −0.31, and 0.39, respectively. However, we observed high level of correlation (absolute Pearson correlation coefficient: 0.58–0.87) between epithelial–mesenchymal transition/innate anti-PD-1 resistance score and stromal/immune score (Fig. 4b and Supplementary Figure 3b–c). Among the lung adenocarcinoma molecular subtypes, proximal inflammatory subtype was positively correlated with stromal and immune scores (Fig. 4b and Supplementary Figure 3f).

Discussion

Using an approach of multiregion sampling and comprehensive gene expression analysis of 10 non-small cell lung cancers, we demonstrated clear evidence of gene expression intra-tumor heterogeneity in all tumors studied. Two tumor samples showed substantial level of global intra-tumor heterogeneity comparable to heterogeneity between different patients (Fig. 1). In addition to the global gene expression profile, substantial intra-tumor heterogeneity was also observed for molecular subtypes and various clinically relevant gene expression signatures including epithelial–mesenchymal transition signature, a recently reported immune therapy response signature and two frequently cited prognostic signatures (Figs. 2–4 and Supplementary Tables 2–5). Interestingly, global intra-tumor heterogeneity did not always correlate with intra-tumor heterogeneity observed in the signatures with selected genes.

Programmed cell death protein 1 (PD-1) immune checkpoint blockade has shown unprecedented durable clinical responses in patients with various cancer types including metastatic non-small cell lung cancer [34]; however, the response rate is suboptimal [35, 36]. There are currently no reliable biomarkers to predict response to immune checkpoint blockade. Expression of programmed death-ligand 1 (PD-L1) protein was reported to be predictive of benefit from immune checkpoint blockade treatment, but robust responses seen in patients with low PD-L1 argues against its value as an exclusionary predictive biomarker [37]. Gene expression-based signatures have been recently reported to correlate with response to immune checkpoint inhibition in various cancer types and proposed as potential predictive markers [20, 33]. Using a recently published innate anti-PD-1 resistance signature analysis, our results showed 4 out of the 10 patients harbored substantially different innate anti-PD-1 resistance scores in different tumor regions within the same tumors that may lead to discordant prediction of response to anti-PD-1 checkpoint inhibition. When correlating to the tumor microenvironment, innate anti-PD-1 resistance score was found to correlate negatively with tumor purity, and positively with immune score and stromal score, which is as expected because it is well known that tumor infiltrating lymphocyte profile, particularly CD8+ T cell infiltrate is associated with response to anti-PD-1 therapy [38]. What is

interesting is that the correlation of innate anti-PD-1 resistance score with stromal score was higher than that with the immune score (correlation coefficient of 0.87 versus 0.67), indicating that in addition to immune cells, other stromal cells may also contribute to impact on the anti-PD-1 response signature.

Cancer tissues are composed of both cancer cells and non-cancerous stromal cells that form the tumor microenvironment. Our data demonstrated heterogeneous tumor microenvironments in spatially separated tumor regions within the same tumor (Supplementary Table 6). This heterogeneous tumor microenvironment is closely correlated to some characteristics of tumor represented by the gene expression signatures explored in this study (Supplementary Figure 3). However, these correlations were only marginal at overall gene expression profile. In addition, different tumor regions from the same patients almost always clustered together in spite of different tumor purity, stromal or immune scores (Fig. 1). Taken together, our data suggest that the gene expression intra-tumor heterogeneity observed in this study may be attributed to the different tumor microenvironments as well as spatial difference in gene expression profiles of lung cancer cells.

Many prognostic gene signatures have been developed by diverse analytical techniques. Commercially available and clinically applicable prognostic tests like Pervenio™ Lung RS [39] are often based on small prognostic and predictive gene sets with RT-PCR protocol. Future studies include the investigation on the intra-tumor heterogeneity of those signatures with the same techniques by which they were developed. Moreover, higher-resolution technologies, such as RNA sequencing on a larger cohort of patients, ideally supported by genomics and epigenetic data will help us to better understand the gene expression intra-tumor heterogeneity in lung cancer and its impact on cancer biology and clinical outcomes.

In summary, our study is the first study, to the best of our knowledge, on comprehensive gene expression intra-tumor heterogeneity of any cancer type. We observed clear evidence of gene expression intra-tumor heterogeneity from all tumors in this cohort for both the overall gene expression profile and the expression signatures with selected genes. Since many of these gene expression signatures have been reported to be associated with clinical outcomes of lung cancers and proposed as potential prognostic and/or predictive biomarkers, our results suggest that gene expression intra-tumor heterogeneity should be taken into consideration when evaluating gene expression-based biomarkers.

Acknowledgements This work was supported by MD Anderson Lung cancer Moon Shot Program, MD Anderson Physician Scientist Program, Conquer Cancer Foundation Young Investigator Award, Khalifa Scholar Award, the Cancer Prevention and Research Institute of Texas (R120501), the Cancer Prevention and Research Institute of Texas Multi-Investigator Research Award grant (RP160668), the University of Texas (UT) Systems Stars Award (PS100149), the Welch Foundation Robert A. Welch Distinguished University Chair Award (G-0040), Department of Defense PROSPECT grant (W81XWH-07-1-0306), the UT Lung Specialized Programs of Research Excellence grant (P50CA70907), and T.J. Martell Foundation.

Compliance with ethical standards

Conflict of interest The authors declare that they have no conflict of interest.

References

1. The Cancer Genome Atlas - National Cancer Institute. http://cancergenome.nih.gov. Accessed 15th July 2016.
2. McGranahan N, Swanton C. Biological and therapeutic impact of intratumor heterogeneity in cancer evolution. Cancer Cell. 2015;27:15–26.
3. Gerlinger M, Rowan AJ, Horswell S, et al. Intratumor heterogeneity and branched evolution revealed by multiregion sequencing. N Engl J Med. 2012;366:883–92.
4. Gerlinger M, Horswell S, Larkin J, et al. Genomic architecture and evolution of clear cell renal cell carcinomas defined by multiregion sequencing. Nat Genet. 2014;46:225–33.
5. Zhang J, Fujimoto J, Zhang J, et al. Intratumor heterogeneity in localized lung adenocarcinomas delineated by multiregion sequencing. Science. 2014;346:256–9.
6. de Bruin EC, McGranahan N, Mitter R, et al. Spatial and temporal diversity in genomic instability processes defines lung cancer evolution. Science. 2014;346:251–6.
7. Pertschuk LP, Axiotis CA, Feldman JG, et al. Marked intratumoral heterogeneity of the proto-oncogene Her-2/neu determined by three different detection systems. Breast J. 1999;5:369–74.
8. Chung GG, Zerkowski MP, Ghosh S, Camp RL, Rimm DL. Quantitative analysis of estrogen receptor heterogeneity in breast cancer. Lab Invest. 2007;87:662–9.
9. Yang J, Luo H, Li Y, et al. Intratumoral heterogeneity determines discordant results of diagnostic tests for human epidermal growth factor receptor (HER) 2 in gastric cancer specimens. Cell Biochem Biophys. 2012;62:221–8.
10. Gyanchandani R, Lin Y, Lin HM, et al. Intratumor heterogeneity affects gene expression profile test prognostic risk stratification in early breast cancer. Clin Cancer Res. 2016;22:5362–9.
11. Wilkerson MD, Yin X, Hoadley KA, et al. Lung squamous cell carcinoma mRNA expression subtypes are reproducible, clinically important, and correspond to normal cell types. Clin Cancer Res. 2010;16:4864–75.
12. Wilkerson MD, Yin X, Walter V, et al. Differential pathogenesis of lung adenocarcinoma subtypes involving sequence mutations, copy number, chromosomal instability, and methylation. PLoS ONE. 2012;7:e36530.
13. Cancer Genome Atlas Research Network. Comprehensive molecular profiling of lung adenocarcinoma. Nature. 2014;511:543–50.
14. Ringner M, Jonsson G, Staaf J. Prognostic and chemotherapy predictive value of gene-expression phenotypes in primary lung adenocarcinoma. Clin Cancer Res. 2016;22:218–29.
15. Byers LA, Diao L, Wang J, et al. An epithelial-mesenchymal transition gene signature predicts resistance to EGFR and PI3K inhibitors and identifies Axl as a therapeutic target for overcoming EGFR inhibitor resistance. Clin Cancer Res. 2013;19:279–90.
16. Chen L, Gibbons DL, Goswami S, et al. Metastasis is regulated via microRNA-200/ZEB1 axis control of tumour cell PD-L1

expression and intratumoral immunosuppression. Nat Commun. 2014;5:5241.
17. Kuner R. Lung cancer gene signatures and clinical perspectives. Microarrays. 2013;2:318–39.
18. Boutros PC, Lau SK, Pintilie M, et al. Prognostic gene signatures for non-small-cell lung cancer. Proc Natl Acad Sci USA. 2009;106:2824–8.
19. Zhu CQ, Ding K, Strumpf D, et al. Prognostic and predictive gene signature for adjuvant chemotherapy in resected non-small-cell lung cancer. J Clin Oncol. 2010;28:4417–24.
20. Hugo W, Zaretsky JM, Sun L, et al. Genomic and transcriptomic features of response to anti-PD-1 therapy in metastatic melanoma. Cell. 2016;165:35–44.
21. Subramanian A, Tamayo P, Mootha VK, et al. Gene set enrichment analysis: a knowledge-based approach for interpreting genome-wide expression profiles. Proc Natl Acad Sci USA. 2005;102:15545–50.
22. Yoshihara K, Shahmoradgoli M, Martinez E, et al. Inferring tumour purity and stromal and immune cell admixture from expression data. Nat Commun. 2013;4:2612.
23. Perou CM, Sorlie T, Eisen MB, et al. Molecular portraits of human breast tumours. Nature. 2000;406:747–52.
24. Verhaak RG, Hoadley KA, Purdom E, et al. Integrated genomic analysis identifies clinically relevant subtypes of glioblastoma characterized by abnormalities in PDGFRA, IDH1, EGFR, and NF1. Cancer Cell. 2010;17:98–110.
25. Guinney J, Dienstmann R, Wang X, et al. The consensus molecular subtypes of colorectal cancer. Nat Med. 2015;21: 1350–6.
26. Cancer Genome Atlas Research Network. Comprehensive genomic characterization of squamous cell lung cancers. Nature. 2012;489:519–25.
27. Thomson S, Buck E, Petti F, et al. Epithelial to mesenchymal transition is a determinant of sensitivity of non-small-cell lung carcinoma cell lines and xenografts to epidermal growth factor receptor inhibition. Cancer Res. 2005;65:9455–62.
28. Yauch RL, Januario T, Eberhard DA, et al. Epithelial versus mesenchymal phenotype determines in vitro sensitivity and predicts clinical activity of erlotinib in lung cancer patients. Clin Cancer Res. 2005;11:8686–98.
29. Frederick BA, Helfrich BA, Coldren CD, et al. Epithelial to mesenchymal transition predicts gefitinib resistance in cell lines of head and neck squamous cell carcinoma and non-small cell lung carcinoma. Mol Cancer Ther. 2007;6:1683–91.
30. Papadimitrakopoulou V, Lee JJ, Wistuba, II, et al. The BATTLE-2 study: a biomarker-integrated targeted therapy study in previously treated patients with advanced non-small-cell lung cancer. J Clin Oncol. 2016;34:3638-47.
31. Nitsche K, Gunther B, Katenkamp D, Petersen I. Thoracic neoplasms at the Jena reference center for soft tissue tumors. J Cancer Res Clin Oncol. 2012;138:415–24.
32. Matsubara D, Kishaba Y, Yoshimoto T, et al. Immunohistochemical analysis of the expression of E-cadherin and ZEB1 in non-small cell lung cancer. Pathol Int. 2014;64:560–8.
33. Rosenberg JE, Hoffman-Censits J, Powles T, et al. Atezolizumab in patients with locally advanced and metastatic urothelial carcinoma who have progressed following treatment with platinum-based chemotherapy: a single-arm, multicentre, phase 2 trial. Lancet. 2016;387:1909–20.
34. Pardoll DM. The blockade of immune checkpoints in cancer immunotherapy. Nat Rev Cancer. 2012;12:252–64.
35. Brahmer JR, Tykodi SS, Chow LQ, et al. Safety and activity of anti-PD-L1 antibody in patients with advanced cancer. N Engl J Med. 2012;366:2455–65.
36. Topalian SL, Hodi FS, Brahmer JR, et al. Safety, activity, and immune correlates of anti-PD-1 antibody in cancer. N Engl J Med. 2012;366:2443–54.
37. Patel SP, Kurzrock R. PD-L1 expression as a predictive biomarker in cancer immunotherapy. Mol Cancer Ther. 2015;14:847–56.
38. Tumeh PC, Harview CL, Yearley JH, et al. PD-1 blockade induces responses by inhibiting adaptive immune resistance. Nature. 2014;515:568–71.
39. Kratz JR, He J, Van Den Eeden SK, et al. A practical molecular assay to predict survival in resected non-squamous, non-small-cell lung cancer: development and international validation studies. Lancet. 2012;379:823–32.